Politecnico di Milano

Master degree in Engineering Physics

School of Industrial and Information Engineering
Department of Physics & DEIB

Topological protection of EM Waves with metallic Photonic Crystal

Theory and application to Contra-Directional coupler

Supervisor:
Prof. Gian Guido Gentili
Co-supervisor:
Prof. Stefano Selleri[1]

Thesis work by:
Francesco Piccioli

Academic year: 2016/2017

---

[1]Department of Information Engineering, University of Florence

To my mum and dad,,
my personal superheroes

Abstract

Photonic Topological Insulators (PTI) are Photonic Crystals (PhC) structures with a bulk Photonic Band Gap (PBG) but gapless topologically protected states at its surface. These Topologically Protected Surface States (TPSS) are unidirectional and insensitive to a broad range of lattice defects including bends, disorders and vacancies. A metallic PTI that directly emulates Quantum Spin Hall Effect (QSH) and does not explicitly break time-reversal symmetry is here studied both theoretically and numerically. A broad range of numerical simulations are carried out employing commercial softwares HFSS$^{\text{TM}}$ and CST MWS$^{\text{TM}}$ to inspect the propagation properties of the proposed Topologically Protected Meta Waveguide (TPMW). Polarization-preserving properties of QSH PTI are used to design a compact hybrid directional and contra-directional coupler operating with a fractional bandwidth of 0.067 centered on 22.33GHz.

Sommario

Gli Isolanti Topologici Fotonici (PTI) sono Cristalli Fotonici (PhC) con un gap proibito interno (PBG) ma con stati privi di gap e topologicamente protetti alla superficie. Tali Stati Superficiali Topologicamente Protetti (TPSS) sono unidirezionali ed immuni a molti difetti del reticolo cristallino fra cui curve arbitrariamente strette, irregolarità e lacune nel reticolo. Questo lavoro di Tesi consiste nello studio, teorico e numerico, di un PTI metallico che emula direttamente l' effetto di Hall Quantistico di Spin (QSH) senza violare la simmetria di invarianza temporale. Sono state condotte diverse simulazioni numeriche utilizzando i software commerciali HFSS$^{\text{TM}}$ e CST MWS$^{\text{TM}}$ allo scopo di esplorare le proprietà di trasporto di onde EM della guida d'onda a protezione topologica (TPMW) qui proposta. Le proprietà di conservazione della polarizzazione, peculiari dei QSH PTI vengono utilizzate per progettare un accoppiatore ibrido direzionale e contro direzionale compatto operante su una banda frazionaria di 0.067 centrata a 22.33GHz

Acknowledgements

There is no way I can thank enough Proff. Gentili and Selleri for the kindness and patience they demonstrated throughout the time I spent working under their supervision. In particular I wish to thank both of them for the opportunity to be involved into publications and Prof Gentili for the possibility to present part of this work at the IWMMbD in Riva del Garda. Last years under their wings have been invaluable for my professional growth both in research and in personal skills.

I'm also very grateful to Proff. Longhi and Della Valle for their kindness and availability in discussing the CD coupling behavior of the TPMW.

A warm thank you goes also to all my *fellow travelers*: my colleagues at Engineering Physics, the crazy and wonderful people at "Teatro delle Biglie" and my friends, whose support and friendship drove me throughout and to the end of this path. Last but not least thank you to Sara, Chiara and to my parents, to whom this thesis is dedicated.

Contents

Introduction

THE practice to look at things from different perspectives often opens unexpected paths in research, and it is from links between different fields that some of science greatest achievements eventually came. In this sense mathematics have proven to be a useful tool to sunder a model from its physical application thus exploring similarities that otherwise would have been physically counterintuitive. Photonic Crystals are a clear example of application of a modelized physical behavior (Electrons in a periodic potential) to a different context (Photons in a periodic index medium).

In the last few decades topology, a branch of mathematics that earlier had only found applications in pure research, have been successfully used to understand matter at a new level. Topological phases of matter have, from the late 80's until 2016 award of the Nobel Prize to Haldane Thouless and Kosterlitz, received ever growing interest for the exotic properties that arise as a consequence of topological ordering in condensed matter.

Topological Insulators (TI) are a phase of solid matter similar to ordinary insulators in that the energy spectrum of a bulk TI presents a large energy gap preventing conduction. Topological properties however shows themselves at samples boundaries, where TI unexpectedly show conducting states with peculiar properties of unidirectionality and insensitivity to defects. As macroscopic results of microscopic topological ordering TI, like all topological phases of matter, are interpreted as macroscopic manifestations of quantum behaviors, making them an important tool to study microscopic properties of matter. In particular Topologically insulating phase is a manifestation of Quantum Hall Effect (QH) and Quantum Spin Hall Effect (QSH).

Photonic Topological Insulators (PTI) are Photonic Crystals (PhC) that exhibit the same topologically characteristic properties of TI. As TI, bulk PTIs have a Photonic Band Gap (PBG) inhibiting propagation of EM waves, however on the edges Topologically Protected Surface States (TPSS) for EM propagation arise, in which waves seemingly propagates without back-scattering and showing extremely interesting properties of defect insensitivity.

Although topological effects in Solid State are observed only when the microscopic topological ordering prevails on defects and thermal chaos, thus at very low temperatures, Topological properties in PhC can be engineered with macroscopic structures in which the role of disorder can be arbitrarily reduced within the technological capabilities, making them an invaluable research tool for solid state physics itself. The possibility to work with Maxwell's equation instead that directly dealing with quantum mechanics provides additional benefits because of the possibility to numerically simulate the behavior of the most different structures. For example Time-inversion and Parity symmetries can be individually violated and the interface between heterogeneous topologically characteristic band gap can be numerically inspected. Direct observations of electronic TPSS in these complex structures has not been so far experimentally realized due to technical difficulties in interfacing arbitrary hetero structures.

This thesis work deals with a novel metallic Bianisotropic Photonic Crystal (BPhC) introduced by the groups of G. Shvets and A.B. Khanikaev in which Bianisotropy directly emulates Spin Orbit Interaction (SOI) leading to a photonic analogue of QSH TI. A broad Range of numerical simulations are carried out to understand the working principles of the PhC and to show the practical design of a multi-port directional coupler realized with the studied platform.

In the second chapter, starting from the derivation of the master equations of EM waves, the working principles of PhCs are recalled with particular focus on defective states in planar PhC. The second part of the chapter will deal with Topology concepts in Physics. After an introduction to TI and a brief historical review, the Kane-Mele Hamiltonian of graphene will be presented and discussed. Examples of periodic structures realizing PTI from recent literature will be cited to end the chapter.

In the third chapter the BPhC which is the object of the work will be introduced. At first the complete derivation of the W-S cell and it's numerical model will be presented with particular focus on the computational methods. Then the optimal geometrical parameters will be

derived employing empirical parametric analysis. Later on the mathematical formulation, employing a perturbation approach, leading to the direct emulation of the Kane-Mele model will be discussed and the chapter will be finally concluded with an analysis of the Topologically Protected Meta Waveguide (TPMW) guided modes employing the super-cell method.

After a discussion on the numerical methods to perform full-wave simulations of PhC the fourth chapter will deal mainly with devices that could theoretically be realized using the proposed Topologically Protected Meta Waveguide (TPMW) platform. Various proposals for mode launchers will be compared, topological Protection will be tested as perfect transmission around sharp bends will be demonstrated. Finally, after a brief review of the Coupled Mode Theory, the design for an hybrid directional/contra-directional coupler working in the 20-30GHz range will be illustrated.
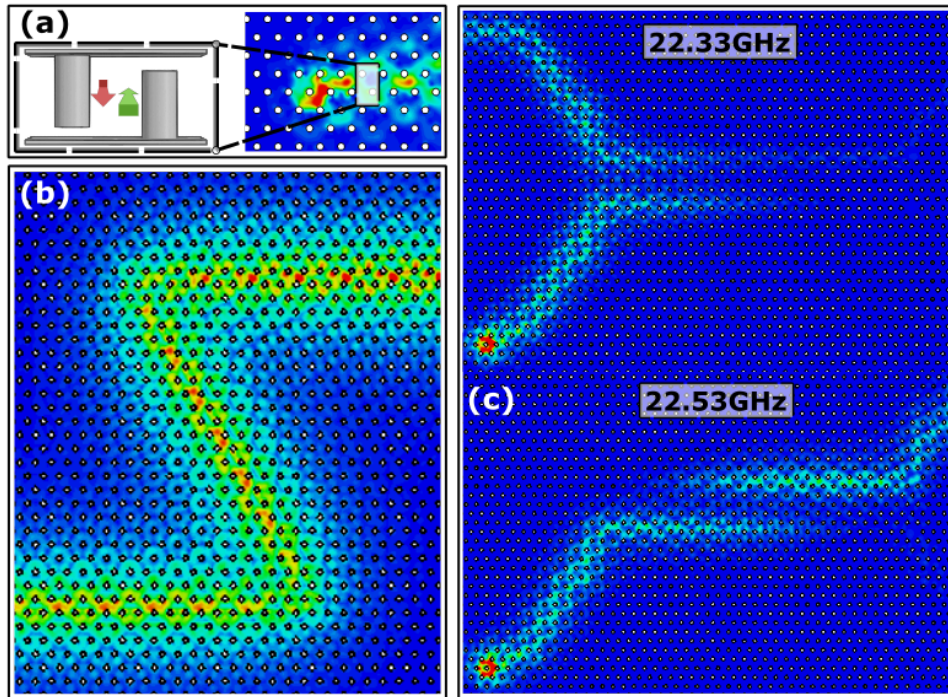
Fig. 1.1: Some examples of Topological Protection related phenomena involving EM waves. **(a):** Unidirectional EM excitation and TPMW schematic (inset).**(b):** Transmission around sharp bend. **(c):** Hybrid directional coupling in Coupled TPMW (CTPMW) [6, 7].

In the conclusions a possible technology for practical realization of the proposed structure is identified and the guidelines for further investigation of the subject are stated.

Theoretical background

AMONG the great achievements of solid state physics, the Bloch theorem is undoubtedly one of the most important one. One of the fundamental results of quantum mechanics, ultimately represented by the Bloch theorem, is that electrons in a periodic potential propagates as waves (Bloch waves). In recent years [15] the mathematical formulation of the Bloch theorem has been applied to a number of different physical systems in order to study the propagation properties inside periodic materials not of electrons but of EM waves or phonons. Similarities between *electrons in crystals* and *photons in Photonic Crystals (PhC)* have been ever growing since, and nearly any phenomenon occurring in solid state physics have been investigated for its photonic counterpart. This eventually pushed the research in the field of photonics and integrated optics and nowadays PhCs find practical applications in many field of research [5, 28, 35, 40, 45].

Very recently also topological phases of matter, a new discovered set of phases characterized by topological in-variants, have attracted growing interest among the scientific community. Topological Insulators (TI) are specific topological phase of crystals and, like most of the phenomena involving electrons in crystals, finds their counterpart in photonics.

The first two sections of this chapter will be dedicated to PhCs. Initially bulk structures will be considered then the effect of defect and terminations will be briefly inspected. In the third section the Topological Insulating state of matter will be introduced with particular focus on the *Quantum Spin Hall Effect (QSH) TI state* and its description by the Kane-Mele Hamiltonian. A quick review of the most recent Photonic implementation of TI will close the chapter

2.1   Photonic Crystals

While semiconductors are lattices in which the electronic potential is
periodically modulated thanks to the localized atoms, Photonic Crys-
tals (PhC) are artificial materials in which the refractive index is peri-
odically modulated. There are a number of techniques to obtain peri-
odically modulated indexes, but the fundamental results don't change
whether different materials are disposed in a periodic lattice or that
the concentration of dopants is spatially modulated, as in DFB lasers.

From here on we will talk about PhC as materials with a periodically
modulated refractive index, without entering into the detail of their
fabrication. There are four kind of PhC, whose distinction can be
made depending on how many dimensions are involved in the index
modulation (Fig. 2.1)
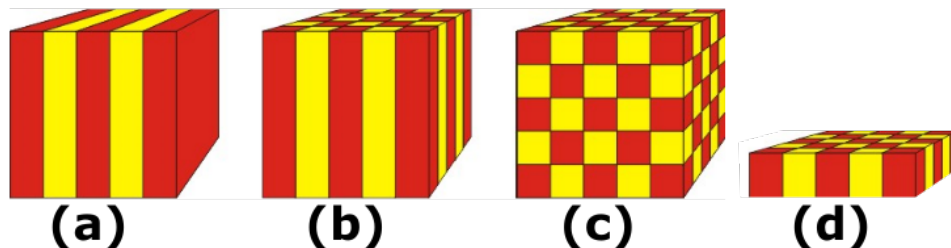
Fig. 2.1: Photonic Crystals (PhC) of different dimensions: 1D(**a**), 2D(**b**),
           3D(**c**), slab(**d**)

- **1D Crystals:** The index is modulated in one dimension while
  the medium is homogeneous in the other two.

- **2D Crystals:** The index is modulated in two dimensions while
  the medium is homogeneous in the third.

- **3D Crystals:** The index is modulated in the three dimensions
  of space.

- **Slab Crystals:** The index is modulated in two dimensions but
  the medium is not homogeneous in the third direction, usually
  the medium is truncated and vertical confinement is achieved for
  total internal reflection (index guiding) or with mirrors.

  note: This class is often included in the second, but the two cases
       are qualitatively different. Furthermore strictly speaking 2D
       PhCs need an extension on the third dimension that is much
       longer then the wavelength, making them intrinsically big
       structures while slab crystals can be thin.

2.1.1   The master equation

$$\begin{cases} \boldsymbol{\nabla} \cdot \epsilon(\mathbf{r})\mathbf{E}(\mathbf{r},t) = 0 \\[2mm] \boldsymbol{\nabla} \times \mathbf{E}(\mathbf{r},t) = -\mu_0 \dfrac{\partial \mathbf{H}(\mathbf{r},t)}{\partial t} \\[2mm] \boldsymbol{\nabla} \cdot \mathbf{H}(\mathbf{r},t) = 0 \\[2mm] \boldsymbol{\nabla} \times \mathbf{H}(\mathbf{r},t) = \epsilon(\mathbf{r}) \dfrac{\partial \mathbf{E}(\mathbf{r},t)}{\partial t} \end{cases} \tag{2.1}$$

Under the hypotheses of absences of surces and linear, lossless and non magnetic materials the solutions of Maxwell's equations (2.1) are transverse waves [3]. Under these hypotheses and moving to the phasor domain (2.1) can be recasted [4,15] into the so-called Master equations for $\mathbf{H}(\mathbf{r},t)$ (2.2) and $\mathbf{E}(\mathbf{r},t)$ (2.3)

$$\begin{cases} \boldsymbol{\nabla} \times \left(\epsilon(\mathbf{r})^{-1}\boldsymbol{\nabla} \times \mathbf{H}(\mathbf{r})\right) = \left(\dfrac{\omega}{c}\right)^2 \mathbf{H}(\mathbf{r}) \\[2mm] \boldsymbol{\nabla} \cdot \mathbf{H} = 0 \end{cases} \tag{2.2}$$

$$\begin{cases} \epsilon(\mathbf{r})^{-1}\boldsymbol{\nabla} \times \boldsymbol{\nabla} \times \mathbf{E} = \left(\dfrac{\omega}{c}\right)^2 \mathbf{E}(\mathbf{r}) \\[2mm] \boldsymbol{\nabla} \cdot \epsilon(\mathbf{r})\mathbf{E} = 0 \end{cases} \tag{2.3}$$

The master equations can be viewed as eigenvalue problems defined by the differential operators $\widehat{L}_H$ $\widehat{L}_E$ acting on the magnetic and electric fields such that

$$\boldsymbol{\nabla} \times \left(\epsilon(\mathbf{r})^{-1}\boldsymbol{\nabla} \times \mathbf{H}\right) \coloneqq \widehat{L}_H\mathbf{H} = \left(\frac{\omega}{c}\right)^2 \mathbf{H}$$

$$\epsilon(\mathbf{r})^{-1}\boldsymbol{\nabla} \times \boldsymbol{\nabla} \times \mathbf{E} \coloneqq \widehat{L}_E\mathbf{E} = \left(\frac{\omega}{c}\right)^2 \mathbf{E}$$

Where, if not expressed, the space dependence of $\mathbf{E}(\mathbf{r}), \mathbf{H}\mathbf{r})$ is implicit. Even if the two operators shares the same eigenvalues the physical meaning of the two is very different. It can be demonstrated that only $\widehat{L}_H$ is an Hermitian operator i.e. for a properly defined scalar product:

$$\left(\mathbf{F}, \widehat{L}_H\mathbf{G}\right) = \left(\widehat{L}_H\mathbf{F}, \mathbf{G}\right), \quad \forall \mathbf{F}, \mathbf{G} \tag{2.4}$$

while (2.4) cannot be ensured for $\widehat{L}_E$ thus nothing can be in principle said about its solutions[1], the eigenfunctions of $\widehat{L}_H$ can be demonstrated

---

[1]multiplying for $\epsilon(\mathbf{r})$ both sides of the $\widehat{L}_H$ eigenvalue problem leads to a generalized eigenvalue problem with the same properties of $\widehat{L}_H$ [15]

to form a complete and orthogonal set as a direct consequence of (2.4), we will in the following assume normalization of eigenmodes to have unitary energy. The orthogonality condition falls for the general solutions of (2.3). It is relevant to note that the fact that $\widehat{L}_E$ is non Hermitian is due to the spatial variation of $\epsilon(\mathbf{r})$ which is a fundamental hypotheses when PhC are considered.

Following (2.4) the eigenvalues $\left(\dfrac{\omega}{c}\right)^2$ of $\widehat{L}_H$ are real and the same can be demonstrated for ω, which in principle could be either real either purely imaginary. The master equation's solutions are thus a set of orthonormal harmonic modes $\mathbf{H}_{\omega_i}$ with angular frequency $\omega_i{}^2$. The electric field of the mode can be always obtained from the magnetic field using (2.5):

$$\mathbf{E}_{\omega_i} = \frac{j}{\omega_i \epsilon_0 \epsilon(\mathbf{r})} \boldsymbol{\nabla} \times \mathbf{H}_{\omega_i} \tag{2.5}$$

It is important to note that the solution properties of $\widehat{L}_H$ can be derived without any particular assumption on the function $\epsilon(\mathbf{r})$ which can be arbitrarily shaped, even with discontinuities.

The harmonic modes that solve the master equation (2.2) can be interpreted as local minima of an appropriate energy functional. This result is known as the *electromagnetic variational theorem*. It is useful to mention the most physically significant form of the variational theorem because it will prove useful in future and it provides a clear physical interpretation of the modes:

Th. 1 (Variational Principle). *If* $\mathbf{H}$ *is an harmonic mode solving* (2.2) *then* $\mathbf{H}$, *is a local minimum of the functional* $\mathcal{U}_f(\mathbf{H})$:

$$\mathcal{U}_f(\mathbf{H}) = \frac{\int_\omega |\boldsymbol{\nabla} \times \mathbf{E}|^2 \, \mathrm{d}^3 r}{\int_\omega \epsilon(\mathbf{r}) |\mathbf{E}|^2 \, \mathrm{d}^3 r}$$

The functional has been expressed in terms of the electric field $\mathbf{E}$ obtained from $\mathbf{H}$ with (2.5) because in this way its physical meaning is more easily seen. Following Th.1 the fundamental mode (the one with the minimum eigenvalue, thus energy), is the absolute minimum of $\mathcal{U}_f$ that is the mode with the minimum spatial variation (which minimizes the numerator) and with the electric field maximally concentrated into the high-ϵ regions (which maximizes the denominator). Higher order modes oscillate more and more and fill regions with lower ϵ.

---

[2]Up to now the mode set is not necessarily discrete, indeed if $\epsilon(\mathbf{r})$ does not possess particular symmetries the spectrum of modes is continuous.

TE/TM modes decomposition

The solutions of (2.2) and (2.3) when an homogeneous medium ($\epsilon(\mathbf{r}) = \epsilon$) is considered are plane waves with arbitrary wave-vector $\mathbf{k}$. If a less trivial case is considered one may think about a medium that is homogeneous along one dimension only ($\epsilon(\mathbf{r}) = \epsilon(x, y)$). This is the case of a 2D photonic Crystal as it is evident from Fig. 2.1.

If propagation in similar media is considered for waves that do not propagate in the direction of the homogeneity then the electromagnetic modes can be divided into Transverse Electric (TE) and Transverse Magnetic (TM) modes.

TE modes have non-vanishing E_x, E_y, H_z components while TM modes have non-vanishing H_x, H_y, E_z components. Under this decomposition, defining $\mathbf{r}_{\shortparallel}$ as the position in the x-y plane, (2.2) and (2.3) become two scalar equations that can be used in place of the Master equations in the discussion that follows on 2.1.2:

$$
\begin{cases}
\widehat{\mathsf{L}}_\mathsf{H} \mathbf{H}_z(\mathbf{r}_{\shortparallel}) = \left(\dfrac{\omega}{c}\right)^2 \mathbf{H}_z(\mathbf{r}_{\shortparallel}) & \text{for TE modes} \\[2ex]
\widehat{\mathsf{L}}_\mathsf{E} \mathbf{E}_z(\mathbf{r}_{\shortparallel}) = \left(\dfrac{\omega}{c}\right)^2 \mathbf{E}_z(\mathbf{r}_{\shortparallel}) & \text{for TM modes}
\end{cases}
\tag{2.6}
$$

The fact that the equation for TE modes does not contain the electric field and *vice versa* can be somehow confusing. About that it is necessary to note that the definitions of TE and TM modes can vary from text to text, and are often inverted for electromagnetic guiding structures and Photonic Crystals. The notation used in (2.6) has been introduced by Joannopoulos [15] and will be the one used throughout the text. Although TE,TM modes decomposition is strictly valid only when the calculation domain is homogeneous in the $\hat{\mathbf{z}}$ direction, a similar *quasi TE* and *quasi TM* decomposition can be defined for slab PhCs, if the vertical confinement is achieved. In the following we will indiscriminately talk about TE and TM modes for both 2D and slab PhC

Scale invariance

Another extremely important property of the master equations, directly related to Maxwell's equations properties, is the *length scale invariance*. While the scale of the phenomena occurring in condensed matter is fixed by a number of physical constants (the radius of the atoms, the De Broglie wavelength of the electrons etc.) this is not true in the EM domain, since the mathematical description of an EM wave is the same at every wavelength scale. Let's suppose that $\mathbf{H}_\omega(\mathbf{r})$ is a solution of the master equation with eigenfrequency ω solved inside the

domain described by $\epsilon(\mathbf{r})$. If a scaled down version of $\epsilon(\mathbf{r})$ is considered, such that $\epsilon'(\mathbf{r}) = \epsilon(s \cdot \mathbf{r})$ for some $s > 1$, then the eigenmodes $\mathbf{H}'(\mathbf{r})$ of the smaller domain will be an exactly equally scaled version of the original eigenmodes $\mathbf{H}'(\mathbf{r}) = \mathbf{H}(s \cdot \mathbf{r}$ with scaled frequency $\omega' = s \cdot \omega$. This fact can be easily demonstrated by defining a new set of coordinates $\mathbf{r}' = s \cdot \mathbf{r}$ with $\mathbf{\nabla}' = s \cdot \mathbf{\nabla}$ and substituting into the master equation itself.

The length scale invariance property is dramatically useful because it ensures that, as long as the dielectric dispersion can be neglected, the operating frequency of an PhC can be arbitrarily increased by simply scaling down the whole dimensions of the PhC. This naturally ceases to be true when the frequency behavior of the dielectric function $\epsilon(\mathbf{r}, \omega)$ is considered.

An equivalent *dielectric scale invariance* can be equally demonstrated stating that if a new dielectric function $\epsilon''(\mathbf{r}) = d \cdot \epsilon(\mathbf{r})$ is defined, then the eigenfrequencies scales accordingly to $\omega'' = \omega/\sqrt{d}$ while the eigenmodes are unchanged $\mathbf{H}''(\mathbf{r}) = \mathbf{H}(\mathbf{r})$. clearly even if $\mathbf{H}(\mathbf{r})$ is unchanged the relation between $\mathbf{H}$ and $\mathbf{E}$ is modified by (2.5).

2.1.2   Photonic Band Gap

As it is often the case interesting properties arise on master equation's solutions if symmetries of the equation itself are considered. Every symmetry is described by an operator $\widehat{S}$ under which the Master equation is invariant, the master equation $\widehat{\mathrm{L}}_\mathrm{H}$ is said to *possess the $\widehat{S}$ symmetry* its commutator with $\widehat{S}$ is null ($[\widehat{S}, \widehat{\mathrm{L}}_\mathrm{H}] = 0$). Knowing that the symmetry properties of $\widehat{\mathrm{L}}_\mathrm{H}$ depend from the symmetries of $\epsilon(\mathbf{r})$ it is possible to demonstrate that if $\widehat{S} = \widehat{\mathrm{T}}_\mathrm{d}$, discrete translational symmetry of the vector $\mathbf{d}$, then the the solutions of the eigenvalue problem (2.7) on the symmetry operator $\widehat{\mathrm{T}}_\mathrm{d}$ are also solutions of the master equation (2.2):

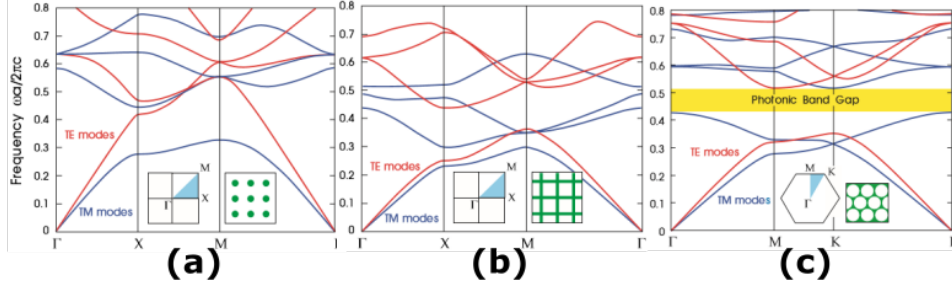$$\widehat{\mathrm{T}}_\mathrm{d} \mathbf{H}(\mathbf{r}) = \mathbf{H}(\mathbf{r} + \mathbf{d}) = \mathbf{H}(\mathbf{r}) \cdot e^{j\mathbf{k} \cdot \mathbf{d}} \tag{2.7}$$

Which is the photonic version of the Bloch theorem. Another more common form of the Bloch theorem is represented by (2.8).

$$\mathbf{H}_{\mathbf{k},n}(\mathbf{r}) = \mathbf{U}_{k,n}(\mathbf{r}) \cdot e^{j\mathbf{k} \cdot \mathbf{r}} \quad \forall \mathbf{k} \in 1^\mathrm{st}\mathrm{BZ} \tag{2.8}$$

Where $1^\mathrm{st}\mathrm{BZ}$ is the *first Brillouin Zone* and $\mathbf{U}_{\mathbf{k},n}(\mathbf{r})$ is a periodic function that is invariant under $\widehat{\mathrm{T}}_\mathrm{d}$:

$$\widehat{\mathrm{T}}_\mathrm{d} \mathbf{U}(\mathbf{r}) = \mathbf{U}(\mathbf{r} + \mathbf{d}) = \mathbf{U}(\mathbf{r})$$

Fig. 2.2: Photonic Band Structure (PBS) for different lattice topologies, images from [15]

What changes with respect to the usual Bloch theorem found in Solid State Physics is the fact that the quantities are now vectorial, but the physical meaning is unchanged. Photons propagates in discrete translationally symmetric media as Bloch waves, moreover if TE, TM decomposition holds true (2.8) splits into two fully scalar problems. The mathematical meaning of the Bloch theorem is that for every $\mathbf{k} \in 1^{st}BZ$ an eigenvalue problem on the symmetry operator is set. The solutions, which can be computed employing various numerical or analytical methods, are a *discrete* set of orthonormal modes $\mathbf{H}_{\omega,n}$ with eigenfrequencies $\omega(\mathbf{k})_n$ that continuously depend on $\mathbf{k}$. The function $\omega(\mathbf{k})$ is the Dispersion Relation, and nearly all the physical properties of the electromagnetic mode can be inferred from it. This leads to the formation of frequency bands, identified by the sub-index n, with a mathematical meaning equal to the energy bands of solids. A Photonic Band Gap (PBG) is obtained when an interval of frequencies $\Delta\omega$ does not contain real solutions of (2.8)[3]. The PBG can also arise for TE-only modes, as well as TM-only. This is the case of most common planar PhCs as the square lattice of dielectric rods (2.2a, TM-only) the square lattice of dielectric veins (2.2b, TE-only) or the hexagonal lattice of dielectric rods (TE or TM only). A PBG for both polarizations is called *Complete PBG* and can be achieved, with dielectric structures, with the hexagonal lattice of air columns (2.2c).

2.2 Localization of states in PhC

Confinement of EM energy is an important issue in engineering. Microstrips, transmission lines, waveguides, coaxial cables, are all different

---

[3]Actually an analytical treatment of (2.8) shows that solutions always exist, but either $\mathbf{k}$ or ω might be imaginary thus the corresponding "mode" is not a real mode but an evanescent one, that is not propagating

ways to guide millimetric and micrometric waves. When the visible or the infra-red spectrum is considered, however, metals ceases to be sufficiently good conductors and Ohmic losses make the aforementioned systems a non convenient choice. What is normally employed in conventional TLC devices is *index guiding*, a mechanism for which light is confined into regions with high refractive index via total internal reflection. Index guiding is the working principle of optical fibers, but dielectric media with high refractive index are often dispersive and presents non-linearities. Photonic Crystals (PhC) provide the possibility to guide EM energy in the air, as in metallic waveguides, but using dielectric materials as mirrors, that shows considerably lower losses up to optical frequencies.

2.2.1   PhC states

It is now important to make a remark about the different types of EM states that might be found in PhC. A *state* is a particular solution of (2.8) with its peculiar dispersion relation $\omega_n(\mathbf{k})$ and eigenmode $\{\mathbf{E}, \mathbf{H}\}_n$, we can distinguish between different kind of states:

A **Bulk State** is a solution of (2.8) calculated for the bulk PhC, that is the structure modeled as infinitely periodic, without any defect. EM waves with frequencies and wave-vectors that are points of $\omega_n(\mathbf{k})$ propagates inside the Photonic crystal. Bulk states are usually divided into *dielectric bands* and *air bands*. Dielectric bands are states with EM energy concentrated on the high index regions of the lattice while air bands are concentrated on the lower index materials, that in some cases (dielectric rods in air, for example) could be air. Bulk states are however delocalized inside the crystal, this make them somehow comparable with valence and conduction band states in semiconductors, where electrons are delocalized in all the crystal[4]. Accordingly to the variational principle Th.1 it is evident that dielectric bands have normally lower frequency that air bands. If a PBG is present in the Photonic Band Structure (PBS) it is between these two classes of bulk states.

Localized States are states that do not propagate inside the PhC and do not properly solve (2.8), however they become available thanks to some defect in the bulk crystal, EM energy is consequently strongly localized inside the defect. Also called *defective states* theses might be compared to the energy levels of dopants that appears inside the band-gap of a doped semiconductor[5] with an analogy that has only physical

---

[4]There is, however, no parallelism between dielectric-valence band and air-conduction band.

[5]Analogies with Photonic Crystals and semiconductors stops here, since the working
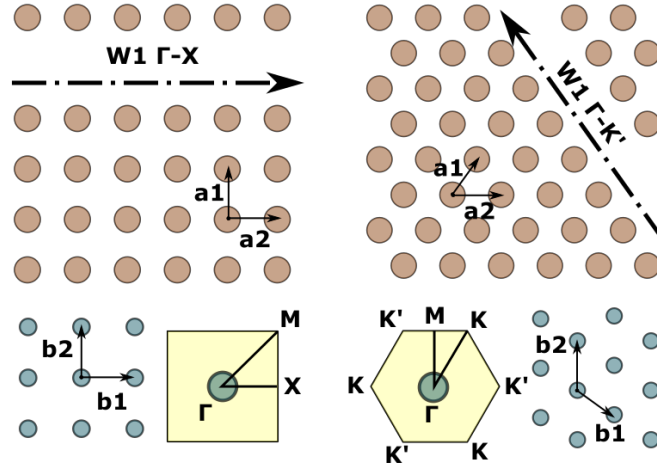
Fig. 2.3: Left: Square lattice, Right: Hexagonal lattice. Direct(orange) and Reciprocal(blue)lattices with primitive vectors are illustrated. Shaded yellow: $1^{st}BZ$ with relevant edge points. Dashed lines: W1 PhC waveguides

meaning in the localization of the wave-function (or EM energy).

Surface States are also states that do not propagate inside the PhC thus they have frequencies in the PBG, the difference between defective and surface however is that the latter are not bounded to a defect, but arise at the interface between a PhC and a different material. Terminations of Photonic Crystals in air may support surface states or not, depending on the shape of the termination. Often "Surface" states and "Edge" states are used as synonyms but strictly speaking terminations of slab PhC gives rise to Edge states while 2D and 3D terminations give rise to surface states. A surface state is delocalized across all the interface to which is bounded.

2.2.2 Line defects

Planar PhC waveguides are obtained with line defects in 2D or Slab PhCs, that is by carving a waveguide inside a bulk PhC (as schematically illustrated in Fig.2.3. Depending from the cross-section of the waveguide and from the termination of the confining bulk PhC there are various classification for PhC waveguides.

The most common are Wx waveguide, with $x = d/a_0$ being d the width of the waveguide and a_0 the lattice constant of the crystal. For example W1 waveguides can be obtained by removing a row of dielectric rods from a 2D lattice of rods in air. W0.8 waveguides would

principles of PhC guiding and conduction in semiconductors are completely different
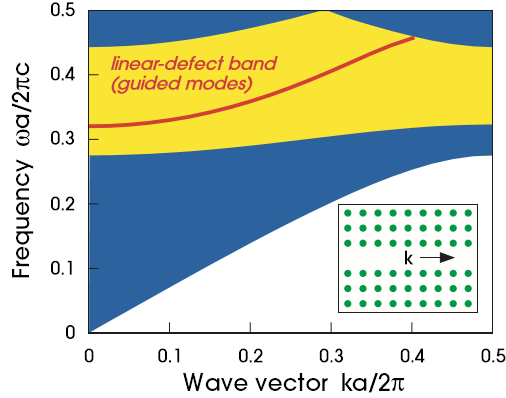
Fig. 2.4: Dispersion relation of a W1 waveguide in a 2D PhC. Bulk modes in blue, PBG in yellow and defective state in red. Image from [15]

be obtained from a W1 waveguide and moving one of the waveguide's edge $0.2a_0$ closer to the other. Another parameter is the direction of the waveguide in the reciprocal space of the lattice: $\Gamma - X$ waveguides are oriented along the $\Gamma - X$ direction of reciprocal space. PhC waveguides are normally of the $\Gamma - X$ (Fig. 2.3 left) or $\Gamma - K$ (Fig. 2.3 right) type, but $\Gamma - M$ are also theoretically possible.

Note that M,X,K points of the reciprocal lattice have a number of topologically equivalent points, there are 4 M and X-points in a square lattice and 6 M-points in an hexagonal lattice. An hexagonal lattice has instead only 3 K-points and 3 K'-points, being K' the space inversion of K. K and K' are usually topologically equivalent (valley degeneracy) but not always, their difference will be relevant in the next chapters.

Localized line defect states in PhCs can be inspected by means of the super-cell method. Let's assume to deal with a linear defect along the y direction of a 3D PhC. From the physical point of view we inspect the propagation inside the defect that ultimately results in a series of modes identified by dispersion relations $\omega_d(k_y)$. If for any $(\hat{k}_x, \hat{k}_z)$ the point $\omega_d(\hat{k}_x k_y \hat{k}_z)$ lies on a bulk state band then the mode is not purely confined within the defect and will leak into the crystal. Repeating the procedure for every k_y leads to the construction of the *projected band structure* of the PhC as a continuum of bulk modes with possibly a *defective band* which is the allowed defect state inside the PBG. Fig. 2.4 show the dispersion relation of a W1 waveguide for a 2D PhC. From a numerical point of view the method is applied by modeling a unit cell with various reticular constants per side of the defect and only one constant in length. Periodic boundary conditions are imposed along the direction of propagation and the eigenmodes are calculated

for every value of k, that is the phase delay between the two periodic boundaries. This corresponds to looking for $\omega_d(k_y)$. Eigenfrequencies inside the previously calculated band gap, if any, will represent guided modes.

Since complete band gaps for 3D PhC are hardly obtainable vertical confinement in PhC waveguides is obtained either with mirrors or with total internal reflection (i.e. slab crystals are used). The operating frequency range of a PhC platform coincides with its PBG, once a PBG is obtained various practical devices can be realized employing carved waveguides and other types of defect, that operates inside the PBG.

2.2.3 point defects

A point defect is obtained when a single point of the lattice is perturbed (by displacement, index perturbation, removal of a lattice point, perturbation on some crystal parameter). Since point defects give rise to truly stationary and resonant states their description goes beyond the domain of this work, that deals with guiding structures. However point defects are of extreme importance in engineering since they permits to realize cavities with very high quality factors, which in turn permits to manipulate the effective density of states enabling groundbreaking capabilities for a wide spectrum of applications [27, 45]

2.3 Topological insulators

Topology is famously the branch of mathematics dealing with quantities that change step-wise. The most famous example of topological invariant is classically the *number of holes*, or *genus* of a solid object. Under a topological point of view a sphere, a spoon and a bowl possess the same topological order: they have no holes. On the contrary a teapot and a doughnut possess a different topological order because they have a single hole. Every object can be described accordingly to the number of holes it have, and these numbers have to be integers (since it is not possible to have 1/2 holes). Without entering into the mathematical details of topology, which is not the scope of this thesis, the application of topology to quantum field theory revolutionized the understanding of a number of physical phenomena occurring at low temperature until in 2016 David J. Thouless, F. Duncan M. Haldane and J. Michael Kosterlitz were awarded the Nobel prize in physics *"for theoretical discoveries of topological phase transitions and topological phases of matter"*.

It is beyond the author's reach to provide clear physical explanation of Topology applied to solid state physics, thus this theoretical introduction to Topological Insulators will be limited to the description of the phenomenon along with a brief historical review of the steps that lead Haldane to the formulation of a theoretical model in which Quantum Hall Effect (QH) was predicted to happen without an external magnetic field, hypothesis that eventually was confirmed experimentally in 2014.

2.3.1   Time reversal and quantum hall effect

The first observation of QH happens in 1980 by Klitzing [41] who is awarded the Nobel Prize in 1985. In QH a 2D quantum gas of electrons subject to a strong perpendicular magnetic field shows a quantized hall conductance $\sigma_H = n \cdot e^2/h$ where n is an integer that abruptly changes by discrete steps with the decrease of the magnetic field intensity. The discrete jumps of the conductance are due to the fact that electrons move in cyclotron motions with energies that assume only discrete steps (Landau levels) due to the 2D confinement of the gas. The accurate measurement of the unit hall conductance to one part in a billion led, in 1990, to the definition of a new standard for the resistance that takes the name of Klitzing and is defined as the inverse of the unit step of the hall conductance in QH: $R_k = h/e^2 \approx 25182.807\Omega$. However it is Thouless in 1982 [39] to classify QH as a topological state of matter, recognizing in the integer n a topological in-variant commonly known as *Chern number*[6] $\mathcal{C}$.

The classification of QH as a topological state of matter permitted to make a fundamental distinction between the bulk energy gap arising in QH phase and in classical insulating state, where even energy gaps exists, but there's no conduction. Energy gap of QH states arises because the applied magnetic field splits electrons energies in landau levels, but every level is occupied by at least one electron[7], while in conventional insulators upper energy bands are not occupied by electrons. It is now possible to say that conventional insulators are TI with $n = 0$ [17], and it is also clear that TI shows conducting states at the samples edge. One of the peculiarity of QH topological state is that the 2D gas provides electronic conduction only at along one direction, which is consistent with the cyclotron motion of the electrons, however seemingly breaks time-reversal invariance. Time-reversal invariance is

---

[6]Strictly speaking it is known as the TKNN invariant, which is the *first* Chern number, but it's not the case to split hairs here

[7]Actually Landau levels are higly degenerate for strong magnetic field thus nearly all the electrons of a sample can sit on few landau levels, which is the condition for QH state.

a symmetry that all physical systems has to satisfy, and basically tells that the behavior of the physical system has to be symmetric under time reversal. In the case of QH time reversal invariance seems to be violated since electron flow is unidirectional. In reality the apparent violation of time reversal is only due to the fact that an external magnetic bias is applied to split Landau levels, under time reversal the magnetic field changes its sign and invariance is restored. This is a common trick to inspect physical properties of seemingly time-reversal variant physical systems.

2.3.2   Haldane and Kane-Mele models

Just 7 years after the discovery of QH and 4 years after its categorization as Topological State of matter, Haldane proposed in 1987 a theoretical model in which topologically characteristic levels (i.e. with a non-null Chern number) are splitted without an external magnetic bias but as a consequence of spontaneous magnetic ordering due to the electron spin [9]. In the haldane Model time-reversal invariance has to be preserved by introducing an external periodic magnetic field, that has no net flux. Haldane model has been used by Kane and Mele in 2005 [16] to predict such topologically characteristic band gap to happen in a 2D sheet of graphene due to Spin Orbit Interaction (SOI). The fundamental result obtained by Kane and Mele is an the effective Hamiltonian for electrons in the A(B) sub-lattice and K(K') points of graphene reciprocal lattice. The total electronic wave-function is expanded as a four component wave-function in which every component is a vector that describing the basis states at the A(B) sub-lattice sites and with K(K') momentum:

$$\Psi(\mathbf{r}) = [u_{AK}, u_{BK}, u_{AK'}, u_{BK'}]\psi(\mathbf{r})$$

The effective Hamiltonian is written as (2.9)

$$\mathcal{H} = -j\hbar v_f \psi^*(\sigma_x \tau_z \delta_x + \sigma_y \delta_y)\psi + \mathcal{H}_{\text{SO}} \qquad (2.9)$$

being,

$$\mathcal{H}_{\text{SO}} = \Delta_{SO}\psi^* \sigma_z \tau_z s_z \psi$$

In (2.9) σ and τ are Pauli matrices acting respectively on the A(B) sublattices and on the K(K') valley of reciprocal space and every matrix product is implied as a kroneker matrix product. The additional term s_z is still a Pauli matrix but acting on the electron spin. Without

the $\mathcal{H}_{\mathcal{SO}}$ term the electron energies are degenerate in the K(K') points. A topologically trivial band gap would be obtained with a term proportional to σ_z, as a staggered sublattice potential, in this case the degeneracy is removed between A and B sublattices, but no topological properties arise. On the contrary a term proportional to $\sigma_z \tau_z$ would introduce a band gap with inverted sign for the K(K') valley, leading to topologically characteristic behavior but the term would be odd under time-reversal invariance thus is not allowed in a physical system. Without the s_z term the Kane-Mele hamiltonian is equivalent to the Haldane models, and is not physical but introducing s_z that changes its sign for spin-inversion leads to a time-reversal symmetric term since the spin is odd under time reversal, that is allowed. In Ref. [16], to which we refer for a more precise and deep explanation of the phenomenon, Kane and Mele theoretically show that this topologically characteristic state is allowed in graphene though the small spin-orbit interaction (leading to a very small Δ_{SO} term) and that the result is a Topologically Insulating state. The effect is known as QSH as a consequence of the spin-dependence of the induced gap sign. An important consequence of QSH is that edge currents of QSH TI are spin-polarized, thus electrons with different spin are transported on opposite directions. A side result illustrated in Ref [16] is the robustness of topologically protected edge states to small enough perturbations. In particular the effect of a perturbation λ_p introducing a gap that is not proportional to $\sigma_z \tau_z s_z$ is studied. the overall bandgap induced by the two concurrent phenomena is given by (2.10)

$$E_g = 2(\Delta_{SO} - \lambda_p) \tag{2.10}$$

Since the sign of the gap induced by non-SOI effect is of inverted sign with respect to the Topological gap it is the relative strength between Δ_{SO} and λ_p to characterize the topological properties of the sample. The latter is a clear example of topological phase transition: In order to annihilate the topological band gap induced by Δ_{SO} it is necessary to close the gap and to reopen it since the two gaps have a different topology and cannot be continuously connected.

Although Spin Orbit Interaction in graphene is too weak to overcome other effects and ultimately permit a topological phase transition with available technologies, the theoretical predictions of Kane and Mele were experimentally demonstrated in 2006, when QSH and TI states without external magnetic field have been observed, not in graphene, but in HgTe quantum wells both by Barnevig *et al.* [1] and by Konig *et al.* [19].
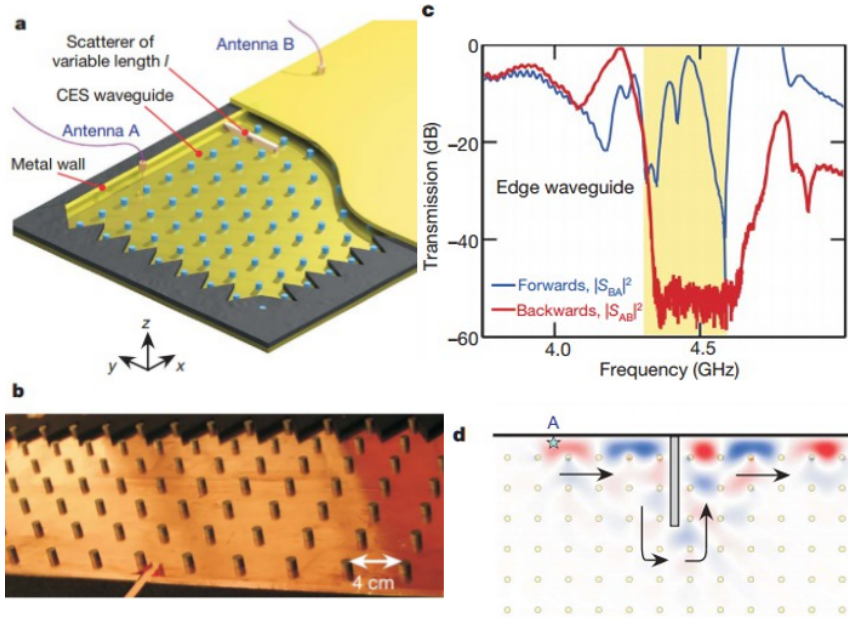
Fig. 2.5: Photonic QH "Chiral Edge States" (CES) as observed by Wang *et. al*, image from Ref. [44]

2.3.3 Photonic Topological Insulators

The fact that his model predicted QH without electron-electron inter-actions but only because of time-reversal symmetry breaking convinced Haldane that an analogous of QH could be present also for photonic systems in the presence of time-reversal breaking. In 2008 a collaboration between Haldane and Raghu resulted in a couple of papers in which a Photonic QH was predicted in PhCs with broken time reversal [32] along with a theoretical proposal for the realization of QH Photonic Topological Insulators (PTI) employing nonreciprocal ferromagnetic media in the presence of a uniform magnetic field [10].

Unidirectional edge states in photonic systems was a very attracting feature and a number of researchers tried to realize Haldane's theoretical proposal. The first experimental evidence of unidirectional backscattering-immune electromagnetic states (also called Chiral Edge States (CES)) came from Wang *et al.* [43,44] who directly implemented Haldane's proposal in a slab PhC of magnetized ferrite rods vertically confined with metallic planes. The presence of an external magnetic field breaks time reversal symmetry and the structure becomes non-reciprocal. Chiral Edge States are observed, that flow along a single direction without reflecting in the presence of even large defects (Fig. 2.5). Floquet Topologial Insulators, arising because of a time periodic

potential perturbation, are another theoretical proposal for TI. The photonic counterpart of a Floquet TI has been demonstrated in 2013 by Rechtsman *et al.* [33] using helical waveguides evanescently coupled in an honeycomb lattice. The periodic potential is imitated by the light flowing into the helical waveguides thus no external field is required. Although the Floquet TI by Rechtsman *et al.* permitted the first experimental demonstration of Photonic Topologically Protected Surface States (TPSS) without external fields, it didn't yet provide a Photonic analogue for QSH TI. In 2012 a theoretical proposal by Khaenikaev *et al.* matematically demonstrated an equivalence between Spin Orbit Coupling and Bianisotropy as long as the opening of a Topologically Protected (TP) PBG is concerned [18]. In his theoretical structure a PTI directly emulating QSH was realized employing an hexagonal lattice of rods with intrinsic bianisotropic responce. A similar structure was realized in 2015 by Slobozhanyuk and Khanikaev himself [37]. A different proposal for QSH PTI, also made by the group of Khanikaev, was theoretically advanced in 2015 [23] and experimentally demonstrated in 2016 [20], based on an hexagonal lattice of metallic rods exhibiting bianisotropic response upon z-symmetry breaking perturbations. Since the latter QSH PTI is the main subject of this Thesis work, a more accurate discussion of the platform in object is given in the next chapter.

As a conclusion to this Chapter it is important to note that after this thesis work begun new photonic structures where realized employing the same unperturbed base of metallic Photonic Graphene in order to separatedly break time and space inversion symmetry. Interfaces between heterogeneous PTI where thus numerically inspected [24] as a further investigation of Topological Edge States. Finally a theoretical proposal of an all-silicon PTI has been recently advanced [25] without any experimental evidence yet.

Topologically Protected MetaWaveguides

W AVE nature of light represents a remarkable problem when it comes to integrating photonic circuits and devices. Waveguide bends are prohibited with a radius smaller than the wavelength thus intrinsically limiting integration. Photonic Crystals (PhC) based waveguides (otherwise called Meta-Waveguide (MW)) [15] shows transmission spectra around curved paths that are several times higher than conventional index-guiding based waveguides but still not high enough to enable integrated photonic circuits design. Moreover PhC are extremely sensitive to slight changes in the geometrical parameters or defects, which usually creates defective states with unwanted resonating behavior. Such high sensitivity is still not compatible with the tolerances of standard low cost technologies if frequencies higher than few hundredths of GHz are considered.

Topological Protection of EM waves could represent a possible solution to both the problems of transmission around sharp bends and sensitivity to crystal defects. Topologically Protected Surface States (TPSS) are indeed insensitive to all classes of lattice defects that leaves unchanged the topological properties of the bulk crystal and have been already demonstrated [24, 25, 37, 44] to enable perfect transmission over a wide frequency range even in the presence of large scatterers, defects and sharp bends of the wave path.

As already discussed the last decade has seen lots of efforts being made to achieve topologically protected transport of light, and various platforms for realizing Photonic Topological Insulators (PTI) have been theoretically proposed and experimentally demonstrated. The

global trend in these researches seems to be that of realizing photonic structures with similar mathematical description to electronic system that are known to exhibit non trivial topological behavior (Quantum Hall Effect (QH), Quantum Spin Hall Effect (QSH), Quantum Valley Hall effect etc). In this way it is possible to exploit the flexibility of PhC, and particularly the scale invariance of the Master Equations, to emulate conditions that would be hardly observable in condensed matter due to parasitic effect, experimental conditions, and scale of the involved phenomena. G.Shvets and A. Khanikaev with their groups at Texas University and New York University have been leading the research on time-reversal preserving PTIs and proposed in the last 5 years a number of structures [18, 20, 23, 25, 37] relying on bianisotropy to open non-topologically trivial band gap in *spin-degenerate* Photonic Crystals. In their works Bianisotropy, or cross-polarization coupling, configures as the photonic analogue of Spin Orbit Interaction (SOI) leading to QSH topological Insulating state, so far observed in HgCdTe Quantum Wells [1, 11, 19].

In this chapter the mathematical formulation and the guiding properties of one of the recent proposals for QSH PTI are studied. The very first section has to be intended as an overview of the steps required to turn a PhC into a PTI that will be extensively demonstrated in the subsequent few sections. The last two sections deals with how to combine two PTIs to realize a Topologically Protected Meta Waveguide (TPMW) able to guide light via TPSS. In that scope the TPSS properties will be intuitively derived from the super-cell Photonic Band Structure (PBS).

3.1   General concepts

Although the proposed Bianisotropic Photonic Crystal (BPhC) doesn't rely on non-reciprocal media such as gyromagnetic materials [44] or metamaterials [18,37], bianisotropy requires some degree of manipulation of the magnetic response which is usually not provided by common dielectrics. The proposed crystal makes use of surface currents (due to the electric field) to induce a magnetic field, actually coupling orthogonal components of electric and magnetic fields thus achieving a bianisotropic response. Metallic materials are required to obtain surface currents. This is one of the main limiting factors in increasing the operating frequencies since normal materials ceases to be good conductors when high frequencies are considered. In Fig. 3.1 the main geometry of the PhC is showed. The crystal is an hexagonal lattice of rods, numerically modeled as Perfect Electric Conductor (PEC). Vertical confinement is achieved through a couple of metallic mass-planes.
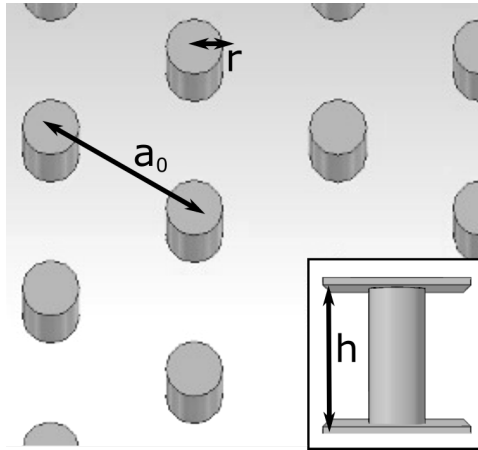
Fig. 3.1: Schematized geometry of PhC

As it has been shown in the first chapter the slab geometry of the crystal permits to subdivide the eigenmodes in two orthogonal Transverse Electric (TE) and Transverse Magnetic (TM) classes [15]. First order TE TM eigenmodes are illustrated in Fig. 3.8 where the bipolar nature of the modes and the orthogonality of pairs can be appreciated. Such modes have degenerate eigenfrequencies in the K(K') points of the PBS thanks to the hexagonal symmetry of the lattice. Accidental degeneracy can be obtained for TE and TM couples so that four degenerate bands touches each other in Dirac-like dispersion around the K(K') points of the PBS.

A z-symmetry breaking perturbation as the one depicted in Fig. 3.2 has the effect of coupling TE and TM bands by introducing bianisotropy, as will be demonstrated employing perturbation theory. The perturbed photonic crystal (Fig.3.2, right) will be in the following referred to as a Bianisotropic Photonic Crystal (BPhC) in comparison with the simple unperturbed PhC (Fig.3.2, left).
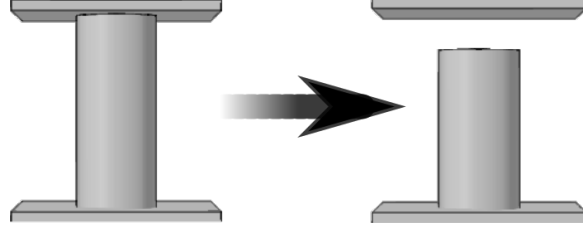
Fig. 3.2

Hybridization of TE TM band can be effectively mapped in the vicinity of the K(K') point to the Kane-Mele hamiltonian of graphene [23]. Cross-polarization coupling (bianisotropy) willb be shown to act on the basis of degenerate EM modes of the unperturbed PhC in the same way that SOI acts on spin-degenerate electronic bands(i.e. opening a topologically non trivial bandgap, as in 2.3.2). The perturbed Hamiltonian shows hence non trivial topological order turning the perturbed BPhC into a QSH PTI.

3.2 W-S cell and numerical analysis

An hexagonal lattice with its unitary cell is illustrated in Fig. 3.3a. Having defined the direct space vectors $\mathbf{r}_1$ and $\mathbf{r}_2$ and the reticular constant a_0 an hexagonal lattice is formally defined by:

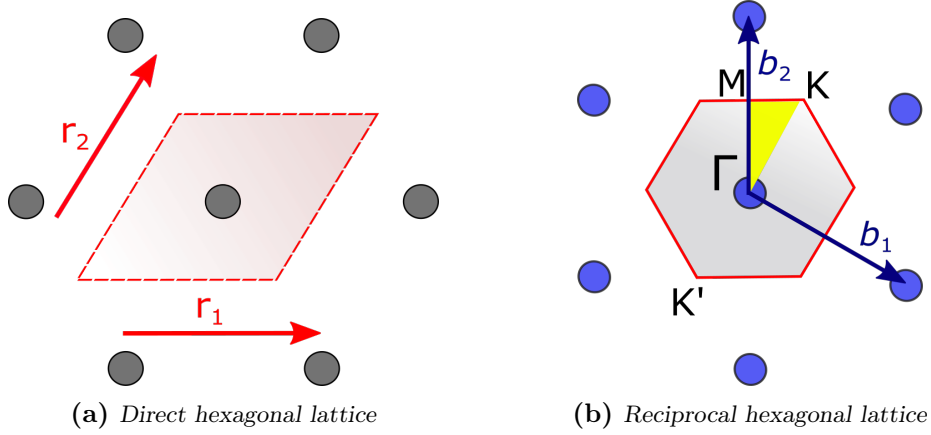$$\begin{cases} |\mathbf{r}_1| = |\mathbf{r}_2| = a_0 \\ \phi = \pi/3 \end{cases} \tag{3.1}$$

where ϕ is the angle between $\mathbf{r}_1$ and $\mathbf{r}_2$. It is useful to describe such vectors in term of Cartesian coordinates, referring to Fig. 3.3a we simply recall

$$\mathbf{r}_1 = a_0 \cdot \hat{\mathbf{x}}$$
$$\mathbf{r}_2 = \frac{a_0}{2} \cdot \left(\hat{\mathbf{x}} + \sqrt{3}\hat{\mathbf{y}} \right) \tag{3.2}$$

Where $\hat{\mathbf{x}}, \hat{\mathbf{y}}$ are versors of the x,y directions.
If $\mathbf{r}_3 = \hat{\mathbf{z}}$ is assumed, it is now possible to derive the expression of the

(a) *Direct hexagonal lattice*   **(b)** *Reciprocal hexagonal lattice*

Fig. 3.3: Direct (a) and reciprocal (b) space of an hexagonal Bravais lattice.
In b) the Irriducible Brilouin Zone is shaded in yellow, important
edge points of the 1$^{\text{st}}$BZ are indicated

reciprocal space vectors $\mathbf{b}_1$ and $\mathbf{b}_2$ [30] obtaining:

$$\begin{aligned}
\mathbf{b}_1 &= \frac{2\pi}{\sqrt{3}a_0} \cdot \left(\sqrt{3}\hat{\mathbf{x}} - \hat{\mathbf{y}}\right) \\
\mathbf{b}_2 &= \frac{4\pi}{\sqrt{3}a_0} \cdot \hat{\mathbf{y}} \\
\mathbf{b}_3 &= 0
\end{aligned} \tag{3.3}$$

Where $\mathbf{b}_3 = 0$ has been artificially imposed due to the vertical confine-
ment that prevents propagation in the $\hat{\mathbf{z}}$ direction.
The reciprocal space generated by $\mathbf{b}_1, \mathbf{b}_2$ vectors is illustrated in Fig.
3.3b together with the Wigner-Seitz cell. From (3.3) it is easily found:

$$\begin{cases} |\mathbf{b}_1| = |\mathbf{b}_2| = |\mathbf{b}| = \dfrac{4\pi}{\sqrt{3}a_0} \\ \phi = 2\pi/3 \end{cases} \tag{3.4}$$

In which ϕ represents the angle between vectors $\mathbf{b}_1, \mathbf{b}_2$. We find the
well known result for which the reciprocal lattice of an hexagonal Bra-
vais lattice is still an hexagonal Bravais lattice rotated by $\pi/3$. It is
now possible to obtain the coordinates of the relevant edge points of
the First Brillouin Zone (1$^{\text{st}}$BZ)(from which the Irriducible Brilouin
Zone (IBZ) will be defined) in terms of $\mathbf{b}_1$ and $\mathbf{b}_2$ vectors. Defining
$\hat{\mathbf{b}}_1, \hat{\mathbf{b}}_2$ as the unitary versors identified by $\mathbf{b}_1, \mathbf{b}_2$ directions, the points
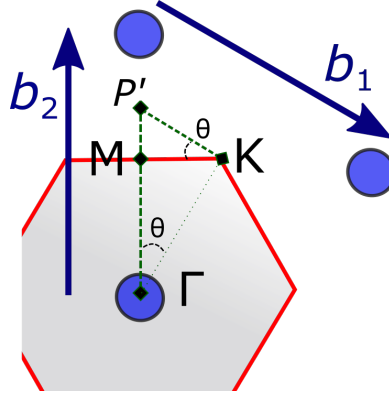
Fig. 3.4

Γ and M are easily obtained from Fig. 3.3b:

$$\begin{cases} \Gamma & = 0 \\ M & = \dfrac{|\mathbf{b}|}{2} \cdot \hat{\mathbf{b}}_2 = \dfrac{2\pi}{\sqrt{3}a_0} \cdot \hat{\mathbf{b}}_2 \end{cases} \qquad (3.5)$$

By employing the construction depicted in Fig. 3.4 it is finally possible to obtain also the K point, being $\theta = \pi/6$:

$$\overline{MK} = \overline{\Gamma M} \cdot \tan\theta$$

$$\overline{P'K} = \frac{\tilde{M}K}{cos\theta} \Rightarrow \overline{\Gamma M} \cdot \frac{\sin\theta}{\cos\theta^2} \qquad (3.6)$$

$$\overline{MP'} = \overline{P'K} \cdot \sin\theta \Rightarrow \overline{\Gamma M} \cdot \tan\theta^2$$

Since $\overline{\Gamma M} = |M|$ (that has been previously calculated) it is easy to find now $(\hat{\mathbf{b}}_1, \hat{\mathbf{b}}_2)$ components of K from $\overline{P'K}$ and $\overline{\Gamma P'}$:

$$\overline{P'K} = \frac{|\mathbf{b}|}{2} \cdot \frac{1}{2} \cdot \frac{4}{3} = \frac{|\mathbf{b}|}{3}$$

$$\overline{\Gamma P'} = \overline{\Gamma M} + \overline{MP'} = \frac{2|\mathbf{b}|}{3} \qquad (3.7)$$

Thus finally obtaining:

$$\begin{aligned} K &= \overline{P'K} \cdot \hat{\mathbf{b}}_1 + \overline{\Gamma P'} \cdot \hat{\mathbf{b}}_2 \\ &= \frac{4\pi}{3\sqrt{3}a_0} \left(\hat{\mathbf{b}}_1 + 2 \cdot \hat{\mathbf{b}}_2 \right) \end{aligned} \qquad (3.8)$$

The point K' is obtained by parity inversion of the point K. i.e.

$$K' = -\frac{4\pi}{3\sqrt{3}a_0} \left(\hat{\mathbf{b}}_1 + 2 \cdot \hat{\mathbf{b}}_2 \right)$$

It is important to note that the IBZ depicted in Fig. 3.3b is defined with
a K point as a corner. Nevertheless K and K' points are not equivalent
because no reciprocal space unit vector can be used to connect K and
K' points. There are 3 K points and 3 K' points in the 1$^{\text{st}}$BZ alternating
along the edge of the W-S cell. The PBS is equivalent both in the K and
K' points but the eigenmodes are related by time-inversion symmetry
and are not, in general, the same. It is possible to look at whichever
among the 3 K and 3 K' points if the band structure is considered since
each mode in K must have a Kramer degenerate pair at K'. Although
in literature it is common to derive K' with parity inversion from K,
in this context it is preferable to use the K' point right next to the
already derived K point. Table 3.1 synthesizes the last results:

|	$\hat{\mathbf{b}}_1$	$\hat{\mathbf{b}}_2$
Γ	0	0
K	$|\mathbf{b}|/3$	$2|\mathbf{b}|/3$
M	0	$|\mathbf{b}|/2$
K'	$-|\mathbf{b}|/3$	$|\mathbf{b}|/3$

Table 3.1: Values of the reciprocal vectors for the relevant points of the
1$^{\text{st}}$BZ. The path $\Gamma-K-M-\Gamma$ is usually referred to as Irreducible
Brillouin Zone.

The unit cell modeled under HFSS environment is illustrated in Fig.
3.5. PEC boundary conditions have been used for the z confinement
while Master-Slave boundaries hare defined to model a bulk crystal.
Master-Slave couples of boundaries are parallel faces of the unit cell
for which a phase difference $\Delta\Phi$ is specified. At each value of $\Delta\Phi$
corresponds a unique $\mathbf{k}$ of the Wigner-Seitz cell. If we denote by P_1
and P_2 the phases relatives to the reciprocal lattice vectors $\mathbf{b}_1, \mathbf{b}_2$ the
couple of values (P_1, P_2) that corresponds to the IBZ corners $\Gamma K M$ can
be directly obtained from table 3.1 applying the substitution $|\mathbf{b}| \to 2\pi$
hence obtaining the values in table 3.2 (expressed in degrees for this is
the notation employed by HFSS)

The complete Photonic Band Structure can be computed by per-
forming a parametric analysis on the eigenmodes of the structure letting
the relative phases P_1, P_2 vary along the path $\Gamma - K - M - \Gamma$ Such
path, that corresponds to the edge of the yellow-shaded area in Fig.
3.3b is called Irriducible Brilouin Zone (IBZ). All the relevant phenom-
ena occurring in the reciprocal space will happen on the edges of the
IBZ, where the Bragg condition is satisfied.

	P_1	P_2
Γ	$0°$	$0°$
K	$120°$	$240°$
M	$0°$	$180°$
K'	$-120°$	$120°$

Table 3.2: Values of relative phase between Master-Slave boundary couples 1 and 2 for relevant points in the 1stBZ
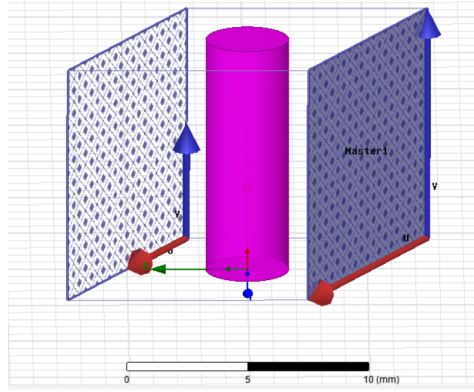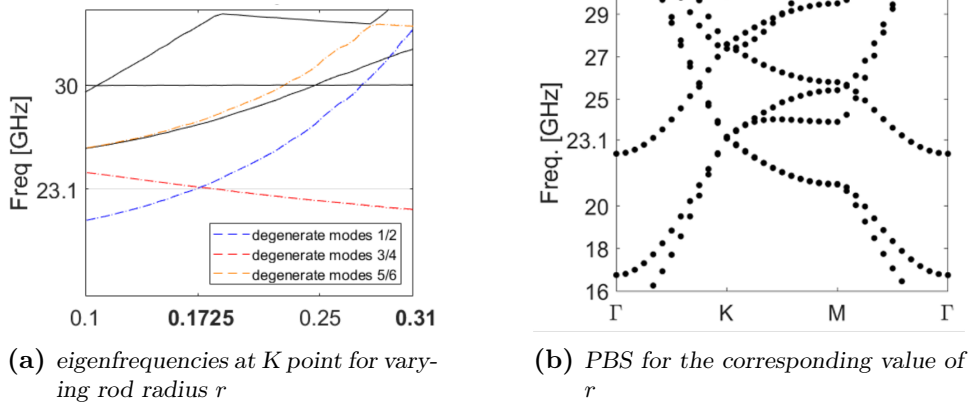

Fig. 3.5: Unit Cell modeled with HFSS. A single couple of Master-Slave boundaries is highlighted

3.3 TE-TM modes degeneracy

Degeneracy of TE and TM polarized couples is ensured (*protected*) by the simultaneous presence of time reversal and inversion simmetry [32]. What it is required in order to open a topologically non trivial bandgap is cross polarization degeneracy (usually called spin-degeneracy for reasons that will be clear in the following) between TE and TM modes [18]. Accidental degeneracy can be obtained with a numerical analysis by calculating the PBS in the K point of the IBZ for various values of the rods radius r.

The parametric analysis depicted in Fig. 3.6a shows two couples of degenerate modes that becomes four fold degenerate for $r = r_0 = 0.1725 \cdot a_0$ This will be in the following the value assumed for r if not otherwise stated. The Dispersion relation of the degenerate PhC(Fig. 3.6b) have been calculated using first-principles eigenmodes analysis on the commercial software HFSS ^{TM}. A double Dirac Cone emerges in correspondence of the K(K') points at a frequency $f = 23.1$ GHz.

(a) *eigenfrequencies at K point for varying rod radius r*

(b) *PBS for the corresponding value of r*

Fig. 3.6: PhC parameters: $a_0 = 10mm$, $h_0 = a_0$
$r = 0.1725a_0$ for 3.6b

It is also possible to compute the full 3D Dispersion relation of the Photonic Crystal. In Fig. 3.7 the full Photonic Band Structure of the PhC (3.7a) is compared with the full band structure of graphene (3.7b). It is evident the similarity in the appearance of 6 Dirac Cones in the K(K') points of the band structure.
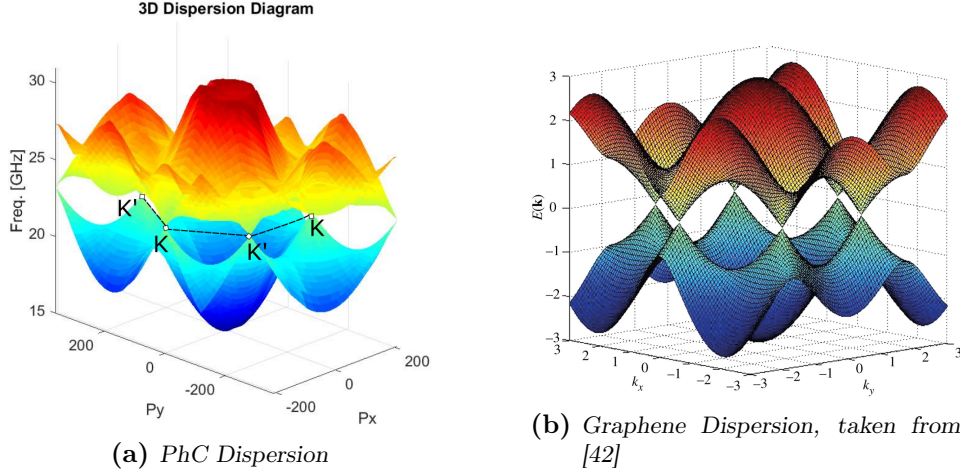
3.3.1 Unperturbed eigenmodes analysis

Several interesting properties can be underlined for the unperturbed crystal eigenmodes, such properties will prove useful in the further development of the perturbation theory.
Fig. 3.8 shows the first two lower order TE/TM modes of the unperturbed PhC. The following observations can be summarized:

- TM modes are z-independent while TE modes are z-dependent (z-dependence is not shown). This is reasonable because TE modes have vanishing E_z by construction while at the metallic boundaries also $E_x = E_y = 0$ such that a z-dependence is necessary to have non-trivial solution.

- $Z = 0$ plane can be modeled as a perfect magnetic conductor for TE modes thus H_x, H_y fields annihilates at $z = 0$. Z-dependence of TE modes can be expressed as

$$\mathbf{H}_{\text{TE}}(x, y, z) = \mathbf{H}_{\text{TE}}(x, y) \sin\left(\frac{\pi}{h}z\right) \tag{3.9}$$

From which $\mathbf{H}_{x,y,-z} = -\mathbf{H}_{x,y,z}$ and TE modes are anti-symmetric.

(a) *PhC Dispersion*

(b) *Graphene Dispersion, taken from [42]*

Fig. 3.7: Comparison between 3 dimentional band structures of **(a:)** Photonic Graphene [25] and **(b:)** Graphene

- It is possible to separate the magnetic field of each mode into orthogonal components of which only one is relevant. The modes are hence Linearly Polarized.

  Note: Due to the particular rotational symmetry of the crystal the stationary modes in the IBZ corners has to be 6 fold degenerate. A particular x, y basis has to be chosen among the 6 possible axis rotations $\phi = k\pi/3$ in order to observe the linear polarization of Fig.3.8

3.4 Achieving Bianisotropy

In this section a z-symmetry breaking perturbation will be used to introduce bianisotropy to the developed Photonic Crystals. The role of bianisotropy in removing the degeneracy of the double Dirac Point in Fig. 3.6b thus opening a band gap will be formally explained using perturbation theory.

3.4.1 Perturbation theory for EM modes

It is known from section 2 that the EM field in a cavity can be described by the master equation for TE or TM modes that represents an eigenvalue problem with a number M of solutions, being the eigenfrequency ω_m the m-th eigenvalue and $(E_{z,m}, H_{z,m})$ the m-th eigenmode ($E_{z,m}$ for TM modes and $H_{z,m}$ for TE).

Let's now consider, without assuming any transverse modes decomposition, a cavity supporting a set of N eigenfrequencies $\{\omega_n\}_{n=1:N}$
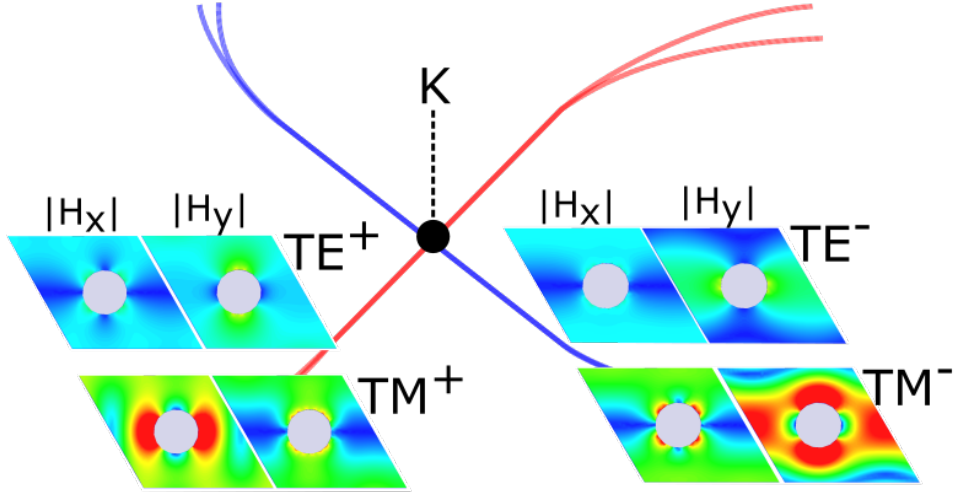
Fig. 3.8: First two low order TE and TM modes. *Left inset* Forward propagating (Fw) modes (red curve). *Right inset* Backward propagating (Bw) modes (blue curve).

that corresponds to an equal number of N eigenmodes $\{\mathbf{E}_n, \mathbf{H}_n\}_{n=1:N}$. If a very small perturbation of the cavity walls is considered, such that a volume ΔV, much smaller then the whole cavity volume V_0, is perturbed, then the perturbation theory yields a new set of N eigenfrequencies $\{\tilde{\omega}_m\}_{m=1:N}$ with eigenmodes $\{\tilde{\mathbf{E}}_m, \tilde{\mathbf{H}}_m\}_{m=1:N}$, related to the original set by (3.10) that relates the normalized frequency shift to the overlap integral between the perturbed and unperturbed eigenmodes.

$$\frac{\tilde{\omega}_m - \omega_n}{\omega_n} = -\frac{\int_{\Delta V}(\epsilon \mathbf{E}_n^* \cdot \tilde{\mathbf{E}}_m - \mu \mathbf{H}_n^* \cdot \tilde{\mathbf{H}}_m)dV}{\int_V(\epsilon \mathbf{E}_n^* \cdot \tilde{\mathbf{E}}_m + \mu \mathbf{H}_n^* \cdot \tilde{\mathbf{H}}_m)dV} \qquad (3.10)$$

Being the normal modes of a cavity a complete orthogonal set for the space of all electromagnetic modes then it is possible to express the perturbed cavity modes $\{\tilde{\mathbf{E}}_m \tilde{\mathbf{H}}_m\}$ in terms of the unperturbed ones using (3.11)

$$\begin{cases} \tilde{\mathbf{E}}_m &= \sum_k a_{k,m} \mathbf{E}_k \\ \tilde{\mathbf{H}}_m &= \sum_k a_{k,m} \mathbf{H}_k \end{cases} \qquad (3.11)$$

Where the index k spans the entire set of N eigenmodes while $a_{k,m}$ represent the coupling coefficient of the *m-th* perturbed eigenmode with the *k-th* unperturbed eigenmode.
By substituting (3.11) inside (3.10) and removing the m index for sake

of simplicity the following expression is derived, for every $\tilde{\omega} = \tilde{\omega}_m$:

$$\frac{\tilde{\omega} - \omega_n}{\omega_n} = -\frac{\int_{\Delta V} (\epsilon \mathbf{E}_n^* \cdot \sum_k a_k \mathbf{E}_k - \mu \mathbf{H}_n^* \cdot \sum_k a_k \mathbf{H}_k) \, \mathrm{d}V}{\int_V (\epsilon \mathbf{E}_n^* \cdot \sum_k a_k \mathbf{E}_k + \mu \mathbf{H}_n^* \cdot \sum_k a_k \mathbf{H}_k) \, \mathrm{d}V} \qquad (3.12)$$

by changing the order of integrals and sums and rearranging terms the latter becomes:

$$(\tilde{\omega} - \omega_n) \sum_k a_k \int_V (\epsilon \mathbf{E}_n^* \cdot \mathbf{E}_k + \mu \mathbf{H}_n^* \cdot \mathbf{H}_k) \, \mathrm{d}V =$$

$$-\omega_n \sum_k a_k \int_{\Delta V} (\epsilon \mathbf{E}_n^* \cdot \mathbf{E}_k - \mu \mathbf{H}_n^* \cdot \mathbf{H}_k) \, \mathrm{d}V \qquad (3.13)$$

In order to simplify (3.13) the following shorthands can be made, recalling the orthogonality condition of the eigenmodes, when integration on the whole space is considered, and imposing normalization on the arbitrary amplitudes of the orthonormal modes:

$$\int_V (\epsilon \mathbf{E}_n^* \cdot \mathbf{E}_k + \mu \mathbf{H}_n^* \cdot \mathbf{H}_k) \, \mathrm{d}V = \delta_{n,k}$$

$$-\int_{\Delta V} (\epsilon \mathbf{E}_n^* \cdot \mathbf{E}_k - \mu \mathbf{H}_n^* \cdot \mathbf{H}_k) \, \mathrm{d}V = \Delta_{n,k} = \Delta_{k,n}^* \qquad (3.14)$$

Where $\delta_{n,k}$ is the Kronecker delta. Using (3.14), The set of N equations of the form (3.13) can finally be recast into the eigenvalue problem expressed by (3.15):

$$(\tilde{\omega} - \omega_n)a_n = \omega_n \sum_k a_k \Delta_{n,k}$$

$$\Downarrow$$

$$\tilde{\omega}a_n = a_n\omega_n + \sum_k a_k \Delta_{n,k}\omega_n$$

$$\Downarrow$$

$$\tilde{\omega}a_n = \omega_n \sum_k a_k(\Delta_{n,k} + \delta_{n,k})$$

$$\Downarrow$$

$$\Omega \mathbf{a} = \tilde{\omega}\mathbf{a} \qquad\qquad\qquad (3.15)$$

where,

$$\mathbf{a} = (a_1, a_2 \cdots a_N)$$

$$\Omega = \begin{pmatrix} \omega_1(1 + \Delta_{11}) & \omega_1\Delta_{21} & \cdots & \omega_1\Delta_{N1} \\ \omega_2\Delta_{12} & \omega_2(1 + \Delta_{22}) & \cdots & \omega_2\Delta_{N2} \\ \vdots & \vdots & \ddots & \vdots \\ \omega_N\Delta_{1N} & \omega_N\Delta_{2N} & \cdots & \omega_N(1 + \Delta_{NN}) \end{pmatrix}$$

If, for instance, $\Delta_{n,k} = 0 \quad \forall n, k$ which correspond to a null perturbation, the Ω matrix becomes diagonal with the unperturbed eigenfrequencies on the main diagonal. Then from (3.15) we get $\{\tilde{\omega}_m\}_{m=1:N} = \{\omega_n\}_{n=1:N}$ and the corresponding eigenvectors are given by $\mathbf{a}_m$ with components $a_{k,m} = \delta_{k,m}$ (where index m has been restored from (3.11)). This trivial conditions corresponds to a null cross coupling between eigenmodes (i.e. the band structure remains obviously unaltered and the perturbed eigenmodes are equal to the unperturbed ones).

To understand the effect of non-null $\Delta_{n,k}$ it is possible to consider as an example the analytically treatable case of a cavity supporting $N = 2$ degenerate eigenfrequencies, for which (3.15) becomes

$$\begin{pmatrix} \omega_1(1 + \Delta_{11}) & \omega_1\Delta_{21} \\ \omega_2\Delta_{12} & \omega_2(1 + \Delta_{22}) \end{pmatrix} \begin{pmatrix} a_1 \\ a_2 \end{pmatrix} = \tilde{\omega} \begin{pmatrix} a_1 \\ a_2 \end{pmatrix} \qquad (3.16)$$

With $\omega_1 = \omega_2 = \omega$ for the imposed degeneracy condition. The perturbed cavity eigenvalues $\tilde{\omega}_{1,2}$ are given by the solution of the secular equation (3.17), where $\alpha = (1 + \Delta_{11})$ and $\beta = (1 + \Delta_{22})$

$$\begin{vmatrix} \omega_1\alpha - \tilde{\omega} & \omega_1\Delta_{21} \\ \omega_2\Delta_{21}^* & \omega_2\beta - \tilde{\omega} \end{vmatrix} = 0 \qquad (3.17)$$

$$\Downarrow$$

$$\tilde{\omega}^2 - \tilde{\omega}(\omega_1\alpha + \omega_2\beta) + \omega_1\omega_2(\alpha\beta - |\Delta_{12}|^2) = 0$$

Taking into account degeneracy between ω_1 and ω_2 the analytical solutions of (3.17) are given by (3.18)

$$\tilde{\omega}_{1,2} = \omega\frac{\alpha + \beta}{2} \pm \sqrt{\frac{\omega^2(\alpha + \beta)^2}{4} - \omega^2(\alpha\beta - |\Delta_{12}|^2)} \qquad (3.18)$$

$$\Downarrow$$

$$\pm \omega\sqrt{\frac{(\alpha - \beta)^2}{4} + |\Delta_{12}|^2}$$

The first term in the square root becomes then negligible and the two solutions of (3.18) are:

$$\begin{aligned} \tilde{\omega}_1 &= \omega(\alpha + |\Delta 12|) = \omega(1 + \Delta + \Delta_{12}) \\ \tilde{\omega}_2 &= \omega(\alpha - |\Delta 12|) = \omega(1 + \Delta - \Delta_{12}) \end{aligned} \qquad (3.19)$$

Let's assume $\alpha \approx \beta$ (i.e. $\Delta_{11} \approx \Delta_{22} = \Delta$).

Note: Since Δ_{kk} coefficients strongly depends on the perturbation itself it is not possible to generally assume $\delta\tilde{\omega} = \omega_1(1 + \Delta_{11}) - \omega_2(1 + \Delta_{22}) = 0$. The effect of $\delta\tilde{\omega} \neq 0$ however is the opening of gap that has nothing to do with the cross-polarization term Δ_{12}, and we recall here that topologically trivial behaviour is ensured only if the gap is induced by cross-polarization. The problem in the real structure has been studied by T.Ma [23] and will be only briefly reviewed in the next section. For the scope of this intuitive description it is however sufficient to assume $\delta\tilde{\omega} = 0$, that is a condition always obtainable for a particular perturbation.

If the cross coupling term $\Delta_{12} = 0$ then the eigenfrequencies are equally shifted by the α term and degeneracy, if present, is not removed. This correspond to the trivial case, for instance, of varying the cavity overall size while preserving all the unit cell symmetries. In this case orthogonal modes of the same polarization(TE or TM) cannot couple because of the orthogonality condition. Moreover modes belonging to different polarizations do not couple each other because TE TM decomposition holds true thus from (3.15) degeneracy is preserved (Fig. 3.6a). On the contrary if somehow $|\Delta_{12}| \neq 0$ degeneracy is lifted by the cross coupling term. A band gap of $\Delta\omega = 2|\Delta_{12}|$ is generated by the band splitting.

3.4.2   Applied perturbation theory

(3.15) represents an eigenvalue problem that describes how the eigenfrequencies of a cavity mode change when a small perturbation acts on the cavity modes by coupling them each other. The main result obtained in the last sections are that the perturbation may open a band-gap if the coupling between different modes is strong enough. Here we show how a z-symmetry breaking perturbation is able to couple TE and TM modes.

The PhC in Fig. 3.1 supports two couples of TE/TM modes that can be made four fold degenerate, each couple of equally polarized modes, as it can be seen from Fig. 3.6b is made by a Fw mode (positive group velocity) and a Bw mode (negative group velocity). Let's call $\omega_e^- = \omega_e^+ = \omega_m^- = \omega_m^+ = \omega$ the 4 degenerate eigenfrequencies with eigenmodes $\{\mathbf{E}_n, \mathbf{H}_n\}_{n=1:4}$. Here the subscripts $+/-$ indicates the direction of propagation of the mode while superscripts e/m stand for TE/TM. The above developed perturbation theory (3.15) yields the following eigenvalue problem for the cavity with broken z-symmetry:

$$\Omega \boldsymbol{a} = \tilde{\omega} \boldsymbol{a} \qquad\qquad (3.20)$$

Where,

$$\boldsymbol{a} = (a_e^-, a_e^+, a_m^-, a_m^+)$$

$$\Omega = \omega \begin{pmatrix} (1 + \Delta_{ee}^{--}) & \Delta_{ee}^{+-} & \Delta_{me}^{--} & \Delta_{me}^{+-} \\ \Delta_{ee}^{-+} & (1 + \Delta_{ee}^{++}) & \Delta_{me}^{-+} & \Delta_{me}^{++} \\ \Delta_{em}^{--} & \Delta_{em}^{+-} & (1 + \Delta_{mm}^{--}) & \Delta_{mm}^{+-} \\ \Delta_{em}^{--} & \Delta_{em}^{++} & \Delta_{mm}^{-+} & (1 + \Delta_{mm}^{++}) \end{pmatrix}$$

The matrix Ω can be simplified employing the orthogonality condition and the field profiles in Fig. 3.8.

- If the in-plane symmetries of the unperturbed crystal are not changed the overlap integral of different modes of the same polarization is null because of the orthogonality, hence all terms $\Delta_{ee}^{+-} = \Delta_{mm}^{+-} = 0$.

- TE and TM modes propagating in the same direction presents orthogonal dipoles, hence all the terms $\Delta_{em}^{--} = \Delta_{em}^{++} = 0$.

- If, again, the perturbation possess cylindrical symmetry then all TE and TM modes are equally perturbed and it is possible to
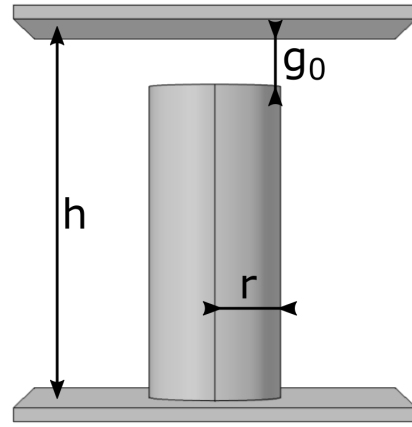
assume $\Delta_{ee}^{++} = \Delta_{ee}^{--} = \Delta_{ee}$ and $\Delta_{mm}^{++} = \Delta_{mm}^{--} = \Delta_{mm}$, this assumption is numerically demonstrated by T.Ma [23]:

From the above simplifications (3.20) becomes the following eigenvalue problem:

$$
\begin{pmatrix}
(1+\Delta_{ee}) & 0 & 0 & \Delta_{me}^{+-} \\
0 & (1+\Delta_{ee}) & \Delta_{me}^{-+} & 0 \\
0 & \Delta_{me}^{-+*} & (1+\Delta_{mm}) & 0 \\
\Delta_{me}^{+-*} & 0 & 0 & (1+\Delta_{mm})
\end{pmatrix} \boldsymbol{a} = \tilde{\omega}\boldsymbol{a} \quad (3.21)
$$
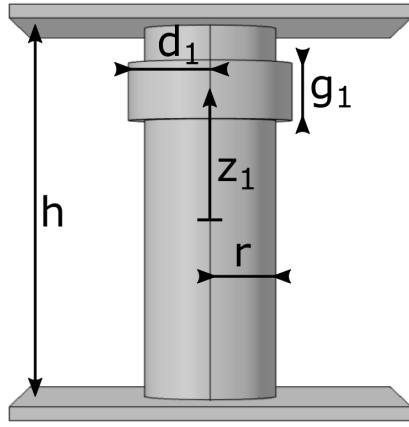
(a) *Asymmetric Metal washer*   **(b)** *Air gap between the rod and only one of the mass planes*

Fig. 3.9

Examples of perturbations that break z-symmetry are depicted in Fig. 3.9.
Considering the structure in 3.9a and assuming $(d_1/r) \approx 1$ an analytical treatment can be done by using (3.9) into (3.14) in order to obtain an approximate expression for Δ_{em}:

$$
\begin{aligned}
\Delta_{em} &= -\int_{\Delta V} \left(\epsilon \mathbf{E}_e^* \cdot \mathbf{E}_m - \mu \mathbf{H}_e^* \cdot \mathbf{H}_m\right) \mathrm{d}V \\
&= \int_{\Delta V} \mu (\mathbf{H}_e^* \cdot \mathbf{H}_m)\, \mathrm{d}V \\
&= \int_{\Delta V} \sin\!\left(\frac{\pi}{h}z\right)\mu\left(H_{e,x}^* H_{m,x} + H_{e,y}^* H_{m,y}\right) \mathrm{d}V \\
&= -\frac{h}{\pi}\cos\!\left(\frac{\pi}{h}\right)\Bigg|_{z_1-h_1/2}^{z_1+h_1/2} \int_{\Delta A} \mu\left(H_{e,x}^* H_{m,x} + H_{e,y}^* H_{m,y}\right) \mathrm{d}A \\
&= \frac{2h}{\pi}\sin\!\left(\frac{h_1\pi}{2h}\right)\sin\!\left(\frac{\pi}{h}z_1\right)\mathcal{S}_{em} \tag{3.22}
\end{aligned}
$$

It is important to note that $z_1 \to -z_1 \quad \Rightarrow \Delta_{em} \to -\Delta_{em}$ so that relocating of the perturbation in $-z$ reverses the sign of bianisotropy. This suggests the use of an interface between z-symmetry reversed BPhC to realize the TPMW.

3.5 From bianisotropy to Topologically Insulating state

Equation (3.21) describes the frequency shift of the band diagram due to a perturbation that acts on the z-inversion symmetry of the PhC. From (3.21) it is evident that the perturbation poorly contributes to intra-polarization coupling (i.e. coupling of the two TE and TM modes is weak) while providing strong cross-polarization coupling.

An effective low-energy Hamiltonian for the photonic states in the vicinity of the K point ($\mathbf{k} = K + \delta k$) can be constructed from (3.21) and taking into account the group velocities v_d (considered equal for both polarizations), having defined $\alpha = (a + \Delta_{ee})$, $\beta = (1 + \Delta_{mm})$:

$$
\mathcal{H}_k = \omega \begin{pmatrix} \alpha - v_d|\delta k| & 0 & 0 & \Delta_{me}^{+-} \\ 0 & \alpha + v_d|\delta k| & \Delta_{me}^{-+} & 0 \\ 0 & \Delta_{me}^{-+*} & \beta - v_d|\delta k| & 0 \\ \Delta_{me}^{+-*} & 0 & 0 & \beta + v_d|\delta k| \end{pmatrix} \tag{3.23}
$$

Here perfect degeneracy between TE and TM bands has been assumed ($\omega_e = \omega_m = \omega$). As it has been previously stated, $\delta\tilde{\omega} = \omega_e(1 + \Delta_{ee}) - \omega_m(1 + \Delta_{mm}) = 0$ is, accordingly to this theory a necessary condition to obtain a gap induced only by δ_{em}. Since $\Delta_{ee} = \Delta_{mm}$ is not generally obtainable T.Ma shows that is possible to design the unperturbed PhC

such that $\omega_m = \dfrac{1 + \Delta_{ee}}{1 + \Delta_{mm}}\omega_e$. Although this condition ensures $\delta\tilde{\omega} = 0$ for a finite set of perturbations $\{\Delta V\}_k$ it turns out that as long as the contribution of $\delta\tilde{\omega}$ remains small with respect to Δ_{em} the bianisotropic gap is not affected, as it is confirmed by the numerical simulations of Fig. 3.10b.

This result is in accordance with the treatment that Kane and Mele [16] provide about the robustness of QSH effect in graphene where the effects of Rashba coupling (weaker then SOI) are discussed. In both cases the band gap can be introduced either by SOI (or cross polarization coupling for the BPhC) either by parasitic effects breaking parity invariance. As it has been already stated in 2.3.2, however, the gaps induced by SOI and parasitic effects are not topologically equivalent and the correspondence can be understood by looking at (3.18) that is formally equivalent to the graphene bandgap with SOI and Rashba interaction [16]. The gap opened by $\delta\tilde{\omega}$ and by Δem are of inverted sign, and cannot both simultaneously exist. If a topologically non trivial gap is present due to the Δem term, in order to obtain a topologically trivial behavior it is necessary to annihilate the gap with the $\delta\tilde{\omega}$ term, and then reopen it causing a topological phase transition. It is the relative strength between the two phenomena that decides the topological phase of the system.

In case $\Delta_{em} \neq 0$ (3.23) is not diagonal and the unperturbed basis of TE/TM modes are no longer eigenmodes of the Hamiltonian. This means that some dressed states has to be considered that represents the true eigenstates. A proper transformation matrix T leads to the block-diagonal Hamiltonian

$$\mathcal{H}_k = \omega \begin{pmatrix} \omega(1 + \Delta_{em}) & v_d(\delta k_x - j\delta k_y) & 0 & 0 \\ v_d(\delta k_x + j\delta k_y) & \omega(1 - \Delta_{em}) & 0 & 0 \\ 0 & 0 & \omega(1 + \Delta_{em}) & v_d(\delta k_x - j\delta k_y) \\ 0 & 0 & v_d(\delta k_x + j\delta k_y) & \omega(1 - \Delta_{em}) \end{pmatrix} \quad (3.24)$$

With the new basis set $\Psi^{\uparrow} \cong \left[\psi_R^{\uparrow}, \psi_L^{\uparrow}\right]$ and $\Psi^{\downarrow} \cong \left[\psi_R^{\downarrow}, \psi_L^{\downarrow}\right]$ given by:

$$\begin{aligned} \Psi_R^{\uparrow} &= a_e^- - ja_e^+ + a_m^- - ja_m^+ \\ \Psi_L^{\uparrow} &= a_e^- + ja_e^+ + a_m^- + ja_m^+ \\ \Psi_R^{\downarrow} &= a_e^- - ja_e^+ - a_m^- + ja_m^+ \\ \Psi_L^{\downarrow} &= a_e^- + ja_e^+ - a_m^- - ja_m^+ \end{aligned} \qquad (3.25)$$

The new basis set describes 4 circularly polarized states with TE/TM hybridization. The *spin* degree of freedom is given by the sign of the

TE/TM combination (i.e. $\Psi^\uparrow \widehat{=} TE + TM \quad \Psi^\downarrow \widehat{=} TE - TM$) while the *orbital* degree of freedom is given by the handedness (i.e. relative phase between TE(TM) modes). $(\Psi^\uparrow, \Psi^\downarrow)$ is thus a "Photonic Spinor" that represents the true eigenstates of the hamiltonian (3.24). The upper left block of (3.24) relates to the $\Psi^\uparrow$ pair of modes while the bottom right block refers to $\Psi^\downarrow$. The two pairs are completely decoupled hence no power transfer is possible between $\Psi^\uparrow$ and $\Psi^\downarrow$ moreover the coupling term Δ_{em} lifts the degeneracy by raising the frequency of the $(\psi_R^\uparrow \psi_L^\downarrow)$ pair and lowering the frequency of the $(\psi_L^\uparrow, \psi_R^\downarrow)$ thus opening a Photonic Band Gap (PBG).

If an analogue construction is made for the effective hamiltonian at the K' point (that can be derived with space-inversion) and the two are combined in an 8x8 effective hamiltonian then $\mathcal{H}_{eff}$ can be written in the exact form of (2.9), with the term Δ_{SO} replaced by Δ_{em}. This means that *pseudo-spin* states $\Psi^\uparrow \Psi^\downarrow$ are equivalent to the electronic spin states in QSH Topological Insulators (TI). As Kane-Mele demonstrated electronic states in QSH insulators possess non trivial topological order, it follows that the bandedges of the PBG arising in the perturbed BPhC are Topologicaly non trivial. Specifically it is possible to demonstrate [23, 25]

$$\begin{aligned} \mathcal{C}^\uparrow &= sgn(\Delta_{em}) \\ \mathcal{C}^\downarrow &= -sgn(\Delta_{em}) \end{aligned} \qquad (3.26)$$

Where $\mathcal{C}$ is the *Chern number*, the topological invariant whose finiteness characterizes topological insulators (here we refer to section 2.3). Since time-reversal invariance holds true (no external magnetic field is present to break time-reversal) the net Chern number of the BPhC remains null ($\mathcal{C} = \mathcal{C}^\uparrow + \mathcal{C}^\downarrow = 0$). However the two spin modes can be considered as totally uncoupled because of the block diagonal form of $\mathcal{H}_{eff}$ from (3.24). It is then possible to define a *spin Chern number* [29] $\mathcal{C}_s$ such that for the BPhC it is obtained $\mathcal{C}_s = 1/2|\mathcal{C}^\uparrow - \mathcal{C}^\downarrow| = 1$. Photonic analogue of spin-polarized TPSS are expected to arise at the edge of the BPhC as a consequence of the past discussion.

3.5.1   A more practical perturbation

Although the results formally obtained in the previous sections refers to the perturbed structure of Fig. 3.9a they can be extended to a more practical perturbation such that of Fig. 3.9b. The calculated PBS corresponding to such perturbation is depicted in Fig. 3.10a where the opening of a complete PBG is confirmed trough numerical eigenmodes analysis. The latter perturbation will be the one used in all practical designs that will follow.

(a) *PBS of the BPhC perturbed as Fig. 3.9b*

**(b)** *eigenfrequencies at K point for varying air gap g_0*
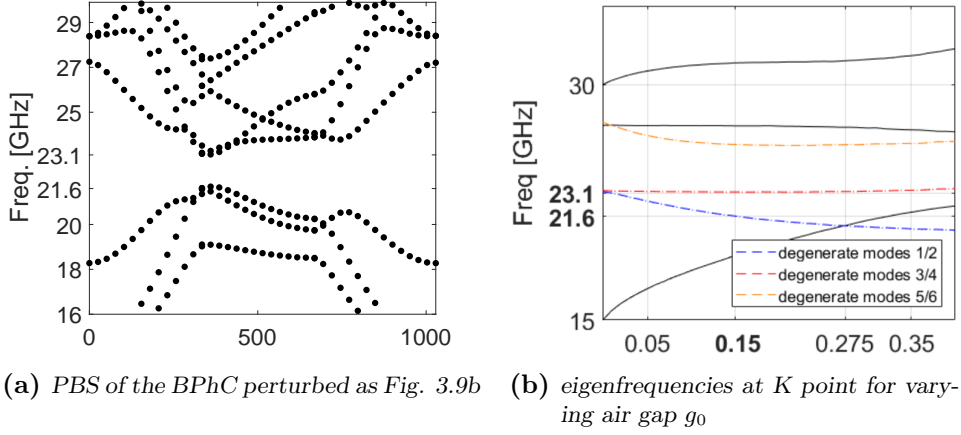
Fig. 3.10: PhC parameters: same as Fig. 3.6b. For 3.10a only: $g_0 = 0.15a_0$

As it has been previously discussed the detuning of g_0 from its nominal value might cause the opening of a topologically trivial band-gap by rendering $\delta\tilde{\omega} \neq 0$. From the analytical treatment of the previous section however it turns out that the size of the cross-polarization coupling perturbation g_0 strongly influences the entity of the Δ_{em} term while only marginally contributes to the detuning of degenerate eigenfrequencies. As long as $\delta\tilde{\omega} \approx 0$ the topological phase of the perturbed eigenmodes, only depending from the sign of Δ_{em}, does not change. Non trivial topological behavior is thus expected for a wide range of g_0 values. The smooth change in the band structure for varying g_0, which suggests absence of topological phase transition, is depicted in Fig. 3.10b where the PBS at point K(K') is plotted vs. the size of the air gap g_0. It is possible to see that the gap keeps on increasing for increasing values of g_0 until for $\tilde{g}_0 = 0.275a_0$ lower modes enter inside the gap and topological protection is lost. Actually a closer look on the whole PBS rather than the sole K point shows that the maximum attainable gap size is smaller since lower modes enter already in the gap for $\tilde{g}_0 \approx 1.9$ and $\mathbf{k}a_0 \in [\Gamma, K]$(Fig. 3.11). The robustness of the bulk properties with respect to defects on g_0 is one of the manifestations of the topological properties of the BPhC and the possibility to obtain various gap sizes can be exploited to design devices with different fractional bandwidths [1].

---

[1] Actually following the analytical model developed in 3.5 a finite $\delta om\tilde{e}ga$ causes in any case the pure spinor to be no more eigenstates of the hamiltonian. Topological protection holds in the sense that propagation is still insensitive to defects, but a very weak coupling between $\Psi^{\uparrow}$ and $\Psi^{\downarrow}$ continuously occurs.
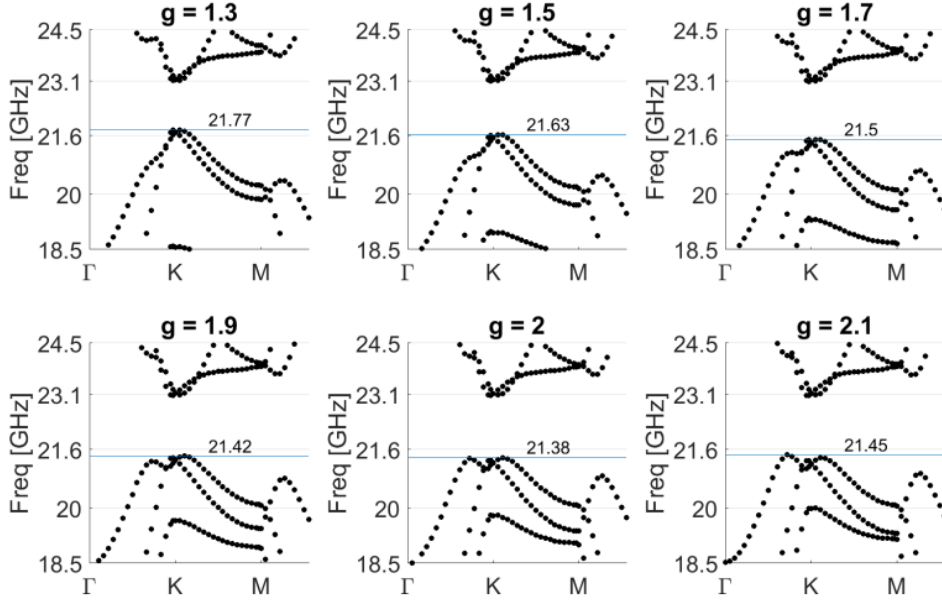
Fig. 3.11: Photonic Band Structure of the BPhC for various values of g_0/a_0. For $\tilde{g}_0/a_0 \approx 1.9$ a lower mode enters inside the gap between Γ and $K(K')$ points of the diagram.

3.6 Topologically Protected MetaWaveguide

Conventional waveguides guide light by confining it with metallic mirrors. Meta-Waveguide (MW) can be obtained with line defects in PhC exhibiting a bulk PBG, in such cases light is confined by the absence of propagating states in the bulk PhC but no metallic walls are used since PBG can be engineered in all-dielectric PhC. Even if performances of MW are superior then that of conventional waveguides (with the drawback of tremendously higher costs both in economic terms and for the footprint) the two classes are equivalent in the sense that both uses *topologically trivial* mirrors to confine light [22].

In Fig. 3.12 a comparison between topologically trivial and topologically non trivial modes is illustrated. Defective states (i.e. topologically trivial states in PhC) are independent from the bulk bands and can be localized within the bulk band gap by acting on defect parameters. This means that they can also be removed from the band gap by continuously changing a single parameter. This is what happens, for instance, by continuously changing the width d of a Wd MW: The defective modes are removed from the band gap and wave guiding is lost. Moreover, since defective states are not bonded to the band edges there must exist states with both positive and negative group velocity
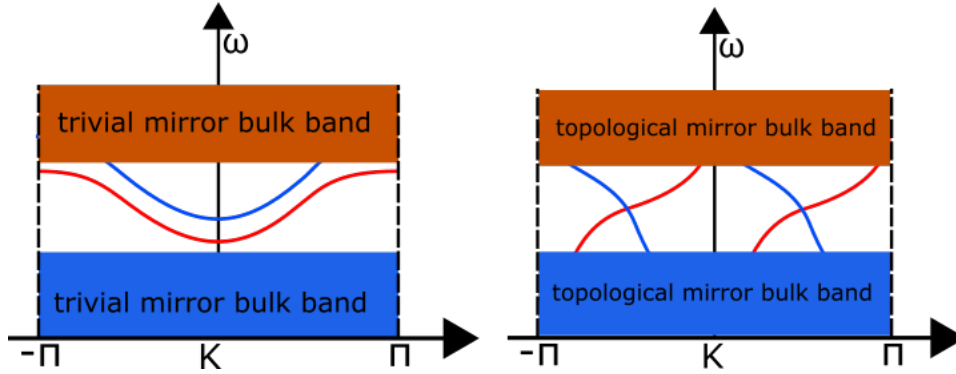
Fig. 3.12: *Left:* defective modes localized within topologically trivial mirrors. *Right:* Topologically Protected Surface States localized within topologically in-equivalent mirrors.

(although the phase velocity might be the same because K reverses sign), this allows Fw light to scatter at imperfections and couple to a Bw mode. TPSS conversely are inherently bonded to the bulk crystal band edges. They must continuously exist within bulk bands of different topologies (i.e. Chern numbers). Since they are bonded to both the band edges, TPSS have a well defined group velocity and thus are unidirectional. In general light cannot back-scatter at imperfections by coupling to a Bw mode since it does not necessarily exist (or because coupling is prohibited as in the described platform).
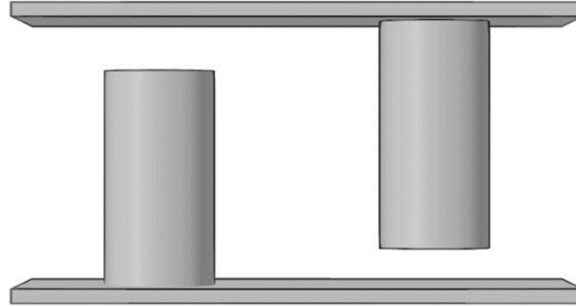
Fig. 3.13: Interface between two BPhC with reversed sign of Δ_{em}

The existence of topologically protected states at the edge of a TI is guaranteed by an important result in topological quantum matter known as the *bulk edge correspondence* [8]. Since air is an ordinary insulator for electrons, the edge of a TI is a topologically non trivial domain wall for electronic systems. On the contrary EH waves propagates in air thus the edge of a PTI cannot in general be used alone for
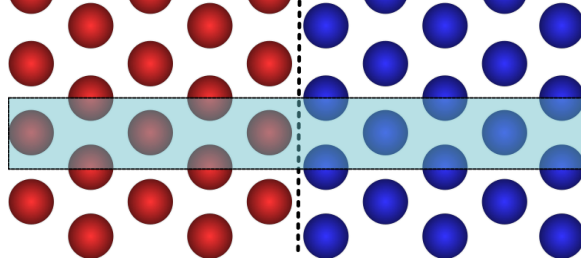
Fig. 3.14: Representation of a super-cell (shaded area). Blue and red circles represents rods with the air gap in opposite positions.

guiding light trough TPSS.

Fortunately a couple of BPhC with reversed sign of bianisotropy possesses the same PBS (thus clearly the same band gap) but are topologically inequivalent since the Chern numbers reverses their sign. An interface as the one in Fig. 3.13 Can hence be used to guide EM radiation, and is expected to support two couples of TPSS, one for each spin state. The number N of protected edge modes arising at the interface of a TI for each spin state is given by the bulk-edge correspondence, which can be expressed as [13]

$$N = \Delta\mathcal{C}_{gap} \tag{3.27}$$

Where N is the signed number of protected edge modes (the sign indicates the direction of propagation) and $\mathcal{C}_{gap}$ is the *gap Chern number*, that is the sum of all the Chern numbers of the bands that lies under the gap. $\Delta\mathcal{C}_{gap}$ is thus the difference between the gap Chern numbers of the two media confining the edge mode.

Since it has been shown that the spin states can be considered separately and the system is well described for each spin state by the *spin-Chern number* we can look for the number of guided modes for each spin $N^{\uparrow(\downarrow)}$

$$N^{\uparrow(\downarrow)} = \Delta\mathcal{C}_{gap}^{\uparrow(\downarrow)} \tag{3.28}$$

Since Δ_{em} changes sign in the two BPhC with reversed symmetry then also $\mathcal{C}^{\uparrow(\downarrow)}$ changes sign, and $\Delta\mathcal{C}_{gap}^{\uparrow} = -\Delta\mathcal{C}_{gap}^{\downarrow} = \pm 2$, where the $\pm$ sign changes accordingly to the spin state. We expect then two Fw edge modes for the spin-up polarization and two Bw modes for the spin-down states. These results are confirmed via numerical calculations of the TPMW eigenmodes performed with the super-cell method schematized in Fig. 3.14. A unitary cell comprising a single reticular constant in the direction of propagation and a sufficiently high number of reticular constants per each side of the interface is constructed. Propagation is then inspected for the only allowed direction. Since this method
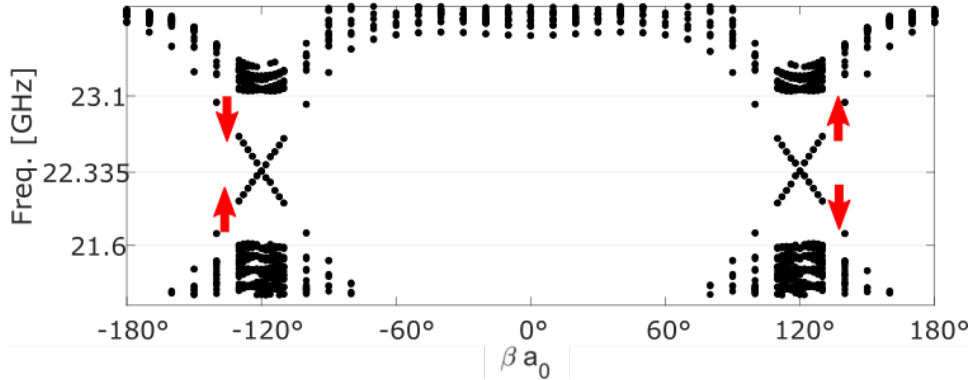
Fig. 3.15: full PBS of a super-cell. Arrows indicate the *spin state* of the TPSS

projects the allowed 2-dimensional bulk states in a single dimension a continuum of modes is expected for the frequencies outside the gap. Results are depicted in Fig. 3.15: Beneath the PBG a total of 4 modes are observed, two Fw propagating and two Bw propagating.

3.7   Topologically protected eigenmodes analysis

Stemming from the results of Fig. 3.15 and 3.16 several observations can be made on the edge modes.
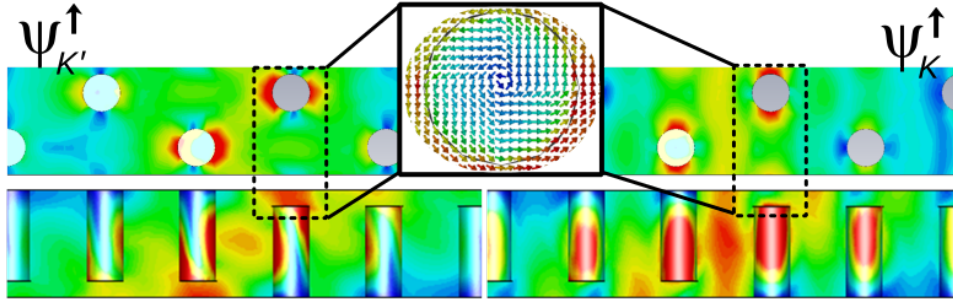
Fig. 3.16: longitudinal (top) and transverse (bottom) electric field profiles for the Spin up ($\Psi^\uparrow$) modes calculated at K' (left) and K (right) points (corresponding to $-120°$ and $120°$) of 3.15. The inset shows counter-clockwise rotation of the pointing vector for the spin-up pairs

- Since the TPSS modes arises only in the vicinity of the K(K') points the use of an effective Hamiltonian restricted to the K(K') points in place of the whole BZ is justified. Spin-degeneracy is in fact generally lost away from the relevant points of the BZ, as can

be seen from Fig. 3.6b, thus nothing could have been said about
edge states eventually arising elsewhere.

- TPSS covers the entire band-gap and has well-defined group ve-
  locities. As it is expected from the topological properties of the
  mirrors, guiding modes are present for all the frequencies of the
  bulk PBG.

- The pointing vector in the air gap region (shown in the inset of
  Fig. 3.16) rotates in the counter clockwise direction for spin up
  modes and in the clockwise direction for the spin-down modes.
  The physical meaning of the *pseudo-spin* states resides thus on
  the spinning of the pointing vector.

- Since time-reversal symmetry $\mathcal{T}$ is not broken the super-cell PBS
  is symmetric in the K-space. Time-reversal operation however
  acts as $(K \rightarrow -K \quad H \rightarrow -H)$ thus transforming spin-up states
  in spin-down states (sign of pointing vector $\mathbf{s}$ is inverted). Guided
  modes shown in Fig. 3.16 are thus related to their degenerate
  Kramer partners by $\mathcal{T}$ that transforms $\Psi_K^\uparrow \rightarrow \Psi_{K'}^\downarrow \quad \Psi_{K'}^\uparrow \rightarrow \Psi_K^\downarrow$.
  Field profiles of $\Psi_{K(K')}^\downarrow$ are thus the same as in Fig. 3.16 but with
  reversed K and K'.

The above mentioned observations suggest that it should be possi-
ble to selectively excite only Fw (or Bw) propagating modes by using
appropriately shifted circularly polarized dipoles. Once the proper $\Psi^\uparrow$
(or $\Psi^\downarrow$) couple of modes have been excited spin-flipping is forbidden by
the block diagonal form of the Hamiltonian in (3.24). Back reflection
is thus prohibited by *spin conservation* and TPSS states are expected
to be insensitive of spin-preserving defects along the propagation path.

Excitation of TPSS and their Topologically Protected behavior is
addressed in the next chapter along with the design of a Directional
Coupler based on TPMW with properties inherited by the Topological
Protection of the guided modes.

CHAPTER 4

Devices

In the previous chapter the physical and mathematical foundations of the proposed Topologically Protected Meta Waveguide (TPMW) have been shown. It has been demonstrated how a topologically non trivial Photonic Band Gap (PBG) can be opened in a planar Photonic Crystals (PhC) ad how such a PBGTopologically Protected Surface States (TPSS) supported by an interface between two different Bianisotropic Photonic Crystal (BPhC) have been showed in Fig. 3.16.

In this chapter the problem of coupling EM power into the guided modes is initially addressed, then topologically protected transport will be numerically demonstrated as perfect transmission throughout a 120° bent structure will be observed. The numerical realization of a directional coupler based on the proposed TPMW will finally be shown and a discussion on the resulting behavior will be made.

4.1 Notes on computational methods

Full-Wave (F-W) simulations are intensive tasks to be performed without powerful parallel computation devices and several days may be required to compute the response of an electrically big structure. The simulation time strongly depends on the proper choice of the mesh, which is the step size and method for domain discretization. Although CST MWS $^{\text{TM}}$ is one of the fastest simulators for time-domain computation a trade-off on the mesh size has been necessary in order for the simulations to be handled by average Personal Computers: the standard setting for the mesh step is around 12-15 mesh cells per wavelength, with an hexahedral mesh, which is the only one allowed by the time domain simulator. Although the metallic rods are not very accurately described with this step, simulations on smaller domains showed that results don't change much if a finer mesh is used. To enhance accuracy the *snapping* options is active, which snaps the mesh line to every edge on the computation domain.

Time domain simulations are carried out by calculating the pulse response of the structure. The input ports emit a time pulse with a total power of 1 W and the pulse propagation throughout the structure is computed. The cross-section of the pulse has normally Gaussian profile with a frequency content determined by user-defined upper and lower limits[1]. The stopping criteria are various:

- **simulation time:** The simulation is stopped after a fixed amount of time.

- **number of pulses** The simulation is stopped after a time equivalent to a fixed number of pulses.

- **propagation length** The simulation is stopped after a time equivalent to a fixed propagation length in free space (for the observed frequencies).

- **steady state energy** The simulation is stopped after the total field energy inside the structure has reached a certain attenuation with respect to the peak value.

  note: The energy criterion can be superimposed on the others, this means that if the total energy has decreased under, for instance, -40dB before the maximum simulation time the computation is successfully aborted because the total field has already been radiated.

---

[1]The frequency limits are often, but not necessarily, the bulk PBG edges
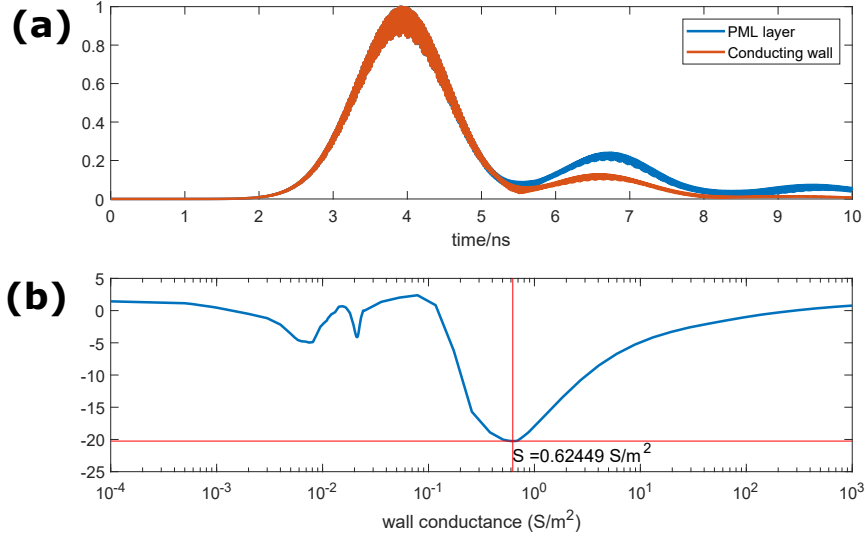
Fig. 4.1: **(a)**: Time traces of an electric field probe placed n=15 rods before a Perfectly Matched layer (blue) and an impedance wall (orange) **(b)** Attenuation of the reflected peak for varying conductance values for the impedance wall

One key issue in time domain simulations is represented by the boundary conditions, if a pulse is reflected by the outer boundary it will propagate again inside the structure. This will critically affect both simulation time and results because steady state energy will be more slowly achieved and the reflected field that remains into the domain will perturb the solution. The reflection from outer boundary can be inspected by looking at the time domain field profiles for a point field probe at a fixed distance from the boundary. As it can be seen from Fig. 4.1a the time trace shows a second peak following the first, that is the reflected pulse. The reflection from Perfectly Matched Layer (PML) boundary can be calculated as $R = 20\log_{10}(Pk_2) = -13dB$, where Pk_2 is the reflected field peak value. Better behavior is obtained with an *impedance wall* with the characteristic impedance of the mode for which a maximum attenuation of $20dB$ can be obtained. The calculation of the TPMW characteristic impedance is performed with a sweep on the value of Z_0 and minimization of the peak ratio in Fig. 4.1a. The maximum absorption is found for $Z_0 = 1.6\,\Omega\,\text{m}^{-1}$, as it is illustrated in Fig.4.1b. Moreover the frequency behavior doesn't seem to be perturbed for various values of Z_0, meaning that the characteristic impedance is fairly constant in frequency. Even the impedance layer however provides non completely negligible reflection. Better results

might be obtained with properly designed multi-layered terminations, however due to time constraints of the work this solution could not be investigated.

It is not obvious how to deal with the unwanted reflections. Where it is possible to neglect them the steady state energy is set to sufficiently high values and the results are assumed to be accurate up to the level of reflections (i.e. 20dB). Another method would be to extent the boundary walls and truncate the time signal of user-defined probes before the reflected signal arrives. This is in principle a good method, however it requires the shape of the pulse to be unaltered throughout the propagation which is very unlikely, moreover the calculation domain is increased with negative side effects on calculation time. The first approach is generally used.

As a side note the time traces in Fig.4.1 can be used to numerically calculate the group velocity of TPSS. Knowing that the probe is placed $n = 15$ rods before the boundary the reflected peak has to propagate for $2 \cdot 15 \cdot a_0 = 30\,\text{cm}$ before returning to the probe. The observed peak distance is $\approx 3\,\text{ns}$ which correspond to a group velocity of $v_g \approx 1 \cdot 10^8 \text{m}/\sec$. The corresponding group index is $n_g \approx 3$ which agrees with what can be more precisely calculated from Fig.3.15.

4.2 Mode Launchers

Although theoretically speaking no power transfer can happen between Forward propagating (Fw) spin-up ($\Psi^\uparrow$) and Backward propagating (Bw) spin-down ($\Psi^\downarrow$) modes, the TPMW is time-reversal invariant so it actually supports both Fw and Bw modes. In order to enable real-life devices it is then necessary to accurately design launching systems able to selectively excite the desired spin polarization minimizing the losses that occurs by power coupling to Bw modes.

4.2.1 Unidirectional modes excitation

electric dipoles

In their leading work T. Ma *et al.* [23] showed that a Circularly polarized (CP) electric dipole, placed in the middle of the air gap of one of the rods acts as an ideal launcher, able to excite pure spin states. Although the results presented in the work shows a perfect Fw coupling we couldn't retrieve, with our numerical simulations, a comparable cou-

pling efficiency. The non-ideality of the excitation with electric dipoles can be caused by various factors:

- The numerical simulator used (CST MWS ^{TM}) allows for the realization of rotating sources only as a superposition between two phased linear dipoles. This may cause a perturbation on the radiation field by one dipole due to the presence of the other, leading to a non ideal behavior.

- The actual position of the electric dipoles in the z-direction significantly varies the coupling efficiency

- The length of the electric dipoles significantly varies the coupling efficiency due to the different radiation pattern and mesh resolution.

More efficient ways of coupling EM power in a pure spin state can be investigated by looking at other sources producing similar field patterns.
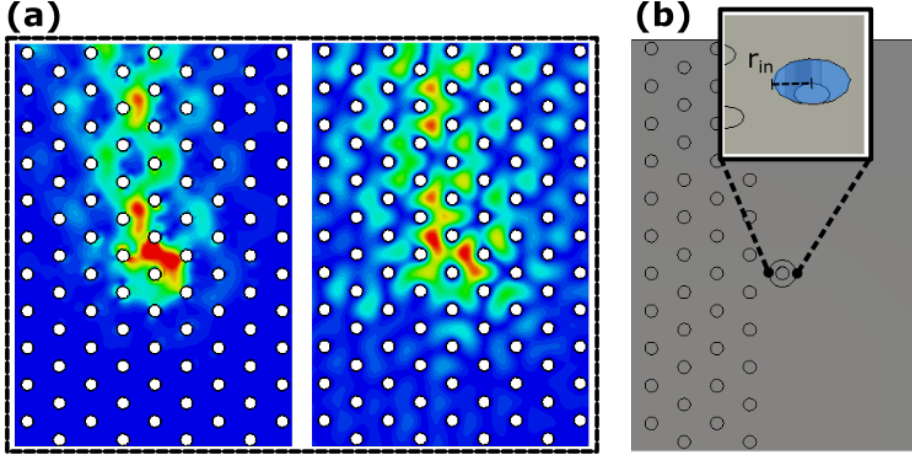
Plane wave

Recent works [34] illustrated the possibility to convert light angular momentum in linear momentum, by driving photons with opposite handedness in opposite directions. The silicon waveguide employed in ref. [34] is not chiral thus guided modes are obviously not "one way", nevertheless the resonating silicon micro-disk resolves the handedness of a normally impinging CP Plane way and excites a single mode waveguide with a reduction of 18dB on the unwanted direction.
Although many are the differences between the unchiral Silicon On Insulator platform that is subject the of ref. [34] and the spin-chiral metallic TPMW it is possible to recognize that the pointing vector pattern developing on the surface of the silicon disk is very similar to the one associated with a pure spin state on the TPMW. 3.16
We found indeed that a CP Plane wave coupled to the structure via a circular slot of appropriate radius cut in the top plate acts as a good launcher exhibiting a reduction on the $\Psi^{\downarrow}$ of as much as 13dB (Fig. 4.2).

Circular waveguide

The dominant modes of a circular waveguide are a couple of degenerate TE_{11} modes [3], polarized along two orthogonal directions of space (Fig. 4.3). A balanced superposition of these modes with a relative phase of $90°$ produces, around center of the waveguide, a field pattern similar

Fig. 4.2: **(a)**: Pointing vector Abs. Value (left) and E_z field profile (right).
(b): Top view of the Plane Wave launcher.
$r_{in}/r = 1.84$

to a rotating electric dipole.

The cutoff frequency of a circular waveguide with radius r_g is given by (4.1).

$$f_c = \frac{p_{mn} \cdot c}{2\pi r_g} \qquad (4.1)$$

Where p_{mn} is a tabulated parameter for every TE/TM mode [3] The lowest order TE_{11} modes have $p_{11}^e = 1.841$ while the first higher order mode is a TM_{01} with $p_{01}^m = 2.405$. The proper radius of the input waveguide r_g has to be chosen in order to have only the degenerate TE_{11} modes propagating inside the frequency range of the bulk PBG (*i.e.* $f \in [21.6, 23.1]$GHz). The upper and lower bound for the radius r are found by solving the following system:

$$\begin{cases} f_{TE_{11}} = \dfrac{1.841 \cdot c}{2\pi r_g} < 21.6\,\text{GHz} \\[4mm] f_{TM_{01}} = \dfrac{2.405 \cdot c}{2\pi r_g} > 23.1\,\text{GHz} \end{cases} \Rightarrow r_g/r \in [2.31, 2.88] \qquad (4.2)$$

If $r_g > r_{max}$ then the unwanted TM_{01} would propagate for some frequencies $f < 23.1\,\text{GHz}$ and if $r < r_{min}$ the TE_{11} modes would become evanescent for some frequencies $f > 21.6\,\text{GHz}$ resulting in an unwanted behavior of the launcher. Fairly good results in term of single spin coupling are obtained defining a circular waveguide directed on the -z direction and coupled to the structure via a circular hole on the top plate.(4.4)

In order to maximize the spin-up coupling without changing the input
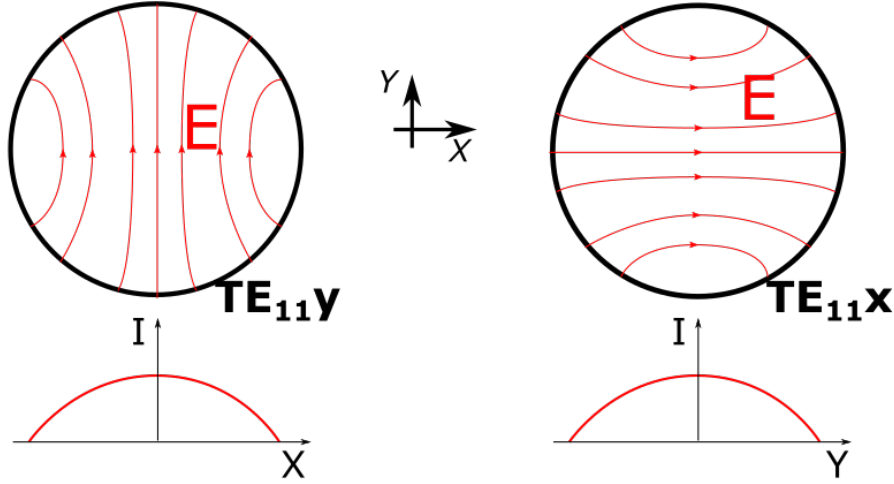
**Fig. 4.3:** Dominant TE_{11} orthogonal modes of a circular waveguide

waveguide radius it is convenient to define an *exit iris* that chokes the waveguide in correspondence with the top metal plate. This have as a side effect the excitement of a series of higher order modes in the waveguide (mode matching), but as long as the irradiating field pattern alone is considered the smaller the iris radius r_{iris} it is, the more similar the field pattern will be with respect to the previously treated case of CP Plane wave.

Parametric simulations on the iris aperture r_{iris} leaving the guide's radius unchanged $r_g/r = 2.80$ shows an attenuation on the $\Psi^{\downarrow}$ modes of 12dB on the whole interval $r_{\mathrm{iris}}/r_g \in [1.6, 2.8]$ with a maximum of 14dB at $r_{\mathrm{iris}}/r_g = 2.22$.

It is relevant to say that Circular Waveguide exciters should be used only if a proper mechanism is adopted to *match* the Circular WG modes to the structure, i.e. the port has to be adapted to have $S_{11} = 0$ for both the degenerate TE_{11} modes. This is in principle feasible since the calculated reflection coefficient are approximately equal for the two polarizations and it is always possible to adapt a single mode. However the design of a proper port adapter has not been performed during the work.

Comparison between exciters

Circular waveguide and Plane wave exciters behaves both better than electric dipoles if the Forward coupling coefficient is considered as a figure of merit. Moreover plane wave excitement have the added advantage that only one numerical simulation is required to process the
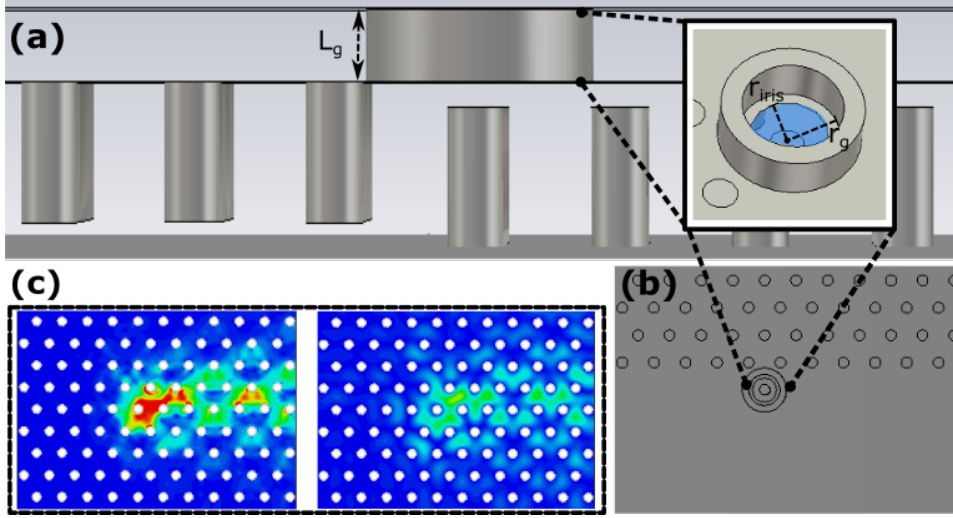
Fig. 4.4: front **(a)** and top **(b)** view of the circular waveguide launcher. **(c)**: Pointing vector Abs. Value (left) and E_z field profile (right). $r_g/r = 2.80$, $r_{\text{iris}}/r = 2.22$, $L_w = h$.

right excitation, while circular waveguides and electric dipoles requires two iterations (one per mode or dipole) and subsequent post processing. It is however important to note that, unless adaptation of CWG port, dipole excitation is by far the most efficient coupling system if the total percentage of coupled EM power is considered.

While circular waveguide exciter seems to be more ideal for microwave application it is important to say that most natural microwave sources can be modeled as plane wave if placed sufficiently far. Being the structure intrinsically chiral the possibility to excite one way modes from far plane wave sources can make the proposed TPMW a valuable tool in resolving the light polarization.

4.2.2 Single mode excitation

It has been stated in the previous chapter that the bulk-edge correspondence provides a principle to determine the number of TPSS along an interface between topologically non trivial mirrors. In the case of the studied TPMW the number of guided modes is given by (3.28) which relates to the spin-Chern number $\mathcal{C}_{gap}^{\uparrow(\downarrow)}$.

Since $\mathcal{C}_{gap}^{\uparrow(\downarrow)} = \pm 2$, there are two TPSS for every spin polarization (Fig. 3.15): a positive index (n^+) mode and a negative index (n^-) mode. Simultaneous excitation of both n^+ and n^- modes leads to the super-lattice periodicity pattern characterized by the spatial period $T_s/a_0 = 3$ visible in both Fig. 4.4 and 4.2. Single mode excitation is nevertheless
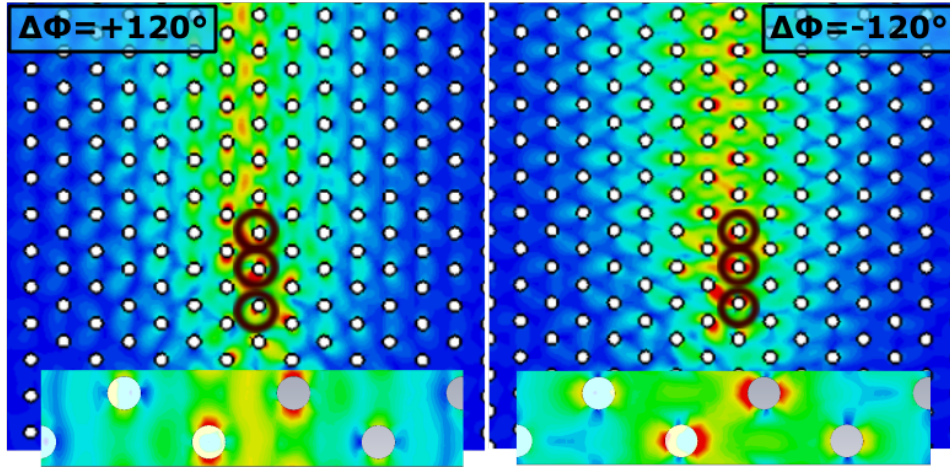
Fig. 4.5: Single mode excitation using 3 properly phased CP electric dipoles

possible by employing a phased dipole array as illustrated in Fig. 4.5 where an array of 3 CP Electric dipoles is used to selectively excite the positive/negative index modes. Inter-dipoles phase P is set in order to phase match the right mode accordingly to the dispersion diagram in Fig. 3.15 (i.e. for excitation frequency of 22.33GHz $P^+ = 120°$ is set for n^+ and $P^- = -120°$ for n^-)

Fig. 4.5 shows an example of simultaneous excitation of n^+ and n^- modes along with a comparison with the modes profiles from Fig. 3.16. Although the field map of Fig. 4.5 has been obtained with a phased electric dipoles array similar results could be obtained employing 3 circular waveguides as excitation and a suitably phased superposition of the 6 modes. A circular waveguides array however would be a very cost inefficient solution and several losses would occur by the coupling of the field radiated by each waveguide in the others guided modes. More sofisticated single-mode excitations could be obtained, as T.Ma *et al.* suggests [24], by phase matching a single mode with a plane wave impinging with a suitable angle on a linear slot cut in the top plate. This coupling mechanism has not been yet investigated.

Further developments

None of the above mentioned launchers is however well suited for a flexible interface with other devices. Rotating electric dipole sources, if ever they might be technologically feasible, would have to be inserted inside the structure itself which is highly uncomfortable. Circular waveguides are big and costly devices while plane waves are highly ideal sources. The need would be to develop a micro-strip launcher which could be

based on two linear slots cut on the top plate mimicking the behavior of a pair of electric dipoles feeded by an integrated 90° shifter and beam splitter, in order to excite the structure with a single feed. The development of such complex device falls outside the scope of this thesis and will be the object of future works.

4.3   Transmission around defects

The most important characteristic of TPSS is their unidirectionality which implies absence of back-scattering in the presence of spin-preserving defects. In general spin-preserving defects and discontinuities are all kind of defects that do not destroy the topological properties of the bulk PhC. Among them it is possible to count perturbations that changes the size of the bulk PBG without closing it, rotations of the unitary cell, scatterers along the guiding path, absence or dislocations of single isolated rods. One of the most interesting phenomena, however, is the insensitivity to sharp bends.

4.3.1   Bends

Starting from a bulk hexagonal crystal and appropriately choosing the position of the air gaps it is possible to realize edges arbitrarily bent by multiples of 60°, since theses bends do not change the overall crystal symmetry.

In Fig. 4.6a a doubly 120° bent TPMW is illustrated, as opposed to a W1-waveguide (4.6b). While the W1- waveguide is obtained by removing a row of rods and creating a pathway for the EM wave that is horizontally confined by the bulk PBG, the TPMW is localized at the interface indicated by the black dashed line. Rods to the right of the interface (highlighted in red) have the gap on the top, rods to the left have the gap on the bottom.

The difficulty in finding proper mode launchers for TPMW has already been stressed. In order to study the transmission spectrum of the doubly bent structure on 4.6a taking into account also the frequency responce of the excitators two series of field probes have been defined. 6 input probes have been placed at mid way between the dipole launcher (blu circle) and the first bend, separated by $a_0/2$ while 6 other dipoles have been placed at mid way between the second bend and the output (bottom left corner). The absolute value of the electric field amplitude is computed for every probe and the input and output mean amplitudes are defined as $\bar{E}_{in} = 1/6 \cdot \sum_{i=1}^{6} |E_i|$ and $\bar{E}_{out} = 1/6 \cdot \sum_{j=1}^{6} |E_j|$, where the subscript i stems the 6 input probes while the subscript j stems the 6 output probes. Finally the transmission is defined as
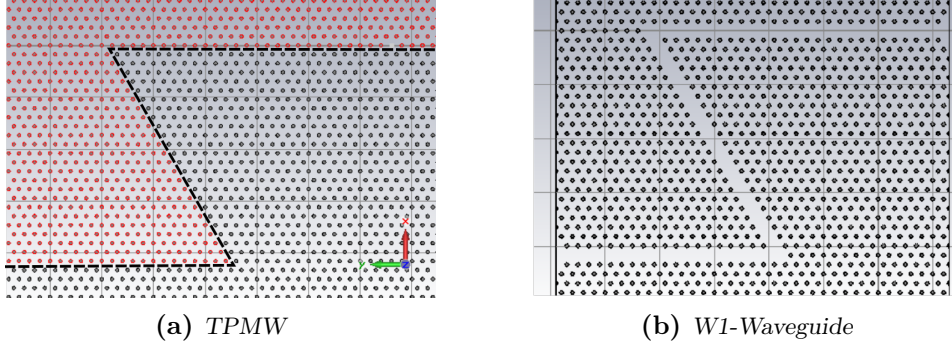
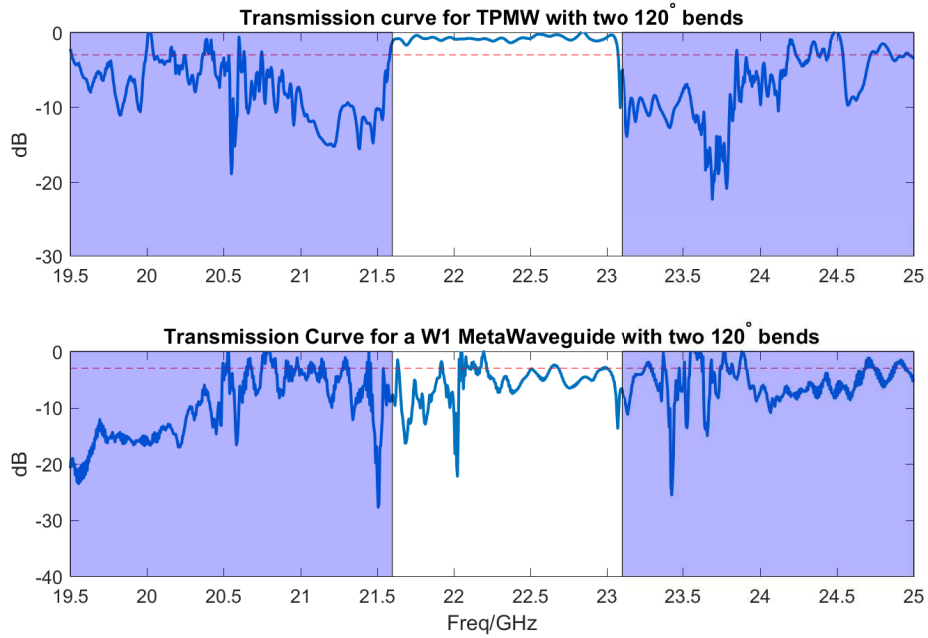**(a)** *TPMW*   **(b)** *W1-Waveguide*

Fig. 4.6

$T = 20 \log_{10}(\bar{E}_{out}/\bar{E}_{in})$. The need to average 6 individual values for the electric field arises from the fact that simultaneous excitation of both positive index and negative index modes causes a periodicity pattern of the field amplitudes with period $3a_0$ which can be seen also from Fig. 4.4 and4.2. The averaging, which in principle is not dissimilar from the procedure described in Ref. [20], aims at smoothing this pattern.

To underline the advantages of Topological Protection the Transmission curve of the structure in 4.6a is compared to the one of 4.6b, calculated with the same averaging mechanism, in Fig.4.7 While transmission for the TPMW is almost unitary for every frequency inside the PBG guided modes are hardly distinguishable from bulk modes in the w-1 waveguide.

It is important to say that the operating frequency of the TPMW is considerably higher then what should be the operating frequency of a w1 waveguide as in Fig.4.6b. The comparison between the graphs in Fig. 4.7 has thus not the claim to directly compare the performances of w1 waveguide with respect to TPMW, however a similar comparison that takes into account the different frequency range is available in [20]. What can be said, on the bases of the conducted analysis, is that TPMW performances outclass conventional topologically trivial guiding mechanism for equal frequency range and device footprint. The added advantage of TPSS is that the bend is intrinsically optimized for perfect transmission, since every perturbation on the lattice will affect topological protection and, eventually, impair transmission. while conventional PhC bends have to be tapered to remove the sharper parts, the position of air gaps itself is sufficient to obtain perfect transmission of TPSS.

The possibility to curve light with unitary efficiency on a broad band is of crucial importance in many field of engineering, however it

Fig. 4.7: Top graph: Transmission of TPMW, Bottom graph: Transmission of W1 Waveguide
The straight red line is fixed at -3dB for comparison and the shaded blue regions are the bulk bands of the PhC
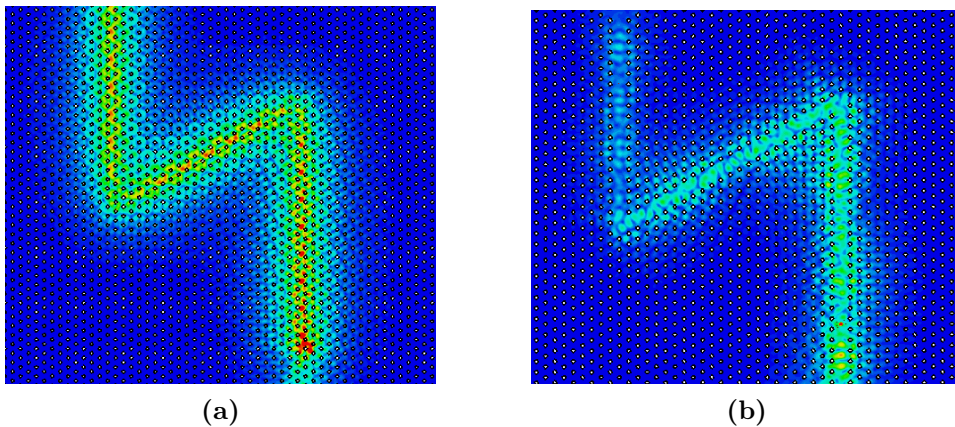
Fig. 4.8: Electric field absolute value map at $f = 22.37\,\mathrm{GHz}$ for a TPMW **(a)** and for a Topologically trivial W1 waveguide **(b)**

is not the only advantage provided by topological protection.

4.3.2   Other defects

vacancies

Conventional Photonic crystal resonators are obtained by removing a single rod by a bulk PhC and coupling light to the defect via a w1 waveguide. Since the operating wavelength of a W1 guide corresponds to $\approx a_0/2$, where a_0 is the reticular constant of the bulk PhC, the size of the defect permits to obtain sharp resonances, and high Q-factors are obtained for PhC cavities [27]. When it comes to guide light trough a PhC structure, however, the presence of a *missing rod* defect, or H0 defect, could actually destroy the propagating state of the W1 waveguide.
TPSS frequencies are conversely much higher with respect to H0 resonant modes thus the guiding states are almost completely insensitive to H-0 defects. If on the one hand this means that it is quite difficult to imagine cavities that benefits from Topologically Protected (TP), on the other it is also true that TP permits to construct guiding devices that are insensitive to a very critical defect.

Crystal Parameters

Among the PhC parameter themselves, namely the rods radius r and the gap size g it is relevant to note that the sensitivity of the TPMW to variations on r is not different from that of a topologically trivial Meta-Waveguide (MW). This is due to the fact that TE/TM degeneracy achieved in section 3.3 is indeed accidental, as it may be seen from Fig. 3.6a, indeed although the PBG arises even in the absence of polarization degeneracy the band gap remains Simulations have not been performed by us on the behavior of TPSS with randomized variations on r but TPSS are expected to be highly perturbed. On the other hand sensitivity to g is expected to be very weak as the analysis on section 3.5 Fig. 3.10b predicts. An overall change of g on the whole PhC has as a consequence the breaking of perfect orthogonality between $\Psi^\uparrow$ and $\Psi^\downarrow$ states, and a weak cross-talk between Fw and Bw modes is observed in our numerical simulations. This small effect (only around 1% of the light is coupled to spin-flipped modes) is however not observed if g is randomly perturbed, keeping the nominal value as average [23].
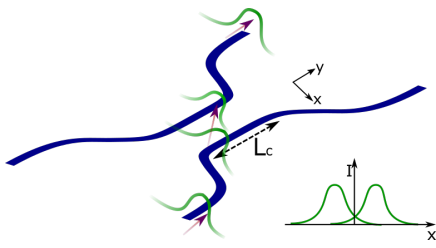
(a) *Schematic of a directional coupler. Waveguides in blue, modes intensity in green.*
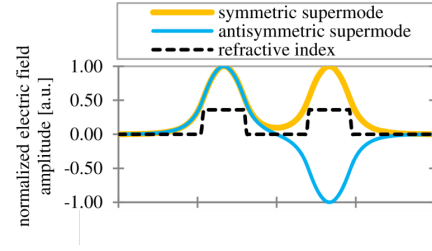
(b) *Symmetric and antysimetric supermodes of two coupled silicon waveguides (image from ref. [38])*

4.4   Coupled Topologically Protected MW

A large number of photonic devices is enabled by the possibility to realize sharp bends without losses. Another important feature for the realization of photonic circuits is the possibility to split light, by driving a certain percentage of light intensity to one or another port. Directional couplers and Y-junctions are very important devices for photonic applications because they permit to split and recombine lights. For example Mach Zehnder interferometers, massively used for WDM multiplexing, are obtained with a couple of directional couplers and a phase shift.
Due to the particular geometry of the TPMW Y-junctions sharing the same $\Psi^{\uparrow}$ modes are geometrically impossible, in order to split light it is then necessary to think about a directional coupler.

4.4.1   directional couplers theory

Directional couplers are obtained by placing two waveguides in close proximity for a limited length L_c. If light is guided inside one of the two waveguides within a mode that isn't abruptly going down to zero outside the guide, but decays as an evanescent field with a rate of γ (as it is the case with silicon waveguides or photonic crystal waveguides), then the evanescent fields of the two waveguide modes couples together leading to power transfer from one guide to the other (Fig. 4.9a).

The interaction length required to obtain a complete transfer of EM power from the input waveguide to the coupled waveguide is called *coupling length L_0*. There are basically two approaches in studying a composite system made by two coupled waveguides.

- Super-modes analysis

- Coupled Mode Theory

Super modes analysis

The supermodes analysis is based on the fact that a coupled lines structure with an $L_c \rightarrow \infty$ (i.e. a y-invariant structure) supports two lower order modes with symmetric and anti-symmetric profiles [2] (Fig. 4.9b. Where light is coupled inside a single waveguide a superposition of symmetric and anti-symmetric modes is excited (i.e. the left waveguide mode on 4.9b is $\psi_1 = \dfrac{\psi_e + \psi_o}{2}$). If the supermodes have slightly different propagation constant the coupling length is defined as the half beat length required to have a 180° phase shift between the two modes, as in (4.3)

$$L_0(\beta_e - \beta_o) = \pi \quad \Rightarrow \quad L_0 = \frac{\pi}{\beta_e - \beta_o} \tag{4.3}$$

It is evident that to decrease the coupling length, which is desirable in order to have lower footprint devices, it is necessary to increase the difference between the super-modes propagation constant.

Coupled Modes Theory

The super-modes analysis is only applicable if the structure is invariant, or can be considered invariant for a sufficient extent, along the propagation direction. If this is not the case, as in the case of a directional coupler when the coupling distance x_0 varies as a function of y) then the Coupled Mode Theory is required. The Coupled Modes Theory (CMT) [12, 26] is based on the study of power interplay between the two uncoupled waveguides modes. The Coupled Modes Equations (4.4) describes the amplitude A_1, A_2 of each lower order waveguide mode as a set of coupled differential equations [21] which, under the hypotheses

of balanced waveguides (i.e. the guides are identical), reads :

$$\begin{cases} \mathcal{P}_1 \dfrac{\mathrm{d}A_1}{\mathrm{d}z} = -j\mathcal{K}_{11}A_1 - j\mathcal{K}_{12}A_2 e^{j\Delta\beta z} + \mathcal{B}_{12}\dfrac{\mathrm{d}A_2}{\mathrm{d}z}e^{j\Delta\beta z} \\ \mathcal{P}_2 \dfrac{\mathrm{d}A_2}{\mathrm{d}z} = -j\mathcal{K}_{22}A_2 - j\mathcal{K}_{21}A_1 e^{-j\Delta\beta z} + \mathcal{B}_{21}\dfrac{\mathrm{d}A_1}{\mathrm{d}z}e^{-j\Delta\beta z} \end{cases} \quad (4.4)$$

Being,

$$\Delta\beta = \beta_1 - \beta_2$$

$$\mathcal{P}_i = \frac{1}{4}\int_S (\mathbf{E}_i^* \times \mathbf{H}_i + \mathbf{E}_i \times \mathbf{H}_i^*) \cdot \hat{\mathbf{n}}\,\mathrm{d}s$$

$$\mathcal{B}_{ij} = \frac{1}{4}\int_S (\mathbf{E}_i^* \times \mathbf{H}_j + \mathbf{E}_j \times \mathbf{H}_i^*) \cdot \hat{\mathbf{n}}\,\mathrm{d}s$$

$$\mathcal{K}_{1i} = \frac{\omega n^2}{4}\int_{S2} \mathbf{E}_1^* \cdot \mathbf{E}_i\,\mathrm{d}s$$

$$\mathcal{K}_{2i} = \frac{\omega n^2}{4}\int_{S1} \mathbf{E}_2^* \cdot \mathbf{E}_i\,\mathrm{d}s$$

Where β_1 and β_2 are the uncoupled waveguides mode propagation constants, S is the whole space cross section, S_1 and S_2 are the cross sections of the first and second waveguide, $\hat{\mathbf{n}}$ is the propagation direction (y for Fig. 4.9a)and $i, j = 1, 2$. $\mathcal{K}_{ii}$ parameters gives a measure of how much the perturbation represented by the second waveguide affects the uncoupled eigenmodes of the first waveguide and if the uncoupled modes are well confined and the distance between the waveguides is high enough they are usually neglected.

$\mathcal{B}_{ij}$ are called *Butt coupling* parameters and describes power coupling from one waveguide to the other via mode matching. They are normally neglected as well for large enough distance between the waveguides, when uncoupled eigenmodes are not too much perturbed.

$\mathcal{K}_{ij}$ are the *modes coupling* parameters, they represent the overlap integral of the guide's uncoupled eigenmodes calculated on the perturbation volume (i.e. $\mathcal{K}_{1i}$ are calculated on the second waveguide and vice versa). These parameters measures the power leakage from one one guide's mode to the other, therefore it is the main mechanism responsible for the power interplay.

Since $\mathcal{P}_i = \frac{1}{2}\int \mathrm{Re}\{\mathbf{S}\}\,\mathrm{d}s$ is the power carried by the mode in the propagation direction it is possible, to the scope of this discussion, to normalize each mode such to have $\mathcal{P}_i = 1$. In the case of two identical waveguides $\beta_1 = \beta_2$ is set and following the above mentioned simplifications (4.4) is recast into the following linear system, whose solution

comes from the initial conditions $A_1(0) = 1, \ A_2(0) = 0$

$$\begin{cases} \dfrac{\mathrm{d}A_1}{\mathrm{d}z} = \mathcal{K}_{12}A_2 \\ \dfrac{\mathrm{d}A_2}{\mathrm{d}z} = \mathcal{K}_{21}A_1 \end{cases} \Rightarrow \begin{cases} |A_1(z)|^2 = \cos^2(\mathcal{K}z) \\ |A_2(z)|^2 = \sin^2(\mathcal{K}z) \end{cases} \tag{4.5}$$

where $\mathcal{K} = |\mathcal{K}_{12}| = |\mathcal{K}_{21}|$, since from (4.3) it is evident that $\mathcal{K}_{12} = \mathcal{K}_{21}^*$. The results in (4.5) shows that the power flowing in one waveguide is completely coupled to the second waveguide after a propagation length of $L_0 = \dfrac{\pi}{2\mathcal{K}}$. The higher the coupling parameter, the shorter L_0.

It is important to note that the case of two slightly different waveguides leads to the non unitary phase term $\exp(\pm\Delta\beta z)$ multiplying the right hand sides of (4.5)that has the double effect of lowering the coupling length and limiting the maximum transferable power accordingly to the following relations

$$L_0 = \frac{\pi}{2\sqrt{\mathcal{K}^2 + \delta^2}}$$
$$P_{max} = \frac{\mathcal{K}^2}{\mathcal{K}^2 + \delta^2}$$
Where, \tag{4.6}

$$\delta = \Delta\beta/2$$

In the super modes theory framework the differences between the waveguides will instead lead to differences in the symmetric and anti-symmetric modes distributions for the two waveguides. This on the on hand leads to an increase of the difference between β_e and β_o, and subsequent decrease of L_0 and on the other prevents a complete interference between the two super modes, but the general formulation of the theory remains the same.
As a general rule, however, (4.4) tells that in order to have mode coupling the phase matching condition (4.7) has to be fulfilled.

$$\Delta\beta = \beta_1 - \beta_2 \approx 0 \ \ \Rightarrow \beta_1 \approx \beta_2 \tag{4.7}$$

The latter can be satisfied or by direct mode matching, that is employing identical waveguides or by grating assisted mode coupling, that is employing a grating with momentum β_g such that the modified Phase matching condition is satisfied:

$$\vec{\beta}_1 - \vec{\beta}_g - \vec{\beta}_2 = 0 \ \ \Rightarrow \vec{\beta}_g = \vec{\beta}_1 - \vec{\beta}_2 \tag{4.8}$$

The vectorial nature of (4.8) shows that grating assisted coupling permits to couple modes traveling in different directions, in particular it is possible to achieve contra-directional (CD) coupling by exchanging power from the forward mode of the input waveguide to the backward mode of the coupled waveguide.

4.4.2 CTPMW - geometry

Since the TPMW is made by an interface between z-reversed BPhC it is possible to realize a double interface with a structure as the one in Fig. 4.10
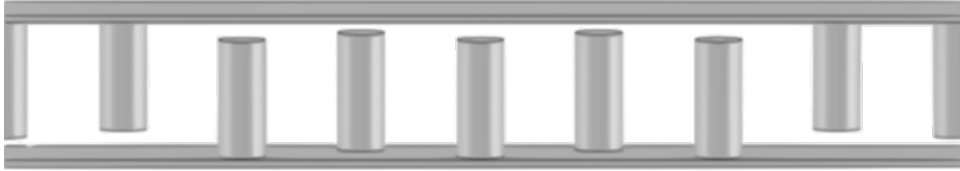

Fig. 4.10: Double interface corresponding to a directional coupler with guides separated by $n = 5$ rods

There are various fundamental problems in applying both of the previously described theoretical discussions to the Coupled TPMW (CTPMW) platform:

- The structure isn't properly y-invariant. Indeed although it can be modeled as discrete-translationally y-invariant the cross section cannot be defined. All the 2D integrals in (4.4) should be treated as 3D integrals on the whole super-cell, but to our knowledge there are not examples of similar calculations for PhC in literature.

- The TPMW supports 2 guided modes for every spin. This crucially complicates the description of the structure via the super modes theory. It is predicted that every guided mode should split in symmetric and anti-symmetric pairs, but the two couples of modes won't have the same coupling length, potentially leading to incomplete power transfer.

- Since the TPMW is defined only in the edge between BPhC the definitions for the mode coupling parameters in (4.4) would have to be redefined as S_1 and S_2 would be undefined.

Moreover the TPMW presents a peculiar dispersion relation, with both positive index and negative index modes, if these modes should couple topological protection of the spin states would be lost for the two CTPMW.
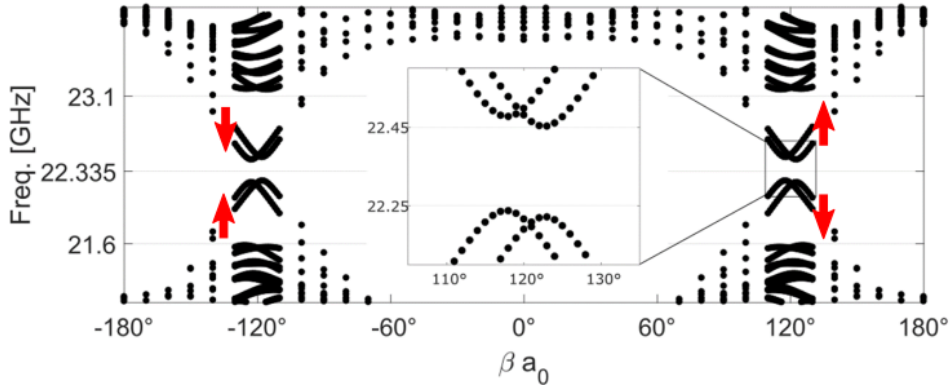
Fig. 4.11: Photonic Band Structure (PBS) of the double interface super-cell with $n = 5$ separating rods. Confined modes are visible inside the bulk PBG. Arrows: Spin states. Previously appeared in [6, 7]

4.4.3   CTPMW - eigenmodes

As a first attempt to understand the behavior of TPSS when subject to mutual interaction it is possible to calculate the dispersion of the double interface in Fig. 4.10 guided modes. This is done as usually with the super-cell method as it has been previously done for Fig. 3.15.

Fig. 4.11 shows the calculated dispersion relation for the CTPMW. Two main observations can be made:

- Symmetric and anti symmetric super modes are observed. Moreover positive index modes are subject to a wider splitting with respect to the negative index modes, suggesting a stronger coupling coefficient for n^+ with respect to n^-.

- A secondary band gap opens in the middle of the bulk PBG.

The first observation can be confirmed through inspection of the 4 eigenmodes that are observed for every given βa_0 (far from 120° where different coupling mechanism later on discussed occurs). Even 4.12a and odd 4.12b balanced recombination in Fig.4.12 yields the uncoupled eigenmodes (see Fig. 3.16 as a comparison)

4.4.4   Secondary frequency gap

The opening of a frequency band gap is the result of mutual coupling between counter propagating TPSS in the two waveguides (i.e. it is an example of CD coupling).

**(a)** *Even recombinations*   **(b)** *Odd Recombinations*
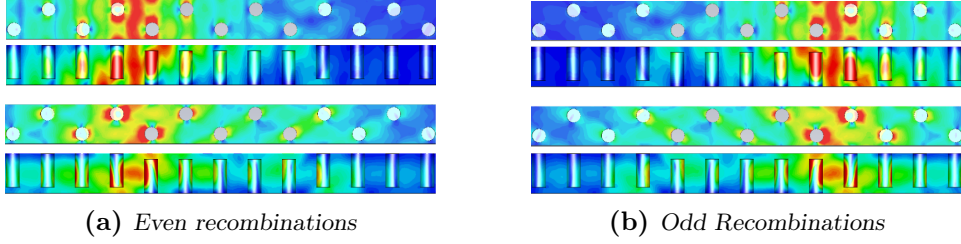
Fig. 4.12: Positive-K / Positive and negative-index CTPMW eigenmodes

The guided modes dispersion for the uncoupled TPMW of Fig. 3.15 shows, for $\beta a_0 = 120°$ degeneracy between two modes. These modes are a Fw spin up with positive index and a Bw spin down with negative index. The simultaneous presence of degenerate positive and negative index modes is protected by the time-reversal invariance of the waveguide and by the topological order or the band gap. Since there must exist 2 Fw and 2 Bw modes spanning the entire bulk PBG, degeneracy of spin reversed modes cannot be lifted by the anticrossing mechanism [15][2]. This is not in general true for trivial left-handed materials or PhC waveguides, which may or may not support modes with discordant signes [31] but their degeneracy is often removed by anti-crossing. The two degenerate modes are, for the uncoupled TPMW, orthogonal (due to spin conservation which have been demonstrated in 3.5). However the left interface in Fig.4.10 is z-symmetric with respect to the right interface (i.e. the right interface is an *up-down* interface while the left is *down-up*), which in fact reverses the spin definition for the two TPMW. When normally $\beta a_0 = 120°$ would correspond to a phase matching condition between two counter propagating waves that are in any case orthogonal, the orthogonality condition fails in the mutual coupling of z-reversed TPMW. Phase matching condition is thus satisfied for two counter propagating modes with the same spin polarization. The result is a counter directional coupling that results, in the eigenmode analysis modeling an infinite structure in the y direction, in the complete destructive interference between the counter propagating modes and, definitely, in the opening of a frequency gap. The amplitude of the secondary frequency gap is found to exponentially decrease with the distance d between the two CTPMW, which in turn can be defined only at discrete steps corresponding to a precise number n of separating rods. This indeed permits to obtain variable bandwidth for the CD coupling, enabling wide and narrow band responses with the

---

[2]The anticrossing is a phenomenon occurring when two different guided modes are expected to cross in the dispersion diagram. The band crossing is normally removed by a mutual coupling between the two modes mediated by the local phase matching condition.
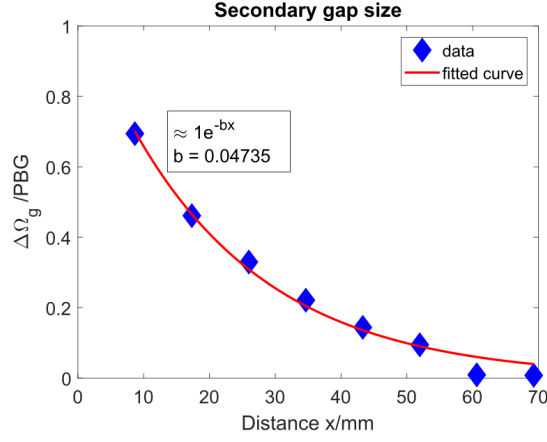
Fig. 4.13: Secondary gap size normalized to bulk PBG for varying coupling
distance

very same technology.

Fig. 4.13 shows the exponential behavior of the normalized gap
amplitude defined as (4.9):

$$\frac{\Delta f_{gap}}{PBG_b} = \frac{\min_{f>22.33\,\text{GHz}}(f) - \max_{f<22.33\,\text{GHz}}(f)}{PBG_b} \tag{4.9}$$

where,
$$PBG_b = (23.1 - 21.6)\text{GHz} = 1.5\,\text{GHz}$$

Although similar results can be obtained for grating assisted waveg-
uide couplers [36] and PhC waveguides [14, 31] this is the first time,
to our knowledge, that pure CD coupling is achieved employing two
identycal waveguides as a direct result of topological protection of the
surface states. Previous approaches to CD couplers design are infact
based on the use of different waveguides in order to suppress the cou-
pling with the input waveguide's backward mode. On the contrary
spin conservation enables the use of identical TPMW since backward
coupling is prohibited. Moreover Fig. 4.11 shows a bandgap, thus a
CD bandwidth, considerably larger than that of Ref. [14, 31].

The methods that can be thought of in order to analyze the behavior
of the secondary gap in relation to the distance between the waveguides
and possibly calculate the bandwidth of the secondary gap are various:

- Development of an analytical model for the phase matching band-
  width

- Analysis of the mode coupling coefficient

The development of an analytical model to calculate the phase matching bandwidth of counter propagating and spatially separated TPSS lies outside the scope of this thesis and may be the object of future work.
On the other hand it has been shown [31] that the bandwidth of a CD coupler can be approximated with (4.10)

$$\Delta f = \frac{2 \cdot c \cdot \mathcal{K}}{\pi(n_+ + n_-)} \tag{4.10}$$

Being the direct calculation of the coupling coefficients impaired by the problem of the integrals domain in (4.4) a possible strategy would be the indirect calculation $\mathcal{K}$ by examination of the CD coupling full width at half maximum. In order to perform such calculation precise input and output ports should be defined and sharp transmission curves have to be calculated, which is not the case considering the difficulties in the mode excitement. Moreover (4.10) refers to CD couplers in weak coupling regime. The coupling strength of our CD coupler cannot be defined weak, because the coupling bandwidth is indeed very large thus (4.10) cannot be straightforwardly applied.

For the sake of completeness it is important to note that being the CTPMW a 4 modes coupler the CMT have to be reformulated as a set of 4 coupled differential equations. The mode coupling coefficients are 16 in total but many of them vanishes due to spin-conservation, the relevant are: $\mathcal{K}^{\uparrow\uparrow}$, $\mathcal{K}^{\downarrow\downarrow}$, $\mathcal{K}^{\uparrow\downarrow}$, $\mathcal{K}^{\downarrow\uparrow}$ all with an implicit sub-index $\mathcal{K}_{RL}$ (complex conjugation of the quadruplet leads to the four $\mathcal{K}_{LR}$). The first two contributing to forward coupling of the positive and negative index modes[3] and the second two contributing to CD coupling. Direct calculations of these mode coupling coefficients have been performed by treating the surface integrals as volume integrals but did not provide insightful results. The problem of calculating the coupling strength thus the transmission of an arbitrarily long coupler without the need to perform F-W simulations on every structure is thus still open.

4.4.5   CTPMW - multiport coupler

The eigenmode analysis is valid only for a discrete-translationally y-invariant structure, where the coupling distance remains the same. The

---

[3]Let's here recall that spin-down negative-index modes that we can find for $\beta > 0$ are Kramer degenerate with spin-up negative-index, which are located at $\beta < 0$ thus $\mathcal{K}^{\downarrow\downarrow}$ formally representing the cross coupling of spin-down negative-index modes is the same coefficient that contributes to the cross coupling of spin-up negative-index modes.

coupling region can be restricted to a section L_c employing a couple of tapers, as illustrated in Fig. 4.14, to model the behavior of a true device.
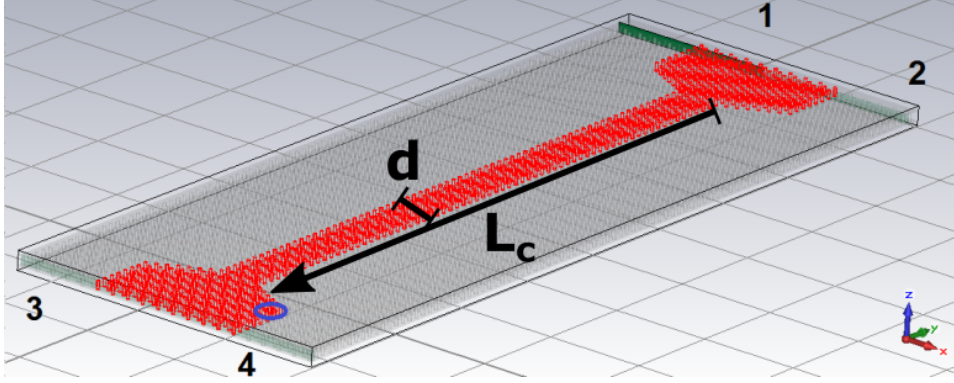
Fig. 4.14: CTPMW with coupling section $L_c/a_0 = 70$ and distance $d/a_0 = n\sqrt{3}/2$, with $n = 5$. Excitation happens in the lower left corner, in correspondence with the blue circle.

The structure can be excited with all the methods described in 4.2 although the most practical one to minimize computational effort seems to be the CP Plane wave ($r_{in}/r = 1.2$ has been used). The simulation is carried out using CST MWS $^{\text{TM}}$ transient solver on a very large computational domain [4] in order to empirically observe the coupling length. The boundaries are defined as impedance walls for the $\pm y$ directions (as described in section 4.1) and Perfect Electric Conductor (PEC) for $\pm x$ and $\pm z$ (apart from the input disk at $+z$). What is expected from the simulation is a classical Directional Coupler behavior with a characteristic coupling length L_0 for frequencies inside the bulk PBG and outside the secondary gap (i.e. $f \in [21.6, 22.25] \cup [22.45, 23.1]$GHz) while for frequencies inside the secondary gap ($f \in [22.25, 22.45]$GHz) CD coupling will happen and the input power will be back transmitted through the second waveguide. Fig. 4.15 shows the 2D map of the electric field absolute value in the cutting plane $z = 0$ (middle of the structure), each field is normalized to the maximum value. Normal forward coupling is observed for all frequencies outside the CD bandwidth with a coupling length that weakly depends on the field frequency. Inside the secondary gap CD coupling is observed with a fast decay rate.

---

[4] 35 cm x 90 cm, being $L_c = 70$ unit cells, $d = 5$ rods and $n_s = 10$ rods per side in the taper regions
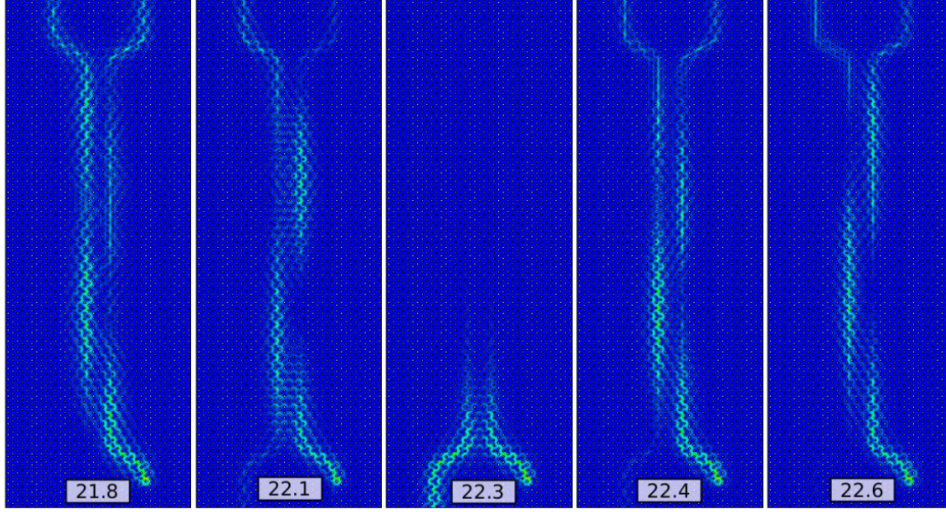
Fig. 4.15: electric field maps normalized to the maximum value for different
frequencies inside the bulk PBG

To quantify the power carried by each guide's TPSS we define power
monitors for a discrete set of frequencies and the 4 virtual surfaces in
green on Fig. 4.10. The total power flow trough the surface A_i is then
calculated as $P_{A_i} = \int_{A_i} S_y \, \mathrm{d}s$ and transmission for each port is defined
as the power flux P_{A_i} normalized to the total power flux on all the
surfaces (i.e. $T_i = P_i/(P_1 + P_2 + P_3 + P_4)$)
Results in Fig. 4.16 shows a wide band transmission drop for both
ports 3 and 4 while port 2 experiences a peak. The center frequency
of the CD coupling as derived from Fig. 4.16 is subject to a shift with
respect to what was expected, this is not a serious issue because:

- Eigenmodes simulation are performed employing a tetrahedral
  meshing system while Time Domain simulation uses hexaedral
  mash. Such strong differences in the meshing system unavoid-
  ably leads to numerical differences in the results.

- The shift is indeed small: while from eigenmode simulation the
  expected center frequency is $f_0 = 22.35 \, \mathrm{GHz}$, from interpolation
  of data in 4.16 $\tilde{f}_0 = 22.25 \, \mathrm{GHz}$ is obtained. The relative error is
 thus defined as $\epsilon = \dfrac{f_0 - \tilde{f}_0}{f_0} < 0.5\%$.

The calculation of the coupling length for every frequency point is
carried out with a spatial Fourier analysis of the field profiles. The
absolute value of the Electric field magnitude in the line corresponding
to each waveguide is plotted as a function of the distance (Fig.4.17 up)
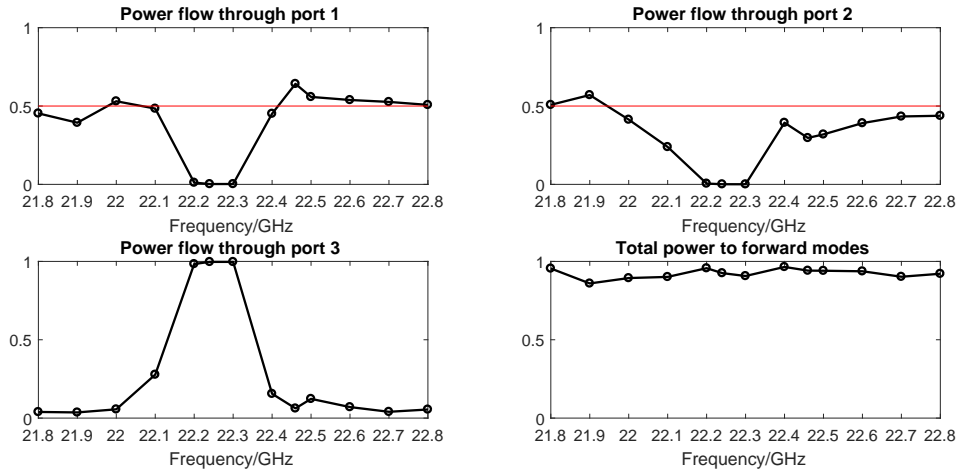
Fig. 4.16: Power flow truough the surfaces defined in Fig. 4.10

and spatial Fourier transform is performed. In order to obtain smooth results on the spatial Fourier transforms for such low spatial frequencies (it is evident that the coupling length corresponds to several lattice periods) it is necessary to perform a very strong zero padding, indeed the spatial Fourier transform has been calculated on 3148 points while only 2225 nodes from $0\,cm$ to $70\,cm$ have been used. The resulting Power Spectral density for the spatial frequency components is then filtered to ignore any component shorter than 1 reticular constant. Bottom plots in Fig.4.17 corresponds to the calculated PSD for two frequencies on the second waveguide.   The high frequency peaks are centered around 0.033 which correspond to 3 lattice constants and are thus the components related to the n^+ / n^- interference pattern. The LF peak instead represent a pattern with period $P/a_0 > 10$ and is therefore compatible with the observed coupling length. The algorithm is used to calculate the coupling lengths on all the available frequency samples for both the input and the coupled waveguides. The results versus frequency are reported in Fig. 4.18.

As the simulated structure contains only about 2 coupling lengths the performed calculation is not intended to provide precise results, howsoever the presented automatic algorithm shows values for L_0 that are not dissimilar from what it can be inferred by looking at the field maps and the accuracy can be enhanced by enlarging the calculation domain to contain several L_0. Unfortunately, this would require a completely different kind of machine since the computational efforts of a F-W simulation greatly increases with the size of the domain and becomes hardly manageble without parallel computing and several Gbs of

(a) 21.8 GHz   **(b)** 22.1 GHz
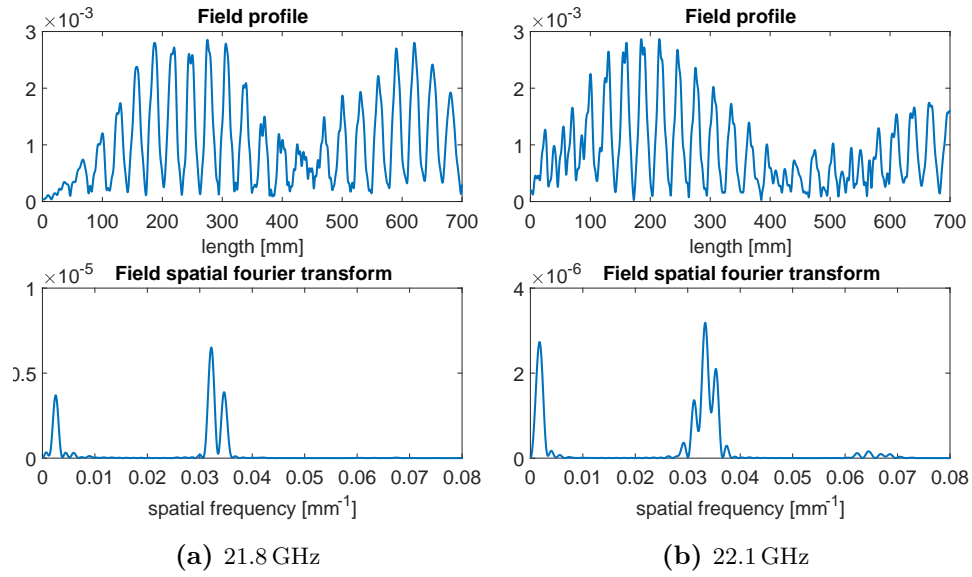
Fig. 4.17: Electric field absolute value (top plot) and spatial fourier transform (bottom plots) for two different frequencies calculated on the coupled waveguide
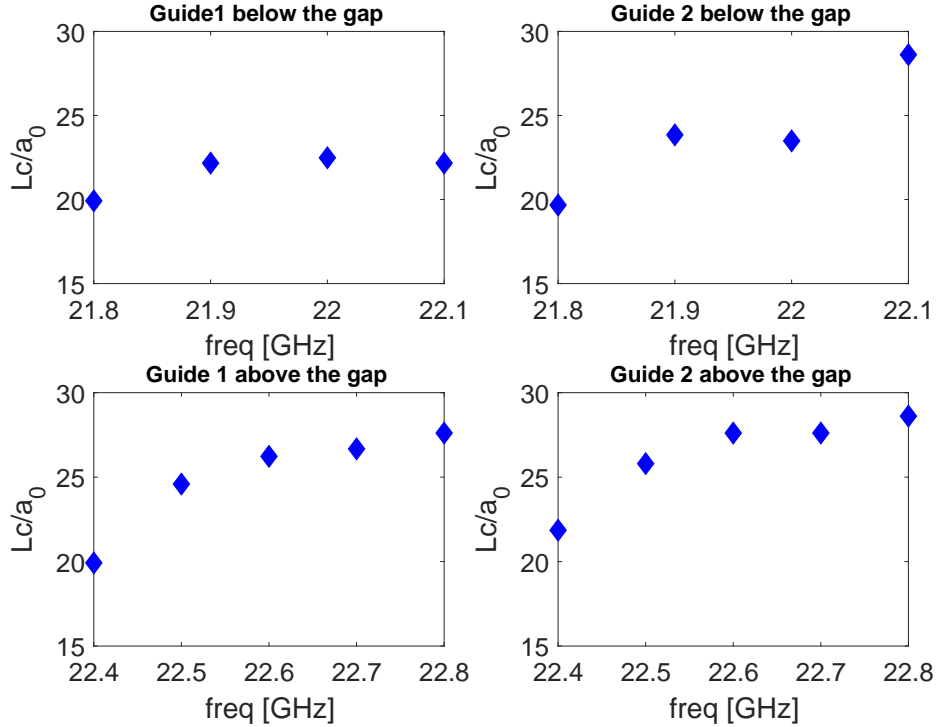
Fig. 4.18: observed coupling length employing field spatial fourier analysis

RAM. The method ultimately shows that, apart from an increase at the highest frequencies of the PBG, the coupling length does not strongly depend from the input wavelength. This feature enables the use of the directional coupler as a wide band 3dB splitter, that is one of the two foundamental parts of an integrated Mach Zender Interferometer. The other fundamental device to enable interferometry based filtering is a phase delay. To that end it has been experimentally demonstrated [20] that the platform here described can be used to realize wide band delays with a very linear behavior.

Lc = 30 CPTMW

To conclude the study, as suggested by the values in Fig. 4.18, a coupler with a length $L_c/a_0 = 30$ is realized. 3 different Field probes are defined at every exit port, equally spaced at a distance a_0 in order to smooth the periodicity pattern as it has been done in 4.3. The structure is excited with a CP plane wave impinging on a circular hole cut in the top plate with radius $r_{in}/r = 2$. The electric field absolute values for every probe are recorded at every frequency inside the bulk PBG and the mean value for every port is computed.

Fig. 4.19 shows the values for the fields intensities at every port. The frequencies inside the contra-directional (CD) bandwidth shows 10dB attenuation for the forward ports. The attenuation of the CD frequencies at the forward ports depends on the coupler length, longer coupling sections L_c leads to sharper contra-directional coupling. However the fact an attenuation of 10dB is provided with only 30 reticular constants and even with relatively large inter-guide distance is relevant and is a direct consequence of the perfect phase matching between forward and backward waves. From Fig. 4.19 it is also possible to observe the frequency behavior of the coupling length. The splitting ratio (defined as $I_{\mathrm{cross}}/(I_{\mathrm{bar}} + I_{\mathrm{cross}})$) is constantly increasing at higher frequencies, the same behavior is observed in Fig. 4.18.

As an example of the flexibility that such device could provide in term of possible frequency response, Fig.4.20 shows the field maps for 3 relevant frequencies. At 21.8 GHz the expected coupling length from 4.18 is $L_0 = a_0$, thus after $L_c = 30a_0$ a splitting ratio of 1/2 is expected. The observed splitting ratio from 4.19 is not exactly 1/2 as the output taper sections weakly contributes to the total coupling and other phenomena intervene, but the field maps shows that an output is achieved at both Bar and Cross Ports.
At 22.33 GHz the peak contra-directional coupling is expected and the theoretical expectations are confirmed by the field maps.
Finally at 22.8 GHz the coupling length is expected to rise up to $L_0 =$
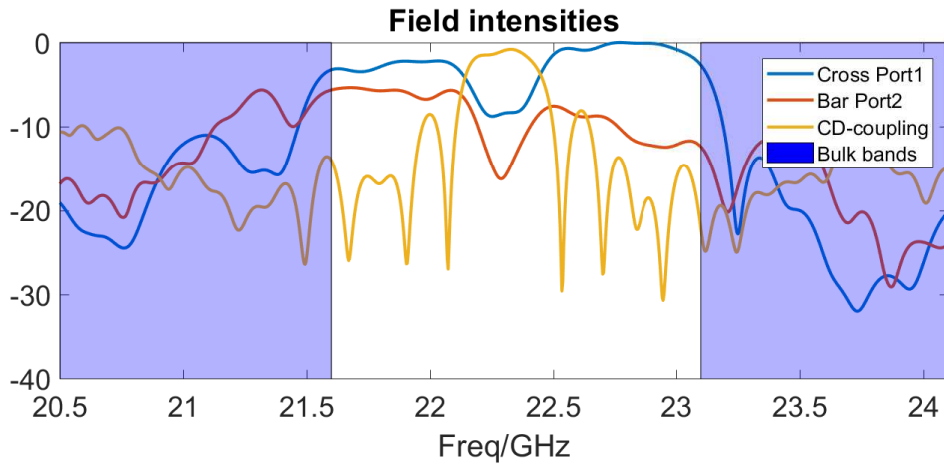
Fig. 4.19: Frequency responces of every output port defined as the squared mean absolute value of three closely placed electric field probes. The contradirectional bandwidth is clearly visible as well as a clear distinction between bulk modes (shaded blue regions, outside the bulk PBG) and guided modes (inside the bulk PBG) can be observed.
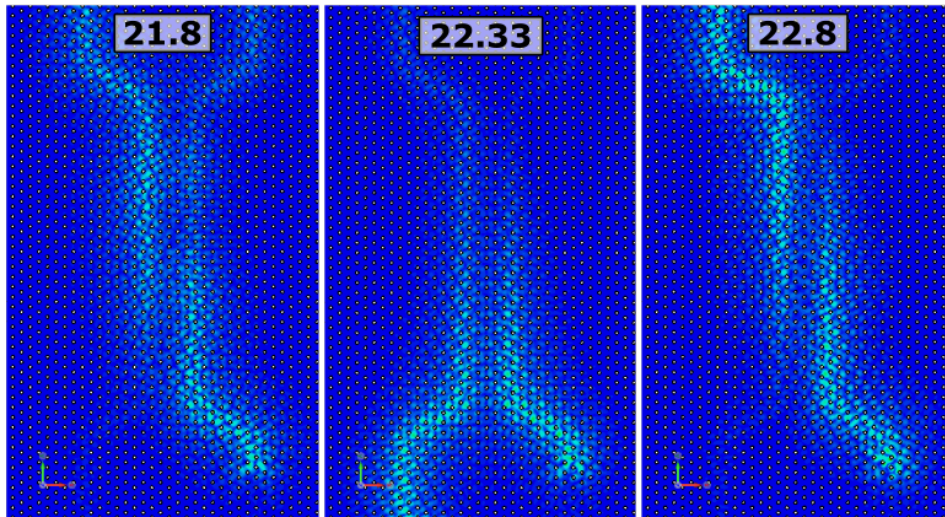
Fig. 4.20: Electric field absolute value for 3 relevant frequencies in the middle plane of the structure (z = 0). Excitation happens in the upper right corner

$30a_0$ thus complete cross state is expected. Fig. 4.19 shows an attenuation on the Bar port of 15dB, the field map shows the electric field concentrated on the Bar Port.

Further comments

Where the coupling is co-directional $\Psi^\uparrow$ states are propagating in the coupled waveguide. Remembering that the spin state definition is inverted for the input and coupled waveguides it is now clear that the device can act as a polarization inverter when $L_c = L_0$ (i.e. cross-state). It has already been suggested that the polarization-chirality of the structure might be a key feature for possible quantum computing application, the possibility to invert the polarization adds new features to the photon manipulation capability of the proposed TPMW.

4.5   further developments

The fundamental properties of Topologically Protected transport have been illustrated, and a detailed study of a directional coupler, as an example of practical device, have been carried out. Other observations that have been made during the thesis period and projects that may be studied in future are presented hereafter.

Electrically tune dispersion relations

The spatial field profile of the guided modes in Fig.3.16 shows a strong confinement of the field inside the air gap.

This suggests a possible upgrade to the structure in order to obtain modulation capabilities. As a consequence of the variational principle Th.1 stated in the second chapter filling the air gap region with a dielectric, as is it illustrated in Fig. 4.21, is expected to lead to a frequency modulation for the modes confined in that region.
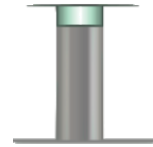
Fig. 4.21

Since the unperturbed PBS in Fig. 3.6b is clearly not affected by the dielectric perturbation (as there is no gap) the discussion on TE/TM degeneracy enabling topological protection is still valid. We can further on imagine that the effect of a dielectric load is not dissimilar from a perturbation on the gap size for what concerns the discussion in 3.5 thus it shouldn't affect too much topological protection of the guided modes.

No relevant changes on the bulk PBG are indeed observed for a dielectric perturbation of $\epsilon_r = 3$ as it might be seen from Fig.4.22a related to 3.6b. The depicted dispersion diagram shows an unperturbed
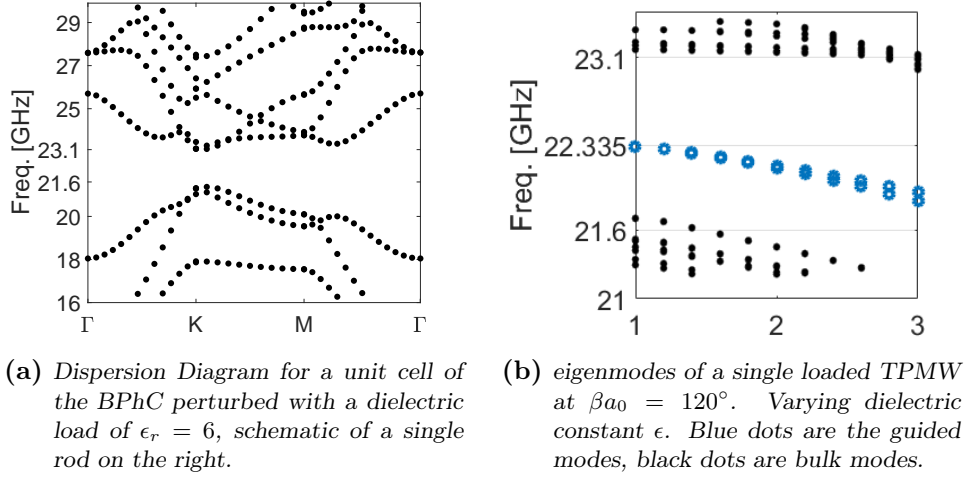
(a) *Dispersion Diagram for a unit cell of the BPhC perturbed with a dielectric load of $\epsilon_r = 6$, schematic of a single rod on the right.*

(b) *eigenmodes of a single loaded TPMW at $\beta a_0 = 120°$. Varying dielectric constant ϵ. Blue dots are the guided modes, black dots are bulk modes.*

Fig. 4.22

behavior for what concerns the band edges, while the upper bands presents a slight red shift in the Γ point, nevertheless the topological properties are related to the behavior of the band edges around the K point, thus the observed red shift is irrelevant as long as topological protection is considered. Finally the band structure of the single and double super-cell loaded with dielectrics is calculated.

Fig. 4.22b shows the eigenfrequency of the perturbed TPMW at the point $\beta a_0 = 120°$ of the dispersion diagram in Fig. 3.15 for various values of permittivity ϵ. It is possible to see a global red shift of the single interface guided modes (which however remains degenerate for sufficiently small perturbations) from the unperturbed case ($\epsilon = 1$) to the maximum perturbation $\epsilon = 3$ where degeneracy is broken. It is not surprising that the guided modes degeneracy breaks as the effect of the dielectric perturbation because as it may be observed from Fig.3.16 the negative index mode as a field intensity more confined into the gap region with respect to the positive index mode, thus it will be more affected by the perturbation.

The shift is observed also on the loaded CTPMW PBS, that is shown aside to the unperturbed one in Fig.4.23, with strength sufficient to move the perturbed secondary gap completely outside the unperturbed one.

This gives the possibility to exploit electro-optical effect to tune the position of the secondary gap, enabling devices like OOK modulators or re-configurable routers.
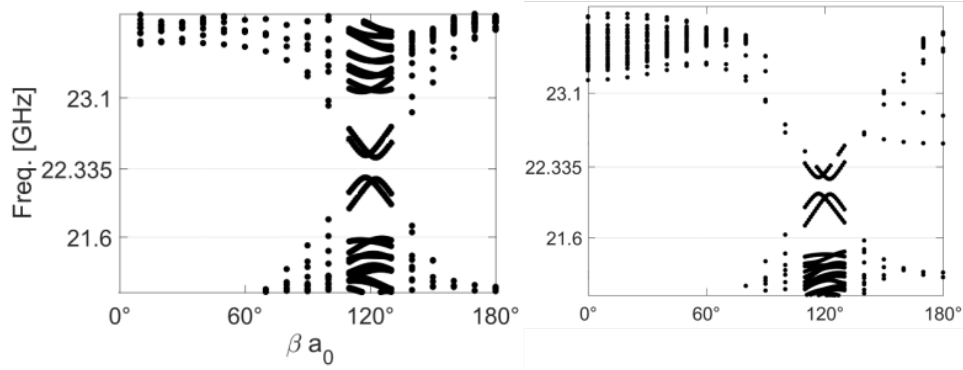
Fig. 4.23: positive half of the dispersion diagram for both unperturbed (left) and perturbed (right) CTPMW.

6-way splitter

Since Y splitters cannot be realized with interfacial states, it is possible to think about more complex power dividers. A device like the one illustrated in Fig. 4.24, where each dot is a rod and the position of the gap is mapped with the color, is composed by 6 TPMW that can be divided in 2 groups. The green-red (or down-up) and the red-green (or up-down) interfaces. Power exchange from one group to the other is inhibited by spin conservation, in fact $\Psi^\uparrow$ states are Fw states for red-green interfaces, but Bw states for green-red. An impinging $\Psi^\uparrow$ state from port 1 is thus expected to propagate only along the interfaces indicated by arrows in Fig.4.24. The percentage of power that goes in every guide will depend from the design of the splitting section, in particular each one of the three green rods highlighted by the blue circle can be changed to a red dot without affecting the global topology. This device deserves an accurate study because a large number of output combinations can be achieved by impinging with different states on different ports. In general input power from an odd port will split in all the even ports (eventually with equal ratio), while input power from an even port will split into the odd ports. This means that up to 3 simultaneous waves could be mixed on the even ports by inputting power in all three odd ports. Although F-W simulations of this structure are not available yet, in case successive works would confirm the theoretical expectations on this geometry it could prove useful in a number of applications as routers, multiplexer and add filters.
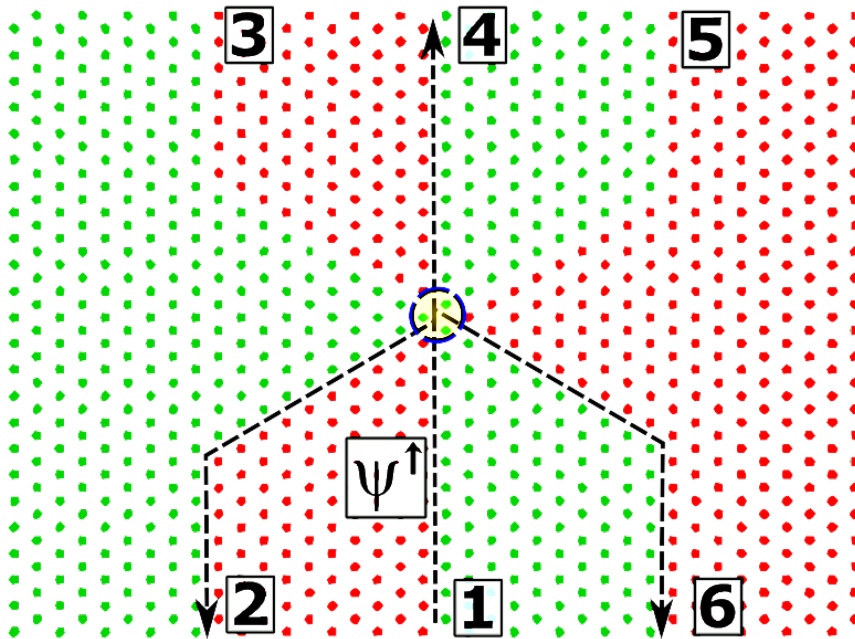
Fig. 4.24: Schematic of a 6 way "spider coupler". Red(green) dots represent rods with the gap in the bottom(top) position and arrows represent the possible propagation directions for a $\Psi^\uparrow$ state coming from port 1

Conclusions

TOPOLOGICAL properties of matter are as exciting as a novel field of physics can be. Where technology characteristic sizes become constantly smaller and physical quantum limits approaches, the study of interfaces and lower dimensional systems acquires an invaluable importance. Topological properties of interfaces configures as a very precious tool to control surface phenomena and engineer novel technologies. Unfortunately an accurate study of topology in solid state matter seems to be quite far from today's technological possibilities and the field is at present full of intriguing but so far only theoretical proposals. The ever present analogy between Photonic Crystals and Solid state matter can prove as a priceless tool in the hands of experimental physicist to better understand topology and phenomena happening at the interfaces between topologically in-equivalent material. Electromagnetic simulations of arbitrarily complex structures are well in the possibilities of today's computers while the scale in-variance of Maxwell's equations permits the study of large scale photonic structures with high precision prior to its scaling toward more technologically useful frequencies.

While topologically protected electron transport can be observed only at very low temperature regime and requires extremely costly equipments, the benefits of topological protected transport for microwave devices appears as plain as the day even with the use of a budget Personal Computer (CPU: single intel ^{TM} i7 3770k, RAM: 16Gb DDR3 dual channel). On the other hand implementation of Topologically Protected Photonic transport is a technological issue, impaired by the difficulty of high precision manufacturing of Photonic Crystals, but the advantages brought by topological properties of Photonic Crystal

are evident and has been experimentally demonstrated by other groups employing a large scale structure operating at millimeter wavelengths.

In the framework of this work the most recent proposals for obtaining topologically protected photonic transport have been studied with a focus on a metallic metawaveguide based on a photonic analogue of Quantum Spin Hall Effect, where bianisotropy substitutes the intrinsic Spin-Orbit Interaction of the well known Quantum Spin Hall Effect (QSH) Topological Insulators (As HgCdTe quantum wells)

The mathematical formulation of Topologically Protected Transport of EM waves in the metallic bianisotropic metawaveguide has been reviewed and the features of Topologically Protected Edge States have been observed trough numerical simulations.

The behavior of Coupled Topologically Protected Edge States, when two metawaveguides are interacting thanks to evanescent field coupling, has been extensively studied employing a formulation of the coupled mode theory for periodic structures, and their exploitation in the design of an efficient multi-port bidirectional coupler has been illustrated.

Insertion losses are the *all time* problem of photonic crystals. While (technological difficulties put aside) photonic crystals are advantageous to be monolithically integrated, their interface with fibers or sensors, impaired by the huge mismatch in the mode profiles, has represented one of the main impeachment to their massive diffusion. Photonic Surface States are a nearly un-investigated propagation channel and the mode mismatch is even larger due to the virtually infinitesimal lateral extension of a surface state. Future works will have to focus on the development of easy and efficient I/O interfaces that may be, for example, based on plasmonic waveguides or evanescent (Butt) coupling but also on microstrip circuits and patch antennas that provides the possibility to design a complete launcher with ready to use technologies. If a proper I/O system is found demonstrators of virtually all the described devices could be realized on Substrate Integrated Waveguide technology (Fig.5.1). This technology has been widely used to realize microwave waveguides integrated inside the substrate of a classical microstrip, but since there's no limit on the number of metal vias that can be realized it could prove useful also for the realization of slab rods-on-air Photonic Crystals, where naturally air would be replaced by a dielectric, causing an overall red shift of the frequency range. The problem to be addressed in using SIW technology is the realization of the "air gap" since the metal vias should not completely transverse the substrate, the latter might be object of future works.
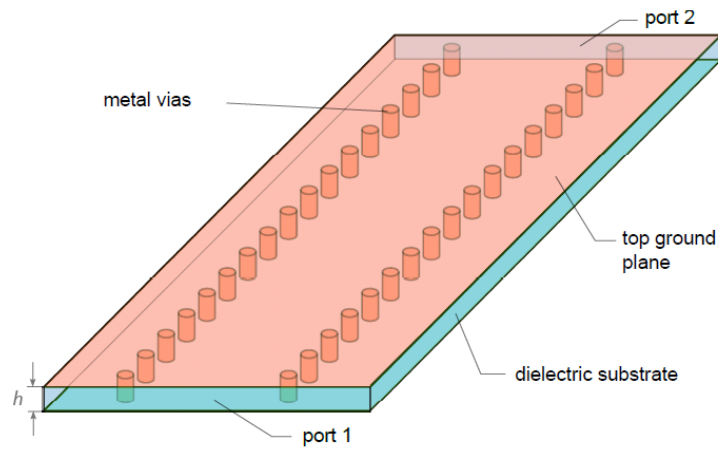
Fig. 5.1: Substrate Integrated Waveguide (SIW) Technology overview

Apart from the already mentioned value of Photonic Topologically Protected Structures for theoretical research purposes, under the availability of efficient coupling systems and relatively low cost technologies spin-chiral structures would provide a large class of benefits for microwave to photonic circuits applications though their non reciprocity with respect to the photon polarization. Devices that may benefit from photonic spin topological protection includes polarization dependent beam splitters, circularly polarized antennas, high efficiency sensors, and quantum computing, where topologically protected surface states might be used to interface polarization encoding with path encoding.

Bibliography

[1] B. Andrei Bernevig, Taylor L. Hughes, and Shou-Cheng Zhang. Quantum Spin Hall Effect and Topological Phase Transition in HgTe Quantum Wells. *Science*, 314(5806), 2006.

[2] William K. Burns. Normal Mode Analysis of Waveguide Devices. Part I: Theory. *Journal of Lightwave Technology*, 6(6):1051–1057, 1988.

[3] M. Pozar David. *Microwave engineering*. Wiley, Hoboken, NJ, 2011.

[4] Giuseppe Della Valle. Lecture Notes in nano optics. In *LM Engineering Physics, Politecnico di Milano*, Milano (MI), 2016. Classes held in May-June.

[5] Nicolas Descharmes, Ulagalandha Perumal Dharanipathy, Zhaolu Diao, Mario Tonin, and Romuald Houdré. Observation of backaction and self-induced trapping in a planar hollow photonic crystal cavity. *Physical Review Letters*, 110(12), 2013.

[6] Gian Guido Gentili, Giuseppe Pelosi, Francesco Piccioli, and Stefano Selleri. On a frequency gap appearing in topologically protected Coupled Lines Structures. In *II International Workshop on MetaMaterials by Design*, Riva del Garda (TN), 2016. Presented as Poster.

[7] Gian Guido Gentili, Giuseppe Pelosi, Francesco Piccioli, and Stefano Selleri. Coupled topologically protected metawaveguides. In *2017 IEEE International Symposium on Antennas and Propagation & USNC/URSI National Radio Science Meeting*, pages 59–60, San Diego (CA), 2017.

[8] Gian Michele Graf and Marcello Porta. Bulk-Edge Correspondence for Two-Dimensional Topological Insulators. *Communications in Mathematical Physics*, 324(3):851–895, 2013.

[9] F. D M Haldane. Model for a quantum hall effect without lan-
     dau levels: Condensed-matter realization of the "parity anomaly".
     Physical Review Letters, 61(18):2015–2018, 1988.

[10] F. D M Haldane and S. Raghu. Possible realization of directional
     optical waveguides in photonic crystals with broken time-reversal
     symmetry. *Physical Review Letters*, 100(1), 2008.

[11] M. Z. Hasan and C. L. Kane. Colloquium: Topological insulators.
     Reviews of Modern Physics, 82(4):3045–3067, 2010.

[12] H. Haus, W. Huang, S. Kawakami, and N. Whitaker. Coupled-
     mode theory of optical waveguides. *Journal of Lightwave Technol-
     ogy*, 5(1):16–23, 1987.

[13] Daniel A. Jacobs, Andrey E. Miroshnichenko, Yuri S. Kivshar,
     and Alexander B. Khanikaev. Photonic topological Chern insu-
     lators based on Tellegen metacrystals. *New Journal of Physics*,
     17(12):125015, 2015.

[14] Vakhtang Jandieri, Kiyotoshi Yasumoto, and Jaromir Pistora.
     Coupled-mode analysis of contra-directional coupling between two
     asymmetric photonic crystal waveguides. *Journal of the Optical
     Society of America A*, 31(3):518, 2014.

[15] John D Joannopoulos, Robert D Meade, and Joshua N Winn.
     Photonic Crystals. Princeton University Press, Princeton (NJ),
     1995.

[16] C. L. Kane and E. J. Mele. Quantum Spin hall effect in graphene.
     Physical Review Letters, 95(22), 2005.

[17] C. L. Kane and E. J. Mele. PHYSICS: A New Spin on the Insu-
     lating State. *Science*, 314(5806):1692–1693, 2006.

[18] Alexander B. Khanikaev, S. Hossein Mousavi, Wang Kong Tse,
     Mehdi Kargarian, Allan H. MacDonald, and Gennady Shvets.
     Photonic topological insulators. *Nature Materials*, 12(3):233–239,
     2013.

[19] Markus Koenig, Steffen Wiedmann, Christoph Bruene, Andreas
     Roth, Hartmut Buhmann, Laurens W. Molenkamp, Xiao-Liang
     Qi, and Shou-Cheng Zhang. Quantum Spin Hall Insulator State
     in HgTe Quantum Wells. *Science*, 318(5851), 2007.

[20] Kueifu Lai, Tsuhsuang Ma, Xiao Bo, Steven Anlage, and Gennady Shvets. Experimental realization of a reflections-free compact delay line based on a photonic topological insulator. *Scientific Reports*, 6(1), 2016.

[21] B E Little and W P Huang. Coupled-Mode Theory for Optical Waveguides. *Progress in Electromagnetics Research*, 10:217–270, 1995.

[22] Ling Lu, John D. Joannopoulos, and Marin Soljačić. Topological photonics. *Nature Photonics*, 8(11):821–829, 2014.

[23] Tzuhsuan Ma, Alexander B. Khanikaev, S. Hossein Mousavi, and Gennady Shvets. Guiding electromagnetic waves around sharp corners: Topologically protected photonic transport in metawaveguides. *Physical Review Letters*, 114(12), 2015.

[24] Tzuhsuan Ma and Gennady Shvets. All-Si valley-Hall photonic topological insulator. *New Journal of Physics*, 18(2):25012, 2016.

[25] Tzuhsuan Ma and Gennady Shvets. Scattering-free edge states between heterogeneous photonic topological insulators. *Physical Review B*, 95(16), 2017.

[26] Marco Marangoni. Lecture Notes in micro optic. In *LM Engineering Physics, Politecnico di Milano*, Milano (MI), 2016. Classes held in March-April.

[27] Susumu Noda. Photonic-Crystal Cavities. *Optical Fiber Communication Conference*, page Th1K.1, 2016.

[28] Masaya Notomi, Takasumi Tanabe, Akihiko Shinya, Eiichi Kuramochi, and Hideaki Taniyama. On-Chip All-Optical Switching and Memory by Silicon Photonic Crystal Nanocavities. *Advances in Optical Technologies*, 2008:1–10, 2008.

[29] Emil Prodan. Robustness of the spin-Chern number. *Physical Review B - Condensed Matter and Materials Physics*, 80(12), 2009.

[30] Ezio Puppin. Lecture notes in Solid State Physics. In *LM Engineering Physics, Politecnico di Milano*, Milano (MI), 2015. Classes held in September-January.

[31] Min Qiu and Marcin Swillo. Contra-directional coupling between two-dimensional photonic crystal waveguides. *Photonics and Nanostructures - Fundamentals and Applications*, 1(1):23–30, 2003.

[32] S. Raghu and F. D M Haldane. Analogs of quantum-Hall-effect edge states in photonic crystals. *Physical Review A - Atomic, Molecular, and Optical Physics*, 78(3), 2008.

[33] Mikael C. Rechtsman, Julia M. Zeuner, Yonatan Plotnik, Yaakov Lumer, Daniel Podolsky, Felix Dreisow, Stefan Nolte, Mordechai Segev, and Alexander Szameit. Photonic Floquet topological insulators. *Nature*, 496(7444):196–200, 2013.

[34] Francisco J. Rodríguez-Fortuño, Isaac Barber-Sanz, Daniel Puerto, Amadeu Griol, and Alejandro Martínez. Resolving Light Handedness with an on-Chip Silicon Microdisk. *ACS Photonics*, 1(9):762–767, 2014.

[35] P. Russell. Photonic Crystal Fibers. *Science*, 299(5605):358–362, 2003.

[36] Wei Shi, Xu Wang, Charlie Lin, Han Yun, Yang Liu, Tom Baehr-Jones, Michael Hochberg, Nicolas A. F. Jaeger, and Lukas Chrostowski. Silicon photonic grating-assisted, contra-directional couplers. *Optics Express*, 21(3):3633, 2013.

[37] Alexey P. Slobozhanyuk, Alexander B. Khanikaev, Dmitry S. Filonov, Daria A. Smirnova, Andrey E. Miroshnichenko, and Yuri S. Kivshar. Experimental demonstration of topological effects in bianisotropic metamaterials. *Scientific Reports*, 6(1), 2016.

[38] Lukasz Szostkiewicz, Marek Napierala, Anna Ziolowicz, Anna Pytel, Tadeusz Tenderenda, and Tomasz Nasilowski. Cross talk analysis in multicore optical fibers by supermode theory. *Optics Letters*, 41(16):3759, 2016.

[39] D. J. Thouless, M. Kohmoto, M. P. Nightingale, and M. Den Nijs. Quantized hall conductance in a two-Dimensional periodic potential. *Physical Review Letters*, 49(6):405–408, 1982.

[40] N. Vico Triviño, G. Rossbach, U. Dharanipathy, J. Levrat, A. Castiglia, J. F. Carlin, K. A. Atlasov, R. Butté, R. Houdré, and N. Grandjean. High quality factor two dimensional GaN photonic crystal cavity membranes grown on silicon substrate. *Applied Physics Letters*, 100(7):71103, 2012.

[41] K. von Klitzing. Quantized Hall effect. *Journal of Magnetism and Magnetic Materials*, 34:525–529, 1983.

[42] M. A. H. Vozmediano. Renormalization group aspects of graphene. *Philosophical Transactions of the Royal Society A: Mathematical, Physical and Engineering Sciences*, 369(1946):2625–2642, 2011.

[43] Zheng Wang, Y. D. Chong, John D. Joannopoulos, and Marin Solja??i?? Reflection-free one-way edge modes in a gyromagnetic photonic crystal. *Physical Review Letters*, 100(1), 2008.

[44] Zheng Wang, Yidong Chong, J D Joannopoulos, and Marin Soljačić. Observation of Unidirectional Backscattering- SUPPLE-MENTARY States immune Topological Electromagnetic. *Nature*, 461(7265):1–6, 2009.

[45] Eli Yablonovitch. Inhibited spontaneous emission in solid-state physics and electronics. *Physical Review Letters*, 58(20):2059–2062, 1987.

Abbreviations

Abbr.		Definition
PTI	=	Photonic Topological Insulators
PhC	=	Photonic Crystals
PBG	=	Photonic Band Gap
TPSS	=	Topologically Protected Surface States
QSH	=	Quantum Spin Hall Effect
TPMW	=	Topologically Protected Meta Waveguide
TI	=	Topological Insulators
QH	=	Quantum Hall Effect
BPhC	=	Bianisotropic Photonic Crystal
SOI	=	Spin Orbit Interaction
CTPMW	=	Coupled TPMW
TE	=	Transverse Electric
TM	=	Transverse Magnetic
PBS	=	Photonic Band Structure
TP	=	Topologically Protected
MW	=	Meta-Waveguide
PEC	=	Perfect Electric Conductor
IBZ	=	Irriducible Brilouin Zone
1^{st}BZ	=	First Brillouin Zone
Fw	=	Forward propagating
Bw	=	Backward propagating
F-W	=	Full-Wave
CP	=	Circularly polarized
CMT	=	Coupled Modes Theory
CD	=	contra-directional